A Biomechanical Investigation of the Structure - Function Relationships in the Human Tongue

by

Vitaly J. Napadow

M.S. Mechanical Engineering, Massachusetts Institute of Technology, 1998
B.S. Mechanical Engineering, Cornell University, 1995

Submitted to the Harvard-MIT division of Health Sciences and Technology in partial fulfillment of the requirements for the degree of

DOCTOR OF PHILOSOPHY IN MEDICAL ENGINEERING
at the
Massachusetts Institute of Technology

August 2001
[Sept. 2001]

Signature of Author: _____
Harvard-MIT Division of Health Science and Technology
August 5, 2001

Certified By: _____
Richard J. Gilbert, M.D.
Department of Mechanical Engineering
Thesis Supervisor

Accepted By: _____
Martha L. Gray, Ph.D.
Edward Hood Taplin Professor of Medical and Electrical Engineering
Co-director, Harvard-MIT Division of Health Sciences and Technology

A Biomechanical Investigation of the Structure - Function Relationships in the Human Tongue

By

Vitaly J. Napadow

Submitted to the Harvard-MIT Division of Health Science and Technology
On August 5th 2001 in Partial Fulfillment of the Requirements
for the Degree of Doctor of Philosophy in Medical Engineering

Abstract

The human tongue is a versatile, lithe and structurally complex muscular organ that is of paramount importance for many physiological tasks. The lingual musculature is composed of various orthogonally oriented myofiber populations. Furthermore, coupling this knowledge of tissue myoarchitecture with patterns of regional deformation offers the ability to explore complex structure-function relationships in the organ. Tongue myoarchitecture was studied with Diffusion Tensor MRI (DTI), which derived the spatial diffusion tensor field in the tongue. Since, diffusivity relates directly to myofiber orientation, this *in vivo* technique successfully produced a virtual anatomical atlas. In order to relate this 3D myoarchitecture to physiological deformations, *in vivo* strain was quantified by an MRI tagging technique. This technique tagged lingual tissue with a rectilinear grid, which was subsequently imaged to track and quantify deformation through 3D strain measures. Anterior protrusion, sagittal bending, and oral stage deglutition were studied with this technique. The results demonstrated that synergistic co-contraction between various muscle populations produced the necessary deformations in global tongue shape. In order to delineate specific muscular contributions to sagittal bending, the tongue was modeled by a thermal bimetal strip analog wherein thermal contraction approximated muscle fiber activation. The results confirmed our hypothesis that sagittal bending resulted from synergistic co-contraction of two distinct myofiber populations. In conclusion, tongue deformation is intimately related to the lingual musculature, and our results confirm the characterization of the tongue as a muscular hydrostat - an organ whose musculature produces deformation as well as the structural support for that deformation.

Thesis Supervisor: Richard J Gilbert, M.D.
Title: Lecturer, Department of Mechanical Engineering

Acknowledgements

It has been a distinct pleasure to spend the past 5 years of my life contributing to the scientific knowledge base of tongue mechanics. ! must confess that, at first, studying the various maneuvers of our lingual organ seemed a far-flung outpost of academic dalliance. However, once the problem presented itself in whole with all of its clinical implications, and the scientific method was applied, it became obvious that tongue deformation could be approached as one approaches any engineering problem.

From this standpoint, I could very well thank Robert Hooke, Isaac Newton, and all of the other scientists on whose shoulders we stand when attempting our forays into classical mechanics. However, there were many people whose contributions produced a more direct influence on this body of work and who I would like to acknowledge. My advisor, Richard Gilbert, has provided continued support for this project as well as for my own personal academic growth. His patience, respect, and unceasing optimism have helped keep the spark of interest for this project alive throughout its duration. I would like to thank him for the substantial academic and personal contributions he has made to this work. I would also like to thank Van Wedeen for the many scientific contributions he has made to this thesis, especially in the chapter characterizing the structural composition of lingual myoarchitecture. Our lively conversations on topics ranging from heart and tongue mechanics to Magnetic Resonance Imaging and diffusion were a welcome influence on my maturation as a researcher. Van's imagination and creative problem solving ideas were certainly not confined to 3 dimensions, as was evidenced by his contributions in the development of Diffusion Spectrum Imaging toward the end of my work on this thesis. I would also like to acknowledge the contributions made by the third member of my thesis committee, Roger Kamm. When the time came to tie together the structural and functional elements of the thesis, Roger's inspiration and patient brainstorming produced the perfect synthesis - namely, the biomechanical analog model presented in Chapter 4.

Of course there were many other scientific contributions made throughout the thesis lifetime, and I would like to acknowledge some of the people whose timely input was most important to this work. Rohan Abeyaratne was very supportive in all matters of engineering at the beginning of my project, and his input helped produce the Tagging MRI quantification described in Chapter 2. I would also like to thank Qun Chen for his assistance in the development and implementation of the magnetic resonance methodology and patience with my still expanding foray into the wonderful world of magnetic resonance imaging.

Every project needs a financial benefactor, and I would like to thank the Whitaker Foundation for the generous financial support that over the past 5 years has helped me continue my graduate education and has kept my rent checks from bouncing.

Of course there is life outside of science, and there were so many people whose impact on my life throughout my graduate education kept me sane, humble, and in touch with the reality that exists outside the gilded cage of academia. While impossible to name them all, my roommates, John Iversen and Alexander Barnett have become wonderful friends and have graciously shared their roadmaps to successfully completing a PhD thesis - each graduating from their respective programs within the past year. My officemates Alfred Pettinger, Srikanth Vedantam, and Markus Zimmermann were always there to humor any tongue diversions I threw at their respective theses; while Debbie Blanchard was immeasurably helpful allaying my day-to-day administrative headaches and in funneling me her husband's old ice-climbing equipment. Hamza Zeytinoglu and Matthew Hoffman were my brothers of conscience and partners in crime on several memorable excursions to Digestive Disease Week - the American Gastroenterological Association's annual fair. My fellow classmates in HST were fantastic in providing a sense of community and dragging me through qualifier exams and medical classes. Who else would allow me to stick a 20gauge syringe needle into their arm or any of the other personal

affronts experienced in our Introduction to Clinical Medicine class? I would like to thank Ngon Dao, Chris Hartemink, Thomas Heldt, Nina Menezes, Mark Price, Patrick Purdon, and Sham Sokka and David Tuch for making the HST experience one I will remember fondly for the rest of my life.

Finally, and most importantly, I would like to thank my family for supporting my studies all these years. Specifically, my mother, Nina, and father, Joseph, provided me the opportunity to enter any academic field; while supporting any tangents along the way. How different my life would have been had I still been in Kharkov, Ukraine, working on a thesis in tongue mechanics. I would also like to thank my grandfather, David, and the rest of my extended family for always reminding me of the things that are truly important in this life.

I would like to end these acknowledgements with a brief story. My grandmother, Anna Braginskaya, was working on her doctoral dissertation in biochemistry in the early 1940's in Kharkov, Ukraine. WWII was ravaging the countryside and as the German army approached, most of Kharkov was evacuated. My grandmother's work was deemed critical to state security, and so she was allowed to stay and continue her research. It was August 1943 when Kharkov finally fell. My grandmother was forced to flee the city and destroy her thesis, lest it fall into German hands. Hence, she was never able to complete her dissertation. Throughout my academic career, my grandmother, who just recently turned ninety years old, has been an ardent supporter, providing encouragement at every turn. It is for these reasons and many more that I would like to dedicate this thesis to my grandmother, Anna.

Contents

Table of Figures

Chapter 1

1 Introduction

The human tongue (L. lingua; G. glossa) is a versatile, lithe and structurally complex muscular organ that is of paramount importance for many physiological tasks including deglutition (swallowing), mastication (chewing), gustation (taste sensation), respiration, and phonation (speech). What has made tongue physiology such a fascinating topic of study for the past five years (and, I might add, a topic rich enough for many future research endeavors), has been the diversity of the organ's functions and, hence, the near limitless degrees of freedom of lingual deformation. Moreover, lingual deformation closely corresponds to the organ's myoarchitecture, defined as the gross organization of the various muscular elements within the tongue. Exploring lingual muscular anatomy provides clues to the functional capabilities of the organ, and it is these structure-function relationships that have become the chief focus of study in this thesis.

Lingual deformation is crucial to normal human swallowing, which is an instinctive and precisely orchestrated act, completed on average 2400 times within a 24-hour period (Miller, 1982). Deglutition has a simple goal: to transport food from the oral cavity to the esophagus, while avoiding aspiration, the unexpected inspiration of pharyngeal contents into the airway (Groher, 1997). During normal deglutition, the tongue acts first to configure and then to propel the ingested bolus[1]. Abnormal deglutition is termed dysphagia, which is a symptom of underlying disease technically defined as an "abnormality in the transfer of a bolus from the mouth to the stomach" (Groher, 1997). The incidence of dysphagia has been reported as 35% in people aged 50-79 and 32% of all patients in intensive care units, while epidemiological studies have estimated that approximately 14.2% of patients over the age of 60, or 6,228,116 individuals, currently suffer from dysphagia (Baum and Bodner, 1983). Furthermore, greater than 50% of the approximately 750,000 individuals who present with stroke annually in the U.S. experience clinically significant oropharyngeal dysphagia at some point in the

[1] bolus (L. bolos, lump or choice morsel) describes the mass of food or liquid swallowed at one time.

illness (Smithard, O'Neil et al., 1997). Of these, it is estimated that ~50% will be affected by malnutrition, ~37% will develop pneumonia, and ~4.3% will die of pneumonia in the absence of adequate treatment (Croghan, Burke et al., 1994; Davalos, Ricart et al., 1996). Lingual disorders comprise one of the most common mechanisms for oropharyngeal dysphagia in clinical medicine. Given the critical position of the oral cavity in the entry to the GI tract, the impact of these disorders may include malnutrition, dehydration, and the increased risk of aspiration pneumonia leading to premature death (Croghan, Burke et al., 1994; Davalos, Ricart et al., 1996; Smithard, O'Neil et al., 1997). Hence, the clinical motivations of this thesis rested in the study of deglutition.

1.1 Lingual Phylogeny and Anatomy

The human tongue is a rather large muscular organ that fills the majority of the oral cavity , as it does in all mammals except for some of the Odontoceti (toothed whales), Rodentia, and Ornithorhyncus (duck-billed platypus) (Sontag, 1925). Our tongue's phylogenetic origins date back to prehistoric fish, where the tongue first appears as a rudimentary organ (Livingston, 1956). The organ is a constant feature in vertebrates above this level. In morphology, the tongue is an appendage of the hyoid part of the branchial skeleton and can thus be considered a variation on the anatomy of the floor of the mouth. In fact, the simplest form of the vertebrate tongue (such as in some birds and snakes) consists of an extension of the hyoid apparatus, the entoglossal process, which is covered by a mucous membrane. In this case, the cartilaginous tongue is moved by simply moving the hyoid bone. Muscles such as the sternoglossus (a tongue retractor) connect the sternum to the tongue, with some fibers having connections to the hyoid bone. The human tongue does not have a sternoglossus muscle, but retains a connection to the hyoid bone (through the hyoglossus muscle), which is then connected to the sternum through the sternohyoid muscle. Thus, the human tongue is still influenced by hyoid motion through phylogeny; however, its complex musculature grants this organ a relative independence of deformation.

Developmentally, human tongue size reflects physiological demands. At birth and during early maturation, the tongue is disproportionately large relative to its surrounding structures. In a newborn baby, the tongue essentially fills the oral cavity. In theory this is due to the increased need for suckling during these years (Brodie, 1952). With development of the infant, radiographic records have demonstrated that the oral cavity increases in size faster than the tongue, resulting in the appearance of

a "masticatory space" (Bosma, 1963). The pharynx also enlarges (A-P) as the tongue descends. The oral cavity also enlarges along the inferior-superior dimension due to the eruption of teeth. Thus, the tongue no longer maintains resting contact with the hard palate, although contact with the soft palate is maintained, separating the mouth from the pharynx.

The adult human tongue is covered on its dorsum, tip, and sides by a mucous membrane; however, its root is firmly attached to the floor of the oral cavity (**Figure 1-1**). The dorsum of the tongue is divided by the "V"-shaped sulcus terminalis into oral (anterior 2/3) and pharyngeal (posterior 1/3) subdivisions. These subdivisions have an embryological origin, as the oral portion develops from the first branchial arch, while the pharyngeal portion develops from the second and third branchial arches (Doran, 1975). The oral portion of the tongue is freely deformable and is loosely attached to the floor of the oral cavity by a flap of skin, termed the lingual frenulum. The sublingual folds are also located on the floor of the mouth. These folds are part of the mucosal lining of the mouth, and end close to the base of the frenulum in special papillae that contain the orifice of the submandibular duct (Wharton's Duct). This duct transfers salivary excretions from the submandibular gland (one of three salivary glands, the others being the parotid and sublingual) to the oral cavity. On either side of the frenulum's midline attachment to the ventral surface of the tongue are the lingual veins, and more laterally, the frilly folds of sublingual epithelium termed the plica fimbriata. On the dorsum of the oral portion of the tongue lies the median groove, which represents the site of fusion of the distal tongue buds during embryonic development (Moore, 1992). The mucous membrane on the oral tongue is rough, owing to the existence of filiform, fungiform, vallate, and foliate papillae. This roughness is due to keratinization of the papillae and is especially pronounced in carnivore mammals, where it aids in rasping flesh from the bones of prey (Doran, 1975). The fungiform, vallate, and foliate papillae contain taste receptor cells located in "taste buds."[1] In contrast to the oral tongue, the pharyngeal portion of the tongue does not contain any papillae, but does have a cobblestone appearance on its dorsum owing to the existence of underlying nodules of lymphoid tissue – the lingual tonsil.

[1] In general, within the animal kingdom, the density of lingual "taste buds" appears to be greater and more diverse in herbivores than in carnivores and insect feeders (Livingston, 1956). I'll refrain from comment on the implications of this finding to the vegetarian subculture in *homo sapeins*!

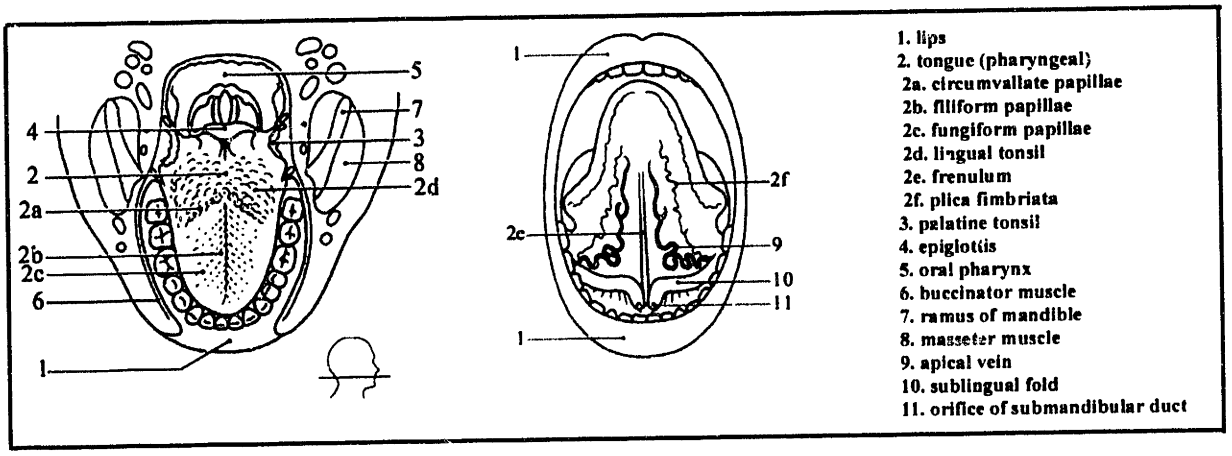

Figure 1-1 A labeled schematic of the external human tongue.

The tongue body is composed of many different types of tissue, including epithelial, glandular, connective, and muscular. However, it is the muscular tissue that affords the tongue its impetus for deformation, and hence will be explored more rigorously in this thesis. Previous investigations of tongue musculature have been limited to observational histological techniques (Miyawaki, 1974; Depaul and Abbs, 1996; Mu and Sanders, 1999; Takemoto, 2001). While histological techniques have offered a reliable modality to explore cross-sectional anatomy, they are destructive and limited to *in vitro* investigations. Hence, one of our motivations was to produce a technique to investigate lingual anatomy *in vivo*. This technique could then be developed as a possible clinical screening procedure for the quantification of dysphagic myopathy.

The musculature of the tongue is composed of two types of muscles – intrinsic and extrinsic (Sontag, 1925). Intrinsic muscles are myofiber populations wholly contained within the body of the tongue, unconnected to any external bony attachments. In contrast, extrinsic muscles have their origin on bone and their insertion within the tongue proper. The intrinsic muscles include the superior and inferior longitudinalis, the transversus, and the verticalis muscles. The extrinsic muscles include the genioglossus, the hyoglossus, the styloglossus, and the palatoglossus muscles. The tongue rests on a muscular floor composed of the geniohyoid muscle, which runs in the mid-sagittal plane from the mental spine of the mandible to the body of the hyoid bone; and the mylohyoid, which runs from the mylohyoid line of the mandible to the raphe and body of the hyoid bone.

Motor innervation to all tongue muscles (except the palatoglossus m.) is supplied by CN-XII, the hypoglossal nerve. This cranial nerve passes between the mylohyoid and hyoglossus muscles, and divides into two branches (Lowe, 1981). The smaller lateral branch innervates the hyoglossus, styloglossus, and the inferior longitudinalis muscles; while the larger medial branch innervates the

genioglossus, transversus, verticalis, and superior longitudinalis muscles. Sensory and taste innervation is also divided by the sulcus terminalis into the anterior 2/3 and the posterior 1/3. In the anterior portion, the lingual nerve (a branch of CN-V^3) provides general sensory innervation, while the chorda tympani nerve (a branch of CN-VII) provides taste sensation (except to the vallate papillae). In the posterior portion of the tongue, the lingual branch of the glossopharyngeal nerve (CN-IX) provides both general and special (taste) sensation.

Lingual muscular anatomy is explored in more detail in Chapter 2 through the application of diffusion based MRI techniques and two-photon microscopy. Diffusion Tensor Imaging (DTI) was used to delineate muscular fiber tracts by measuring water self-diffusivity in tongue tissue. Two-photon microscopy was used to both explore the three-dimensional microstructure of tongue musculature and to correlate this microstructure with the more gross DTI measurements.

1.2 Lingual Physiology

Structure-function relationships in muscle are usually predicated on a functional deformation that occurs along the muscle fiber orientation. It was Leonardo da Vinci (1452-1519) who noted that a muscle "uses its power along the line of its length" (McMurrich, 1930). In other words, myofibers do one thing well – they contract. For example, in order to place food into your mouth, you bring your hand (holding the food) closer to the open orifice. To do this, you will most likely contract your biceps brachii muscle, imparting an angular deformation about the elbow joint, and bringing your hand closer to your face. Conversely, if you want to move your hand back away from your mouth, you can contract your triceps brachii muscle, an antagonist of the biceps brachii. In fact, there exist other muscle groups (e.g. brachialis m., brachioradialis m., etc.), which either aid, restrict, or stabilize these functional movements. Our musculoskeletal systems are filled with these synergistic and antagonistic paired muscular elements. Another key component is skeletal support, which is crucial for successful limb kinematics. If the humerus bone did not provide a semi-rigid support to resist biceps and triceps contraction, your upper limb would simply shorten upon contraction of either muscle. Generally, skeletal support is provided by bony internal elements in vertebrates and by hardened external shells (exoskeletons) in arthropods. In the tongue there are no simple hinge or ball-and-socket joints. In fact, there are very few bony elements whatsoever. Rotational and translational deformation is not even constrained to predefined joints, occurring almost anywhere and on a more local level. The tongue falls

into a rare class of organs known as muscular hydrostats, that is, organs whose musculature both creates motion and supplies skeletal support for that motion (Kier and Smith, 1985; Smith and Kier, 1989). This support derives from the primary composition of skeletal muscle – an *incompressible* aqueous fluid. Hence, lingual deformations are isochoric; that is, conserving tissue volume. For example, the tongue contracts in one dimension to form concavities along the dorsal surface, while at the same time expanding in an orthogonal dimension, producing convexities elsewhere. Functionally, the desired deformation may be either the concavity *or* the convexity, depending on the task. This evolutionary flexibility is what makes lingual deformation such a fascinating topic, and is discussed further in Chapter 3 with the visualization and quantification of tongue deformation patterns. The analysis was completed with an imaging and strain quantification technique termed Tagging MRI (Napadow, Chen et al., 1999). With our technique, we were able to strain map the musculature of the tongue during several primitive deformations, as well as during the oral stage of deglutition.

1.3 Theoretical Modeling

In order to test some of our conclusions regarding lingual structure-function relationships, we created a biomechanical analog model to explore a primitive movement of the tongue, sagittal tongue bending. This deformation can be considered a foundation of lingual deformations seen during both phonation and oral stage swallowing, wherein the tongue undergoes sagittal bending to place the tip posterior to the top row of teeth, forming an accommodation pouch in which the bolus of food is held. This maneuver was an apt one to study for several reasons. Firstly, its fundamental nature makes it applicable to various fields of study. Secondly, its deceptive simplicity allows for a modeling strategy wherein the deformation is dependent on several (but not all) of the tongue's muscular elements. Thus, the model was comprised of tractable analytical solutions to a limited number of governing equations. Thirdly, since this maneuver was previously studied empirically with Tagging MRI, we could compare theoretical and experimental results; thereby strengthening the validity of the model. The theoretical model of tongue bending was based on classical bimetal strip theory, which is typically applied in electronics design. Bimetal strip theory applies to the case in which two bonded metals of different thermal expansion coefficients assume a bent configuration when subjected to a temperature change. In the case of sagittal tongue bending, a beam curvature is produced when one muscle layer (the longitudinalis muscle) contracts more so than the other layers. Hence, if muscular contractile strain can

be considered analogous to thermal contractile strain, contraction of the longitudinalis and transversus muscles can be accomplished by specifying the directionally dependent thermal expansion coefficients.

1.4 Experimental Background

Finally, this thesis employs several experimental techniques not typically utilized in the field of biomechanics. I offer the reader a brief introduction and background into both magnetic resonance imaging (**Appendix A**) and two-photon microscopy (**Appendix B**) in the appendices section of the thesis. While not exhaustive, this introduction is meant to acquaint the uninitiated reader with said techniques and provide a working vocabulary.

Chapter 2

2 Exploring Lingual Myoarchitecture

The mechanical properties of skeletal muscle are dictated largely by the distribution and spatial orientation of its constituting fibers. While the determination of principal fiber direction is relatively straightforward in homogeneous tissues, whose fibers are largely aligned along a single spatial axis, the process is considerably more complicated in heterogeneous tissues such as muscular hydrostats, where fibers are aligned along multiple axes. This truism also holds for the human tongue, whose 3D myoarchitecture is a crucial component of the study of lingual mechanics. The tongue's myoarchitecture, a complex array of interdigitating fibers, is responsible for the organ's almost limitless array of displacements and deformations. Hence, to understand lingual physiology one must first understand lingual anatomy.

2.1 Classic Histological Review of Lingual Myoarchitecture

Deriving accurate information regarding lingual muscle fiber orientation has classically relied on meticulous dissection and multi-slice haematoxylin & eosin histology (the gold standard), a technique which is both laborious and ill-posed. The difficulty stems from the inability of histology, an inherently two-dimensional technique, to resolve through plane fiber angle deviation. Moreover, accurately assembling these planar local data into a coherent and complete three-dimensional atlas poses further problems (McLean and Prothero, 1992). Histology is also invasive, requiring the sacrifice of the sample. This particular characteristic is rather prohibitive to studying human subjects *in-vivo* - the ultimate goal in developing MR techniques that resolve tissue myoarchitecture. With these caveats in mind, past *in vitro* investigations have been very helpful in outlining the gross configuration of lingual musculature. Miyawaki performed a detailed observational study in which the tongue was

pretreated in xyrol, thereby elucidating fiber directionality (Miyawaki, 1974). Other investigations have utilized conventional histologic and histochemical techniques to derive geometrical fiber interrelationships, musculature population percentage, fiber type, and innervation (Depaul and Abbs, 1996; Mu and Sanders, 1999; Takemoto, 2001).

In general, muscular hydrostats share the common anatomical arrangement of a myofiber population perpendicular to the long axis of the organ, along with one that is parallel to the long axis (Smith and Kier, 1989). This arrangement is also seen in the mammalian tongue. The musculature of the tongue is composed of two categories of muscles – intrinsic and extrinsic. Intrinsic muscles are myofiber populations wholly contained within the body of the tongue, unconnected to any external bony attachments (**Figure 2-1**). In contrast, extrinsic muscles have a bony attachment outside the tongue proper (**Figure 2-2**).

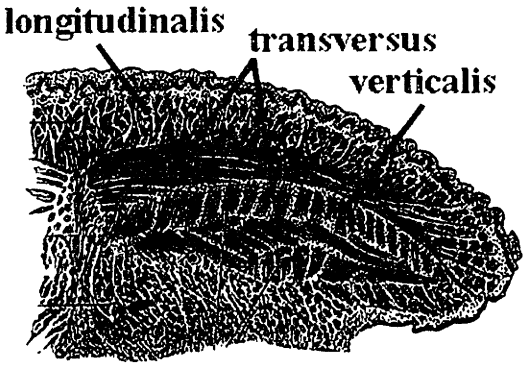

Figure 2-1 The intrinsic musculature of a coronal cross-section of the mammalian tongue. Intrinsic muscles have no bony attachments, being wholly contained within the tongue. (courtesy of Gray's Anatomy by Henry Gray. Crown Publishers, Inc., 1976)

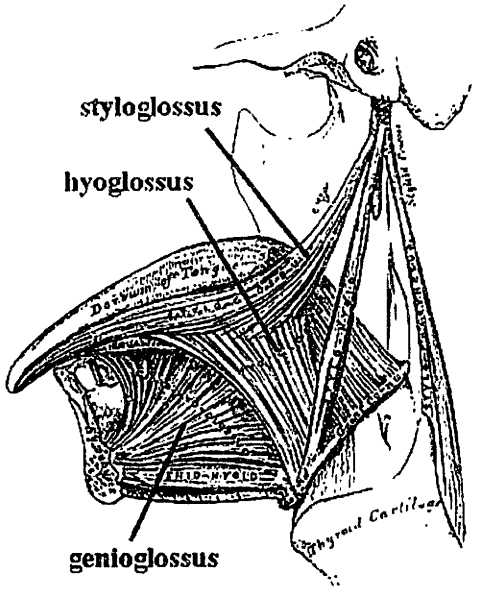

Figure 2-2 The extrinsic musculature of the tongue. Extrinsic muscles have a bony attachment outside of the tongue proper. (courtesy of Gray's Anatomy by Henry Gray. Crown Publishers, Inc., 1976)

The anterior tip of the tongue is composed strictly of intrinsic muscles. These include the superior longitudinalis muscle, which runs parallel to the dorsal surface of the tongue, below the thick epithelium (Miyawaki, 1974). Below this myofiber population, lies the intrinsic core of the tongue.

This region contains sequential sheets[1] (in the coronal plane) of superior-inferiorly and medial-laterally directed fibers – the verticalis and transversus muscles, respectively. Below this core layer is the inferior longitudinalis muscle. The transversus, verticalis, and superior longitudinalis muscles also extend to the posterior tongue, where they seamlessly merge with the extrinsic muscles. These muscles come into the body of the tongue proper from various directions and include the genioglossus, which constitutes such a large portion of the mammalian tongue that it has been occasionally divided into two separate entities (Abd-El-Malek, 1938). The anterior fibers of the genioglossus originate on the mental spine of the mandible and fan postero-superiorly toward the dorsal surface. In the intrinsic core, these fibers merge with intrinsic verticalis fibers into discrete lamellae (Takemoto, 2001). The posterior fibers run antero-posteriorly to the root of the tongue, the hyoid bone, and the base of the epiglottis. Other extrinsic muscles include the hyoglossus, which inserts into the postero-lateral aspect of the tongue from the hyoid bone; the styloglossus, which inserts into the postero-lateral aspect from the styloid process; and palatoglossus, which connects the lateral aspect of the tongue to the soft pallate. This last thin muscle, while entering the body of the tongue, is considered more of a pharyngeal muscle (Lowe, 1981).

Interestingly, muscle fiber type exhibits a steady gradient from anterior to posterior, with anterior muscles being composed almost exclusively of fast-twitch type II fibers, while posterior muscles exhibit a mixed slow twitch/fast twitch (type I/type II) composition (Depaul and Abbs, 1996). A similar gradient exists from superficial to deep muscle structures. It has been hypothesized that this relationship arises since the anterior tongue executes more rapid contractions (mastication, speech) than posterior, deeper tongue regions (respiration: the genioglossus contracts with each inspiration, openning the airway). In fact, the tongue tip has a very high density of mechanoreceptors, and is one of the most sensitive areas of the body (Ringel and Ewanowski, 1965).

It is important to note that the extrinsic muscles merge seamlessly with the intrinsic musculature, confounding the simplified characterization of distinct muscular populations within the tongue. For example, as the genioglossus muscle fans superiorly into the tongue's intrinsic core, its fibers merge with verticalis muscle fibers, sometimes extending all the way to the superior longitudinalis (Takemoto, 2001). The existence of multiple muscular interconnections and the variability of intramuscular fiber type corroborates with our thesis that the tongue is best approached as a continuum of heterogeneously oriented muscular elements, rather than a collection of distinct muscle

[1] It has been estimated that these sheets number close to 100 in the human tongue (Takemoto, 2001).

groups. Following this mantra, the imaging of lingual myoarchitecture was approached with diffusivity based MRI techniques, which subdivided the tongue tissue into a 3D grid of data voxels.

2.2 Diffusion Tensor Imaging (DTI) of the Tongue

The three-dimensional myoarchitecture of the tongue was derived in this thesis by measuring the spatially variant proton self-diffusivity with a diffusion-tensor MRI technique. Diffusion tensor imaging (DTI) measures diffusivity by NMR signal attenuation (Stejskal, 1965). In general, diffusion is a physical property, which represents the random translational motion of molecules, and is a function of the position of cytoskeletal elements and membrane permeability, as well as bulk motion, temperature, and magnetic susceptibility. If there are no macromolecular barriers to affect proton movement in a tissue preparation, molecular diffusion is equal in all directions (termed isotropy). In contrast, when diffusion is hindered by the existence of macromolecular barriers (i.e. membranes or fibers), as in the majority of biological tissues, the pattern of molecular motion is greater along preferred directions (termed anisotropy). Diffusion in muscle tissue is greatest along the fiber direction due to myofiber geometry. Since myocytes are cylindrically symmetric, their elongated cellular membranes impose barriers for the self-diffusion of free water. Hence, the greater the hindrance to proton self-diffusion, the lower the MR signal attenuation – a relationship that can be exploited to derive the spatially variant diffusion tensor. Signal attenuation receives contributions from both intracellular and extracellular fluid; however, the elongated geometry of muscle cells insures that both components induce maximal attenuation along the myofiber long axis (Norris and Niendorf, 1995). Thus, visualization of the self-diffusion tensor field can be utilized as a virtual 3D anatomical atlas of muscle tissue (Reese, Weisskoff et al., 1995; Doorn, Bovendeerd et al., 1996; Gilbert, Reese et al., 1998). NMR imaging of the water diffusion tensor has been shown in a variety of tissues to have the capacity to noninvasively map tissue fiber architecture (Hajnal, Doran et al., 1991; Moseley, Kucharczyk et al., 1991; Basser, Mattiello et al., 1993; Wu, Wong et al., 1993; Wedeen, Reese et al., 1995). In this thesis, DTI was successfully applied to an *ex vivo* mammalian (bovine) tongue, as well as an *in vivo* human subject.

2.2.1 DTI Methodology

Diffusion Tensor Imaging was accomplished by producing an image sensitized to proton self-diffusivity in a given direction. In order to recover diffusivity data, transverse magnetization was first dephased and then rephased under the influence of a spatially dependent magnetic field gradient. This "echo" completely rephased the original magnetization except for T_2 decay and any gross motion along the direction of the applied gradient, such as that due to proton diffusion. This produced a loss of phase coherence and incomplete refocusing, resulting in attenuation of the MRI signal. From the extent of signal attenuation, and taking into account T_2 decay, an apparent diffusion coefficient (ADC) was calculated[1]. A typical pulse sequence produces diffusion sensitization by using paired Stejskal-Tanner gradient pulses in a spin-echo excitation, followed by image acquisition using the HASTE pulse sequence (**Figure 2-3**).

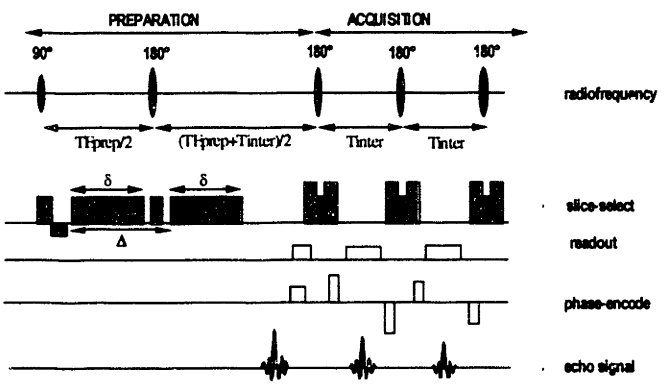

Figure 2-3 A typical spin-echo DTI pulse sequence using Stejskal-Tanner diffusion sensitization pulses and HASTE imaging to produce a slice specific diffusivity map of the tissue.

The calculation of a diffusion coefficient in several directions (controlled by spatially variant applied magnetic gradients) resulted in a unique array of three-dimensional data for each voxel – the apparent diffusion tensor. This symmetric second-order tensor can be conceived as a function of signal attenuation by the following equation:

$$\ln\left(\frac{S_b}{S_0}\right) = -\sum_{i=1}^{3}\sum_{j=1}^{3} b_{ij} D_{ij} \tag{2.1}$$

[1] Because this diffusivity coefficient is averaged over a finite echo time, TE, it is called an "apparent diffusion coefficient" (ADC). If any imaging magnetic field gradients are on during the diffusion time, they will increase the error between the measured diffusion coefficient and a "real" diffusion coefficient (Bihan, 1995). Thus, any extraneous gradients should be minimized.

where S_b is the signal attenuated image, S_0 is the unattenuated image, b_{ij} is the ij component of the classic b-matrix, and D_{ij} is the ij component of the diffusion tensor (Basser, 1995). The b-matrix is related to the direction dependent diffusion sensitization and is expressed as:

$$\mathbf{b} = \int \mathbf{k}^T \mathbf{k} dt \tag{2.2}$$

where the reciprocal space vector, **k**, can be expressed as a function of the proton gyromagnetic ratio, γ, and the 3D diffusion sensitization gradient vector, **G**

$$\mathbf{k} = \gamma \int \mathbf{G}\, dt \tag{2.3}$$

For example, in the classical pulse sequence displayed in **Figure 2-3** with rectangular diffusion sensitizing gradient pulses, the b-factor was defined by: $b_{ij} = \gamma^2 G_i G_j \delta^2 (\Delta - \frac{1}{3}\delta)$. In order to efficiently cover 3D space with the diffusion sensitization gradients, seven images were acquired; six with gradient vectors toward the unopposed edge centers of a theoretical cube, and one unattenuated ($\mathbf{G} = 0$) image. This produced a system of linear equations, which was solved for the diffusion tensor, **D**, in the x-y-z coordinate system. This tensor was transformed by solving $\mathbf{D}v = \lambda v$ in order to derive the diffusion tensor in the eigen coordinate system.

Diffusion sensitization was achieved by proton spin preparation using either spin echoes or stimulated echoes (Merboldt, Hanicke et al., 1991). Stimulated echo sequences are preferable to their spin echo counterparts because they allow higher b-values to be realized with average magnetization gradients (Norris and Niendorf, 1995). Furthermore, they allow for longer diffusion times because the longitudinal magnetization, which is used for the stimulated echo, is being stored during the diffusion, or mixing time TM, and is not subject to transverse T_2 decay. Unfortunately, stimulated echo sequences have only half the signal to noise ratio (SNR) of spin echo techniques, necessitating considerable averaging. Our stimulated echo sequence incorporated single-shot echo-planar spatial encoding with TE/TM/TR = 54/480/800 ms and spatial resolution of 3 x 3 x 6 mm. Using 16 signal averages, acquisitions were completed in 3 minutes per slice yielding an SNR of approximately 40:1 (glossal-to-background magnitude ratio) in the unattenuated images, S_0 (diffusion sensitizing gradients off), and mean SNR of approximately 20:1 in the attenuated images S_b (diffusion sensitizing gradients on).

An additional complication of diffusion-weighted imaging was the induction of image artifacts produced by eddy currents generated during the strong diffusion-sensitizing magnetic field gradients. Each on/off transition of the pulsed field gradient produced currents in the conductive portions of the magnetic bore, which oppose the change in magnetic field, **B**. These currents generated a magnetic field which could be modeled as a spatially variant decaying change in the static magnetic field B_0,

$$B(\mathbf{x},t) = B_0 + \Delta B(\mathbf{x})\sum_n s(n)\exp(-t/\nu) \tag{2.4}$$

Where $\Delta B(\mathbf{x})$ is the eddy current induced magnetic field fluctuation, s(n) is the sign of the field (whether the gradient pulse was turned "on" or "off"), and ν is the decay constant of the current induced field. Thus, $\Delta B(\mathbf{x})$ acted as an "unwelcome" imaging gradient which distorted the k-space trajectory of the pulse sequence's native imaging gradients. The specific distortion depended on the axis of the diffusion encoding gradients inducing the eddy currents. In this regard, distortions of diffusion-weighted images produced by eddy currents may produce or modify the extent of diffusion anisotropy determined. In order to minimize the contribution of eddy currents, we adopted a pulse sequence employed by Reese et al; which split the usual two long unipolar diffusion gradients into two bipolar gradients separated by another 180° refocusing pulse, thereby increasing the number of gradient transitions from n = 4 to n = 8 (Reese, Weisskoff et al., 1998). This modification caused more transitions for a sequence of the same b-factor. Furthermore, eddy currents from paired positive and negative transitions cancel more completely the closer spaced they are temporally. Thus by placing paired positive and negative gradient transitions closer together with this "double echo" pulse sequence, the induced eddy currents canceled each other out more completely, reducing artifactual image distortion.

The complete 3D diffusion tensor was computed for each image voxel and was visualized as individual octahedra, whose axes were scaled by the size of the eigenvalues and oriented along the corresponding eigenvectors (**Figure 2-4**). Within the eigen coordinate system, the principal eigenvector, v_1, corresponded to the direction of greatest diffusion, or principal fiber direction, and was the major axis of the octahedron. The eigenvalues and eigenvectors for each diffusion tensor represented the magnitude and direction of maximal proton diffusivity, respectively. Octahedra were color-coded based on the principal eigenvector {x,y,z} triplet mapped to the red-green-blue color-space: $\{|v_{1x}|, |v_{1y}|, |v_{1z}|\} \in$ {red, green, blue}.

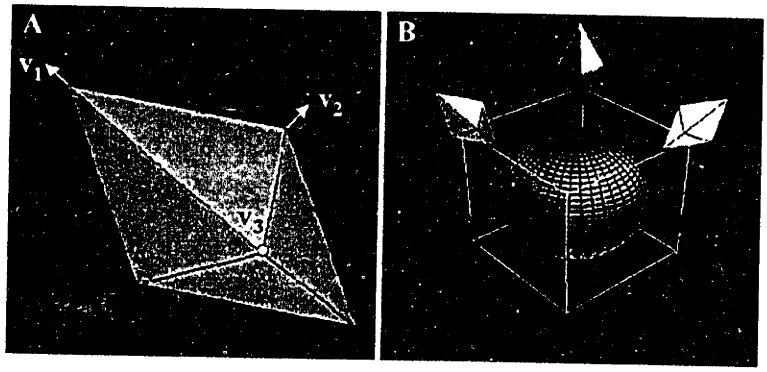

Figure 2-4 (A) Visualization of the diffusion tensor was accomplished with an octahedron oriented and scaled by the tensor eigensystem. (B) The octahedra were color-coded based on the orientation of the principal eigenvector.

Diffusion tensor anisotropy is an index that quantifies the oblateness of the diffusion tensor, and hence the homogeneity of fiber orientation within a voxel. Simply put, homogeneous tissue where most of the myofibers are oriented along the same axis, will have a high anisotropy index. Conversely, heterogeneous tissue with different myofiber orientations (e.g. multiple intertwined or overlaid fiber populations) will have a low anisotropy index. Diffusion anisotropy was measured by a function incorporating the two greatest eigenvalues of the diffusion tensor, λ_1 and λ_2. Two, and not all three, eigenvalues were necessary to define an anisotropy index because the diffusion tensor field for a given tissue has the property of trace invariance (Pierpaoli and Basser, 1996), thus the third eigenvalue is a dependant quantity. While various anisotropy indices have been suggested (Basser, 1995), simple functions have the advantage of ease of interpretation, and were utilized in this thesis. For instance, the anisotropy index $f_{ind} = (\lambda_1 - \lambda_2)/\sum\lambda_i$ was used in analyzing *ex vivo* bovine tongue data; while $f_{ind} = \lambda_1/\lambda_2$ was used in analyzing *in vivo* human data. The former index expresses isotropy with a value of nil, while the latter index conveys isotropy with a value of unity.

2.2.2 *Ex Vivo* DTI of Bovine Tongue

In order to explore the applicability of DTI to the study of myoarchitecture and human lingual anatomy, we imaged the structurally similar bovine tongue (Wedeen, Reese et al., 2001). Magnetic resonance imaging was performed on 4 *ex-vivo* cow tongues obtained from Blood Farms (West Groton, MA). The excision was performed by first exposing the tongue by making an incision from the thyroid prominence to the angle of the mandible, followed by an en bloc resection. Whole tongue specimens were refrigerated and scanned within 24 hours of harvest.

For each specimen, the whole tongue was carefully sealed in plastic and wrapped with a towel to minimize susceptibility artifact (which arises from tissue-air interfaces). Diffusion tensor imaging was performed on contiguous slices perpendicular to the antero-posterior axis of the tongue. Data were acquired at 1.5 T with 20cm receive-transmit head coil and a diffusion-sensitive stimulated echo pulse sequence. Diffusion sensitization utilized gradient pulses of amplitude $|\mathbf{G}|$ = 100 mT/m and duration δ = 10ms, corresponding to net a spatial modulation $\|\mathbf{k}\| = 2\pi\gamma_H\delta|\mathbf{G}|$ = 40 radians/mm (γ_H is the proton gyromagnetic ratio, $\mathbf{k}$ is a column vector). Using an interpulse delay Δ = 500 ms, the diffusion sensitivity |b| factor was calculated to be

$$|\mathbf{b}| = \int_{\Delta} \mathbf{k}^T\mathbf{k}\,dt \approx |\mathbf{k}|^2\Delta \approx 850\,\mathrm{mm}^2/\mathrm{sec} \tag{2.5}$$

The myoarchitecture of the bovine tongue was analyzed by visualizing the diffusion tensor field (**Figure 2-5**). The data from one representative specimen were presented here as a sequence of coronal slices. The diffusion tensors corresponding to each voxel were rendered as octahedra, and color-coded based on the principal eigenvector such that the antero-posterior fiber orientation was blue, medial-lateral fiber orientation was red, and inferior-superior fiber orientation was green. The posterior tongue demonstrated a central region of fibers originating at the inferior surface and projecting in a fan-like manner in the superior, lateral, and posterior directions (corresponding to the genioglossus muscle). Lateral to this central region were two populations of fibers, the first directed posterior and inferior (corresponding to the hyoglossus muscle) and the second directed posterior and superior (corresponding to the styloglossus muscle). The anterior body of the tongue consisted of a central region of orthogonally oriented intrinsic fibers (transversus and verticalis muscles) surrounded by a sheath-like tract of longitudinally-oriented fibers (superior and inferior longitudinalis muscles).

Visualization required the use of both principal eigenvector color-coding and three-dimensional graphics (octahedra), since the colors of the color-sphere did not correspond to unique 3D orientations. This resulted from the insensitivity of the color code to relative signs of vector components. For example, the genioglossus and hyoglossus muscles, with different three-dimensional orientations, were both coded blue-green. The octahedra verified the postero-superior orientation for the genioglossus and antero-superior orientation for the hyoglossus. Inter-sample variability in the DTI data was addressed in Appendix C.

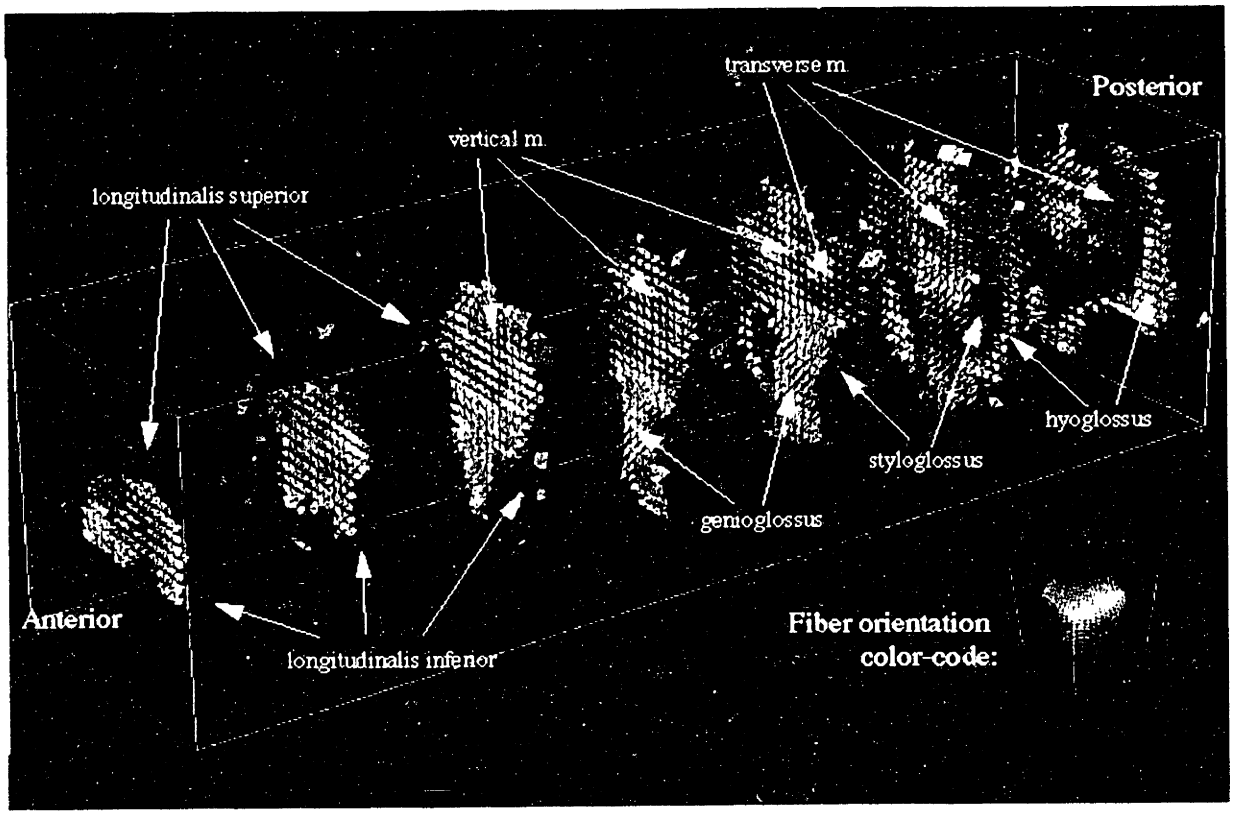

Figure 2-5 Coronal slices comprising the bovine tongue were obtained by diffusion tensor imaging. Extrinsic and intrinsic muscles are identified. An octahedron whose shape approximated the local diffusion tensor was represented at each imaging voxel. The 3D fiber orientation corresponded to the octahedron's long axis and was displayed according to a color code (inset lower right). The intrinsic sheath, which consisted of the superior and inferior longitudinalis muscles, corresponded to blue octahedra. The intrinsic core was red and green, corresponding to horizontal and vertical fiber populations. The extrinsic genioglossus and hyoglossus muscles were oblique. While both were color coded blue-green, the octahedra show their distinct orientations, the genioglossus oriented antero-caudally, the hyoglossus postero-caudally.

Another issue with this technique was in the interpretation of regions with a high density of differently oriented fiber populations, as occurred in the tongue core. In homogeneous tissue, the principal eigenvector is aligned in correspondence with the most prevalent population; however, in heterogeneous tissue, it would be erroneous to assume this or that the second eigenvector was aligned along the second most prevalent population. In other words, it would be erroneous to assume that the core was composed of fiber populations that were orthogonal on the scale of the voxel based on the characteristic orthogonality of the eigensystem coordinate reference frame (represented by the octahedron). Decoding the fiber direction of the second (or even third, or fourth, ...) most prevalent fiber population requires higher diffusivity resolution *within* the measurement voxel. In fact, the measured 2nd order diffusion tensor comprised the sum proton diffusivity of both fiber populations. This is

commonly referred to as the "partial volume effect." The correct relationship between heterogeneous fiber populations and a single second order diffusion tensor was explored more rigorously in Subchapter 2.3.3, where DTI results were compared to actual tissue microstructure.

Owing to the distinction in the anterior tongue between the orthogonal core fibers and the longitudinal sheath fibers, this tissue region was further analyzed by graphically depicting its two-dimensional architecture (**Figure 2-6**). In this rendering for a representative sample (the same sample as that displayed in **Figure 2-5**), $\mathbf{v}_1$ and $\mathbf{v}_2$ constituted the face of a flattened cylinder, representing maximal angular dispersion of fiber angles. That is, if a voxel enclosed more than one distinct fiber population, the two most prevalent populations were coplanar with the $\mathbf{v}_1$-$\mathbf{v}_2$ plane. This property was useful when using cylinders to represent the diffusion tensor in heterogeneous fiber regions, such as the anterior tongue core. In this region, fiber orientations were most dispersed, or varied, in the axial plane of the tongue. These data were shown for the 3rd (anterior to posterior) slice of the complete diffusion tensor data set (which was shown in **Figure 2-5**), and depicted a striking contrast between the core fibers, consisting of the vertical and transverse fibers, and sheath fibers formed by the longitudinalis muscles. The fiber planes of the tongue sheath were concentric with the surface of the tongue, and locally parallel to the adjacent surface of the organ.

Quantitative distinction between the core and sheath in the anterior tongue was provided by scalar measurement of diffusion anisotropy, and was shown by a scatter plot of the diffusion anisotropy index, represented here as $f_{ind} = (\lambda_1 - \lambda_2)/\sum\lambda_n$, vs. the fiber azimuth angle relative to the antero-posterior axis (**Figure 2-7**). These data (taken from the same slice as in **Figure 2-6**) were bimodal in that voxels whose principal eigenvector was parallel to the A-P axis (azimuth angle 0°–30°, representing the longitudinal muscular sheath), had the highest diffusional anisotropy: f=0.21±0.01 (mean ± 95% confidence by t-test). Conversely, voxels whose principal eigenvector was perpendicular to the A-P axis (azimuth angle 60°–90°, such as with medial-lateral or inferior-superior fibers), showed lowest diffusional anisotropy: f = 0.21 ± 0.01.

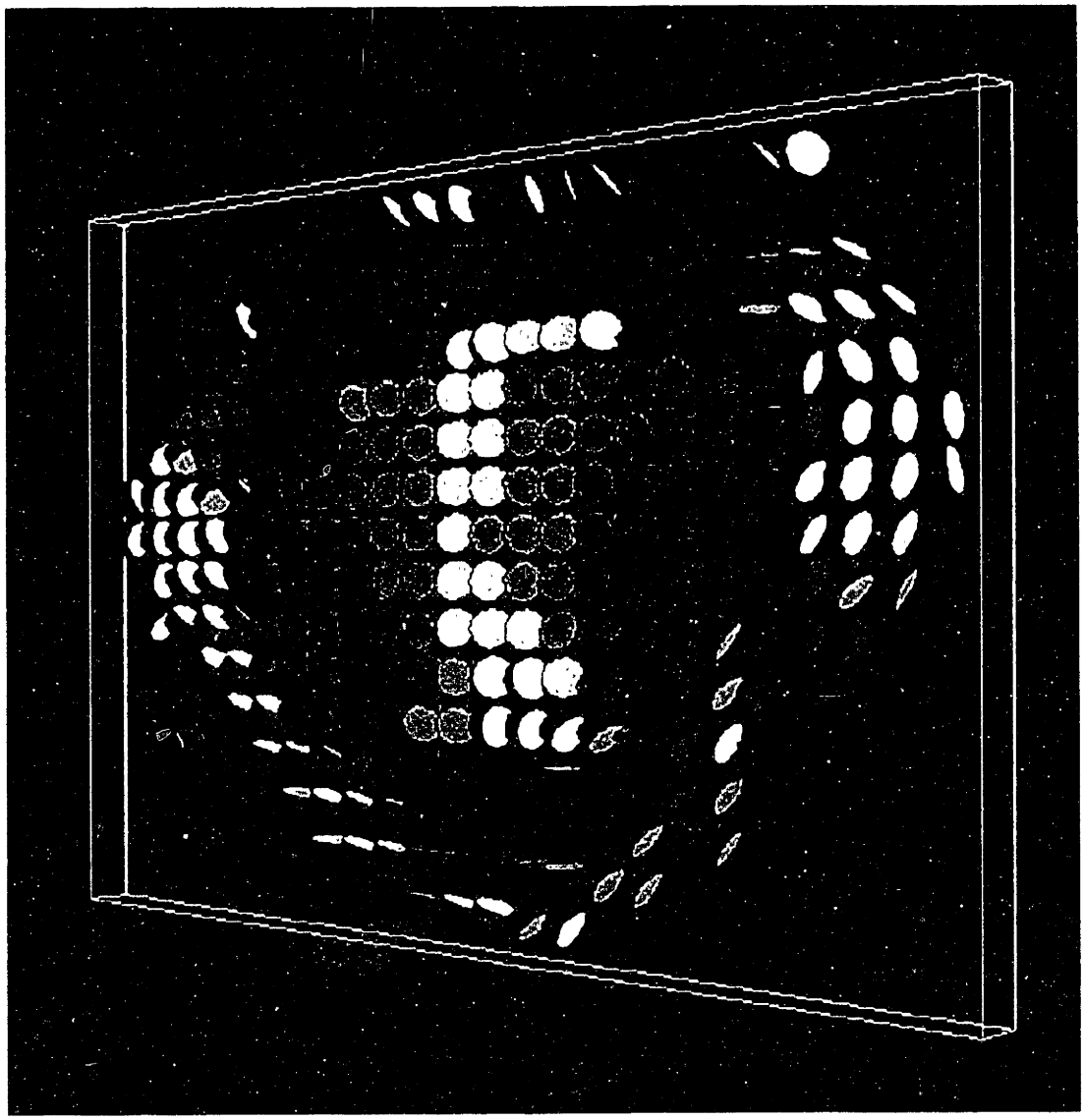

Figure 2-6 The orientation of the diffusion tensor's greatest two eigenvectors, the plane of maximum intra-voxel fiber angle dispersion, was represented by the end-planes of graphic cylinders. Contrast was seen between the tongue core, where the planes of fiber angle dispersion were transverse to the A-P axis of the tongue, and the tongue sheath, where these planes were approximately parallel to the nearby tongue surface. These data are from one representative sample (the 3rd slice from the anterior tip of the data presented in **Figure 2-5**).

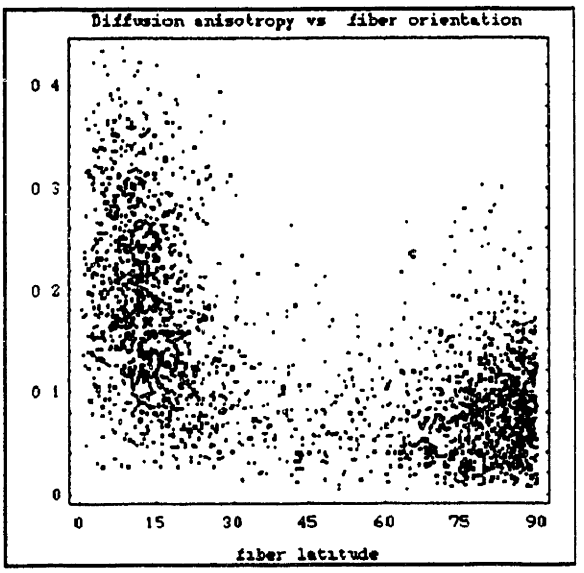

Figure 2-7 Diffusion fractional anisotropy was plotted as a function of fiber azimuth angle with respect to the antero-posterior axis of the tongue. The core, defined by fiber azimuth angle of 60° –90° had a significantly lower anisotropy, $f = 0.09 \pm 0.01$ than the sheath, defined by an azimuth of 0 – 30°, where $f = 0.21 \pm 0.01$.

2.2.3 In Vivo DTI of Human Tongue

In vivo evaluation of lingual musculature could be an integral component for patient-specific structure/function assessments, and can serve as a predictive clinical tool for diagnosing specific lingual dysphagia syndromes. From the attributes of the local diffusion tensor, one can determine an atlas of the constituting myofibers of the tongue tissue, which includes principal fiber orientation and population homogeneity/voxel (tensor anisotropy).

Normal human subjects were studied with a diffusion-sensitive stimulated-echo pulse sequence using single-shot echo-planar imaging (EPI). DTI data from the mid-sagittal slice of one representative subject (voxel size 3x3x8mm) were depicted with color-coded ocathedra, similar to the *ex vivo* DTI figures. The data presented a predominance of vertically (green) oriented fibers in the core region (**Figure 2-8**). The dorsal surface contained a thin (1-2 voxels thick) rim of fibers that followed the contour of the tongue surface. Antero-posterior (blue) directed fibers were also found on the antero-inferior surface. The fibers at the anterior base of the tissue were angled postero-superiorly, while the posterior base contained more antero-posterior oriented fibers.

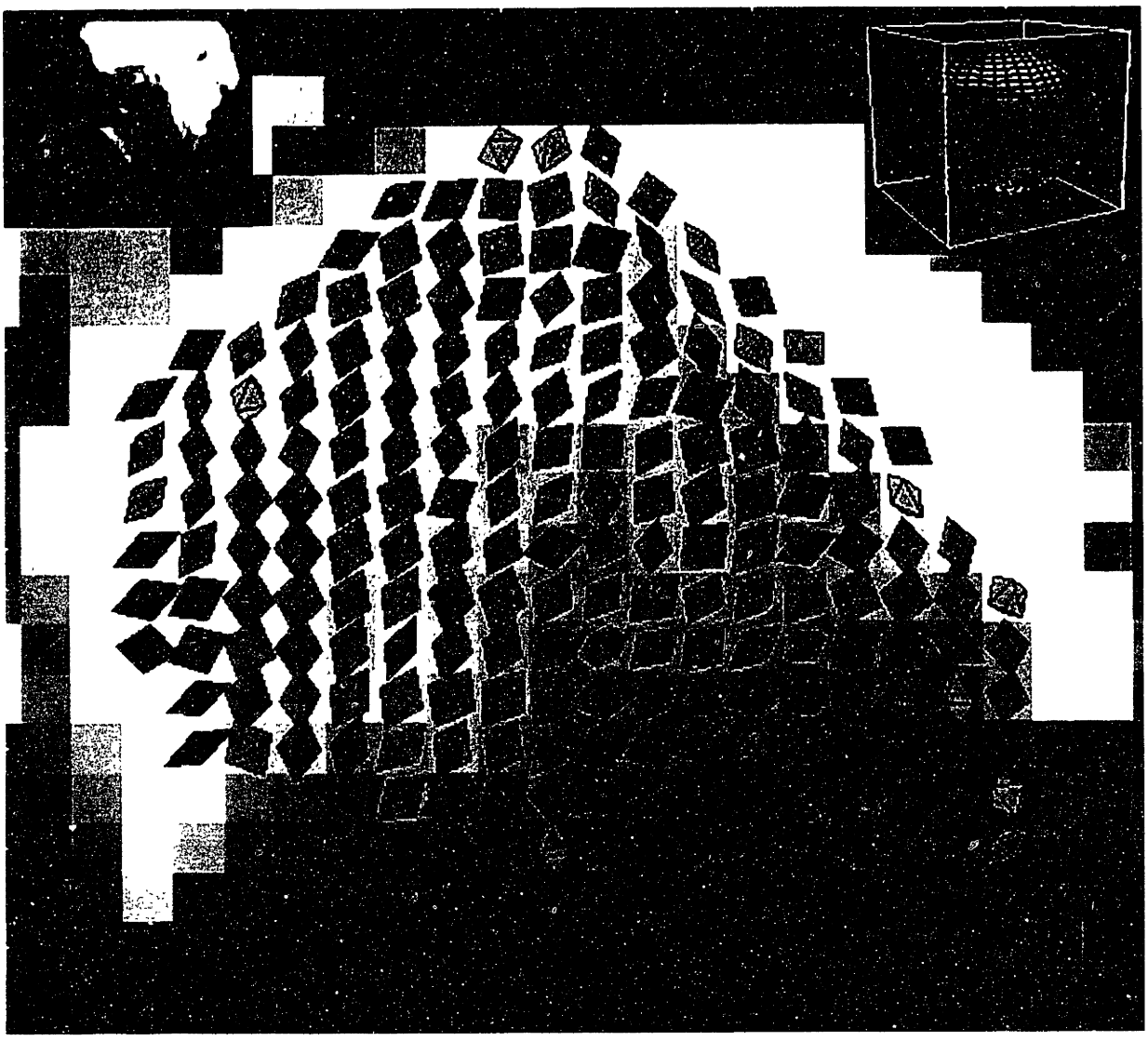

Figure 2-8 *In vivo* DTI of the normal human tongue was performed combining stimulated-echo sensitization and EPI (voxel size 3x3x8mm). DTI data were analyzed from the mid-sagittal slice (upper-left inset) and were depicted as octahedra color-coded according to the color sphere (upper-right inset). A predominance of genioglossus and verticalis fibers was evident. Dorsal surface voxels were suggestive of superior longitudinalis.

An evaluation of these data was difficult due to the lack of *ex vivo* human tongue data. However, considering the *ex vivo* bovine tongue data and known human tongue anatomy, several conclusions could be made. The vertically (green) oriented fibers in the core region were a reflection of the predominance of intrinsic verticalis fibers in the mid-sagittal plane of the core region. These data

may also represent a greater infiltration of genioglossus muscle than previously considered[1], or the confounding effect of the median septum (vertically aligned connective tissue fibers). Furthermore, previous studies were all *in vitro* histological investigations (whether human or otherwise); thus, tissue warping and shrinkage during sample preparation may have prevented past investigators from making similar observations. The rim of octahedra that follow the dorsal contour of the tongue were suggestive of the superior longitudinalis muscle. The antero-inferior (or ventral) surface of the tongue contained voxels with A-P oriented octahedra, suggestive of the inferior longitudinalis muscle. Finally, the posterior base of the tongue appeared less homogeneous in tissue orientation, though A-P (blue) octahedra did constitute a plurality. These octahedra most likely represent the horizontal component of the genioglossus (Doran and Baggett, 1972), which inserts into the posterior 1/3 of the dorsal surface, as well as the A-P directed geniohyoid fibers. The geniohyoid (O: mandible I: hyoid), with the help of the mylohyoid muscle, elevates and protracts the hyoid apparatus, raising the floor of the mouth. While constituting the floor beneath the tongue, and hence affecting its deformations, the geniohyoid is not considered an extrinsic muscle, as it connects bone to bone and does not enter the tongue proper.

The fiber populations were further analyzed in terms of their homogeneity by the extent of diffusion anisotropy (λ_1/λ_2). Anisotropy was high in the case of a single unidirectional fiber population, and low for multiple fiber populations within the sampled voxel. Depicting anisotropy in terms of gray scale intensity, high diffusion tensor anisotropy was found in the dorsal and antero-ventral periphery, corresponding to the superior and inferior longitudinalis muscles (**Figure 2-9, Figure 2-10**). The mean anisotropy in this region was found to be 1.52 ± 0.25. High anisotropy also existed at the anterior base, corresponding to the extrinsic genioglossus muscle (mean = 1.45 ± 0.15). Low anisotropy was found in the intrinsic core region, which corresponded to the location of the transversus and verticalis muscles (mean = 1.22 ± 0.10). While there was marked spread in the data, a statistical analysis demonstrated that inter-regional means were significantly different. Specifically, a student t test was performed to test for the probability that two of these regional samples came from one population with the same mean. The probability that this was the case for the longitudinalis and transversus/verticalis regions was less than 0.02%; while for the genioglossus and transversus/verticalis regions, the probability was less than 0.0001%.

[1] The genioglossus muscle has been found to constitute a larger percentage of tongue mass in humans than in other mammals such as rat, cat, and dog (Doran and Baggett, 1972). This most likely also applies to bovine tongues and may explain the discrepancy between the *in vivo* human data and *ex vivo* bovine data.

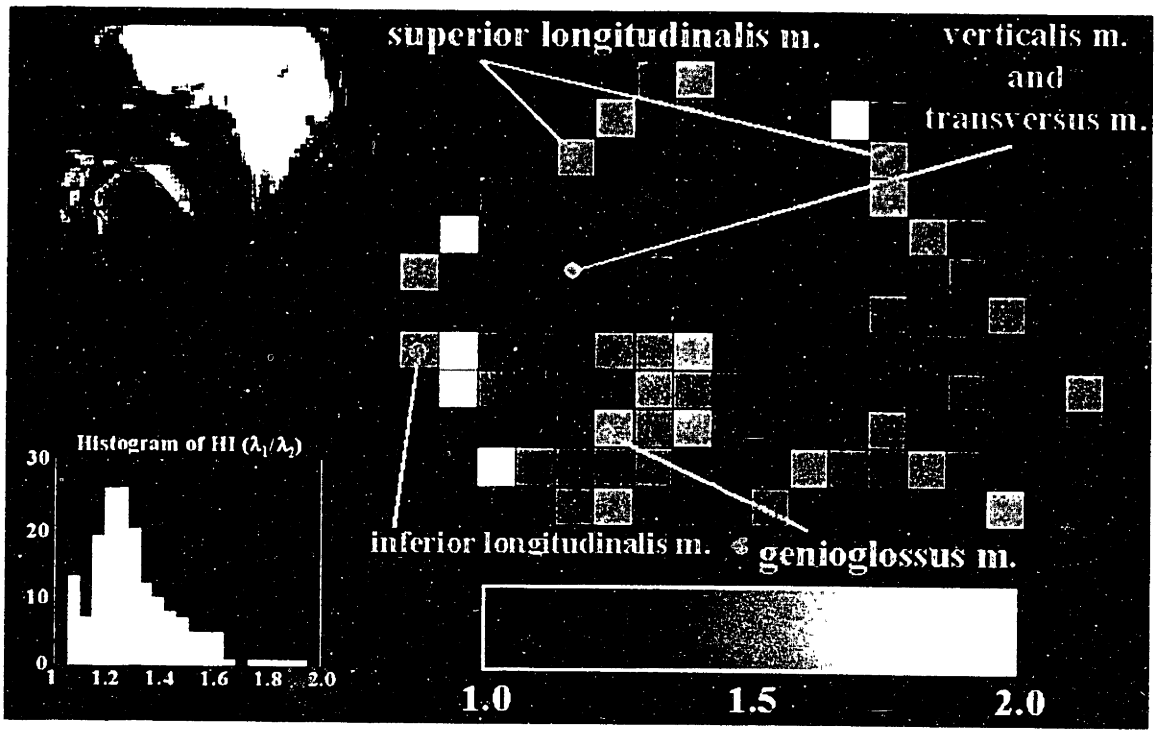

Figure 2-9 Diffusion anisotropy (λ1 λ2) was displayed as a grayscale map with lighter voxels corresponding to higher anisotropy. The analyzed region of interest was shown in the upper-left. There was a region of high anisotropy (homogeneous fiber orientation) in the dorsal and antero-ventral periphery (longitudinalis) as well as the base (genioglossus). The region corresponding to the intrinsic core possessed a generally lower anisotropy index (multiple myofiber populations). A histogram of anisotropy values demonstrated that multiple fiber population regions were more common than homogeneous muscle regions.

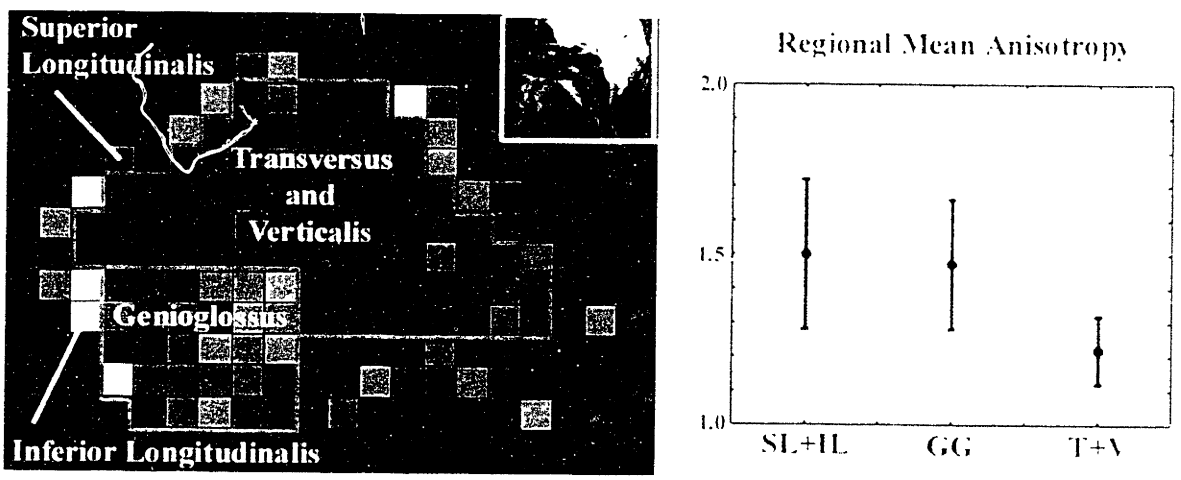

Figure 2-10 A statistical analysis of regional anisotropy differences within the human tongue demonstrated that the mean anisotropy was greater for the regions corresponding to the genioglossus (GG) and longitudinalis (SL + IL) compared to the transversus and verticalis (T+V) region. While there was marked spread in the data, a t-test concluded that the differences were statistically significant.

Applying diffusion tensor imaging in the *in vivo* human tongue is not a trivial extension of the DTI technique. Due to the existence of airspace above the tongue in the oral cavity and the nasal airspace above the hard palate, substantial susceptibility artifact (occurring at material mismatch boundaries) must be overcome. Future MR imaging studies could attempt to mitigate susceptibility artifact by using a surface coil array technique such as SENSE or SMASH to decrease readout time. Furthermore, signal to noise ratio in the tongue was comparatively low, demanding a high number of image averages and, hence longer total imaging times. To improve SNR, larger voxel size was used. However, the size of the human tongue (~ 4cm x 6cm x 9cm) necessitates a smaller voxel size than that of the larger bovine tongue (~ 8cm x 9cm x 20cm). Thus, an upper limit was used which maximized SNR while still providing adequate myoarchitecture discrimination. Future studies should attempt to capitalize on the increased SNR, and hence superior spatial resolution, available with current 3T magnets (greater field strength than the 1.5T magnets used for this study). In addition, successful image averaging relies on inter-image voxel to voxel correspondence. Seemingly minute movements due to cardiac pulsation or respiration could potentially corrupt the dataset. For our experiments, subjects had to hold the tongue steady (i.e. no speaking, masticating, or *swallowing*) for up to 5 minutes with shallow, normal respiration. This temporal constraint proved difficult for most volunteers and may be prohibitive in a patient population (n.b. subjects fared better without specific instruction to "refrain from swallowing"). While subject-to-subject reproducibility was difficult, these findings did indicate that 3D myoarchitecture could be imaged with *in vivo* DTI, providing a structural basis for understanding lingual physiology.

2.3 3D Microscopy of the Tongue

Diffusion tensor imaging had a spatial resolution of 3x3x6mm; adequate for whole tissue analysis. However, myocyte organization is better analyzed at a microscopic level. Furthermore, validation of diffusion tensor imaging requires visualization of the actual underlying myoarchitecture. While conventional microscopy techniques provide a planar snapshot of tissue structure and have been used in the past to attempt to validate DTI results (Hsu, Muzikant et al., 1998), the complex three-dimensional myoarchitecture of the mammalian tongue necessitates a 3D microscopy technique. Two-photon excitation microscopy may constitute an optimal method for visualizing *in situ* fiber architecture

due to its ability to scan a three-dimensional portion of the tissue space. This was accomplished with laser excitation configured to excite two photons at discrete locations in the tissue (Denk, Strickler et al., 1990; Masters, So et al., 1997; Centonze and White, 1998). The particular applicability of two-photon microscopy for depth discrimination in thick tissues results from the fact that fluorescence signal intensity is highly dependent on the degree of photon flux, which decreases rapidly as a function of distance from the focal plane. Thus, excitation is confined to a small enough volume to effectively remove background signal and beam scatter.

NMR (diffusion tensor MRI) and optical (two-photon excitation microscopy) techniques were combined to visualize the microstructure of the core fibers of the mammalian tongue (Napadow, Chen et al., 2001). This developed an analytic framework to test the validity and limitations of the previously presented DTI technique.

2.3.1 Two-Photon Microscopy Methodology

Two-photon excitation microscopy (excitation wavelength 780nm) was used to image lingual muscle fiber autofluorescence *in situ*. The physics behind this technique have been summarized in the appendix. Tissue specimens were imaged with a mode-locked Ti-Sapphire laser, with a 76MHz repetition rate and a 150fsec pulse width (Coherent, Inc, Palo Alto, CA). The power of the laser light source was regulated to approximately 130mW with approximately 15mW delivered at tissue level. The axial position of the objective was driven by a piezoelectric driver, with a resolution of 0.05μm over 100μm. The typical frame rate (per single image slice) was approximately 3 seconds. The 3D deep-tissue volume scans produced 256x256 images with resolution 1.85x1.85μm and a slice thickness of 5μm. Achievable scan depth into the tissue was approximately 200μm.

Image processing of the two-photon datasets was achieved via a 3D autocorrelation algorithm. The autocorrelation of an image volume was computed in order to find average repetitive structures within the image, such as homogeneously aligned fibers (Russ, 1999). Practically speaking, the Fourier transform of the image volume is multiplied by its own complex conjugate and the result inverse-transformed back to real space.

$$ACorr(g(t))_j = \int_{-\infty}^{\infty} g(\tau)g(t+\tau)dt = IFFT(G_k G_k^*) \tag{2.6}$$

where g_j is the real space image volume, and G_k is its Fourier transform. The asterisk denotes complex conjugation. Prior to transformation, image volumes were interpolated in the through-plane dimension and windowed with a Kaiser window. The former procedure was implemented because the data volume was originally spatially anisotropic, while the latter procedure accounted for the lack of periodicity in the data (i.e. no wraparound at the edges).

The center of the autocorrelation volume contained a 3D intensity distribution, which was aligned in space according to the alignment of the mean fiber populations within the original image volume. In order to compute this orientation, we calculated the Hessian matrix at the center voxel of the autocorrelation volume:

$$\mathbf{H} = \begin{bmatrix} I_{xx} & I_{xy} & I_{xz} \\ I_{yx} & I_{yy} & I_{yz} \\ I_{zx} & I_{zy} & I_{zz} \end{bmatrix} \tag{2.7}$$

Discrete derivatives were computed with a higher order five-point scheme with error $O(h^4)$. The eigensystem of the Hessian was then found and the eigenvector corresponding to the smallest eigenvalue (in absolute value) conferred the direction of lowest curvature, which by extension was the mean 3D fiber orientation within the sampled image subvolume.

Two-photon image datasets (n=5) were first filtered with blind deconvolution to correct for an asymmetric excitation point-spread function (AutoDeblur, AutoQuant Imaging Inc., Watervliet, NY). This dataset was then divided into 50 x 50 x 9 voxel subvolumes, which were analyzed by the previously described autocorrelation algorithm. A total of n=63 subvolumes were analyzed and data were presented in table format with comparisons to DTI data taken from the same tissue region.

2.3.2 Microscopy of *Ex Vivo* Bovine Tongue

Tissue specimens (20 x 20 x 8 mm) were obtained from the core of the anterior region of the tongue, and were either fixed (10% gluteraldehyde) and embedded in paraffin, or viewed as fresh tissue, without fixation. For the fixed tissue, following 3D microscopy, the tissue was sliced with a microtome (Olympus) to a thickness of 0.4 μm, stained with either hematoxylin/eosin or trichome, and viewed with conventional light microscopy.

The 3D distribution of individual myofibers within the lingual core was visualized with two-photon excitation microscopy utilizing the autofluorescence of fixed tissue specimens. In contrast,

fresh tissue did not produce sufficient autofluorescence to allow adequate single fiber discrimination. While unconfirmed, we hypothesized that the gluteraldehyde used in the fixation process induces a reduction reaction with the lingual tissue, producing a structure-dependant dispersion of fluorophores. For our purposes it was unimportant what was fluorescing, as long as the fluorescing molecules accurately described the underlying myoarchitecture. Volume content determined by two-photon microscopy was compared to a histological assessment of similar tissue using H&E. Trichrome stains also confirmed that the imaged structures were principally skeletal muscle, with minimal collagen.

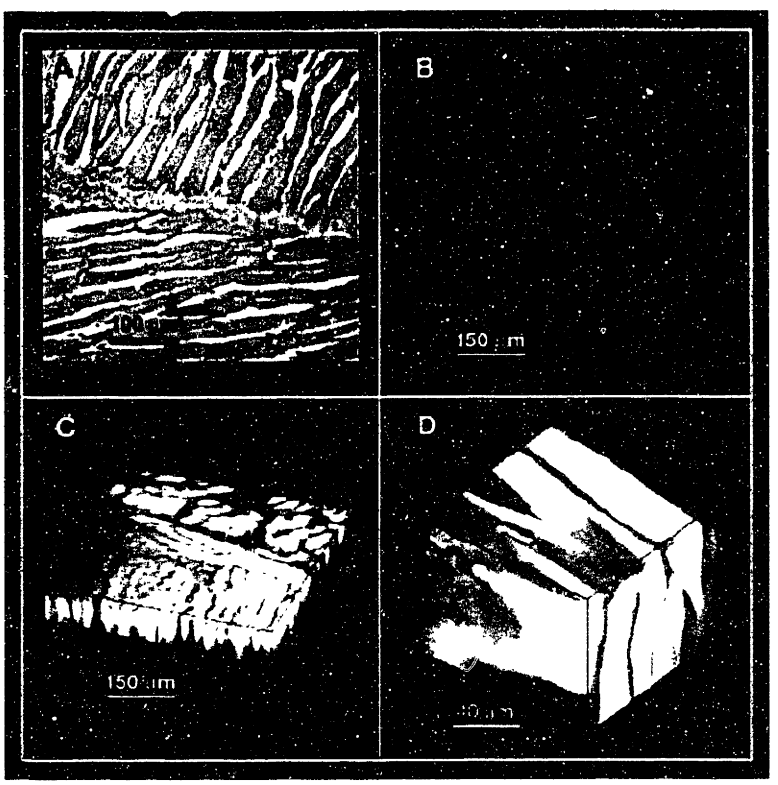

Figure 2-11 The 3D distribution of individual myofibers within the porcine lingual core was visualized with two-photon excitation microscopy utilizing fixed tissue specimens (100x and 400x, C and D respectively). In contrast, fresh tissue did not produce sufficient autofluorescence to allow adequate single fiber discrimination (B). Volume content determined by two-photon microscopy was compared to a histological assessment of the same tissue using H&E (100x, A). The secondary organization of lingual core myofibers resembled a patchwork of fiber bundles (A and C).

2.3.3 Comparison of 3D Microscopy with DTI Results

Diffusion tensor imaging and two-photon microscopy were applied to the same mammalian tongue tissue sample (Napadow, Chen et al., 2001). The goals of this study were to better analyze myocyte organization at a microscopic level, as well as to validate the DTI results.

Two photon excitation microscopy was preformed on 3 excised porcine tongues, while both microscopy and DTI were performed on one additional tongue for future comparison. The porcine tongues were obtained from Blood Farms (West Groton, MA) where the tongue was excised by exposing the tongue with an incision from the thyroid prominence to the angle of the mandible, followed by en bloc resection. Whole tongue specimens were refrigerated and scanned within 24 hours of harvest. For microscopy, tissue specimens (20 x 20 x 8 mm) were obtained from the tongue's anterior core, visually localized to correspond to the region from which diffusion tensor data were acquired. The tissue specimens for three-dimensional microscopy were fixed (10% gluteraldehyde) and embedded in paraffin.

Mean 3D-fiber orientation within the two-photon datasets was computed with an autocorrelation algorithm. A sample image and its 3D autocorrelation volume is presented in the xy, xz, and yz projections, with the computed orientation vector superimposed (**Figure 2-12**).

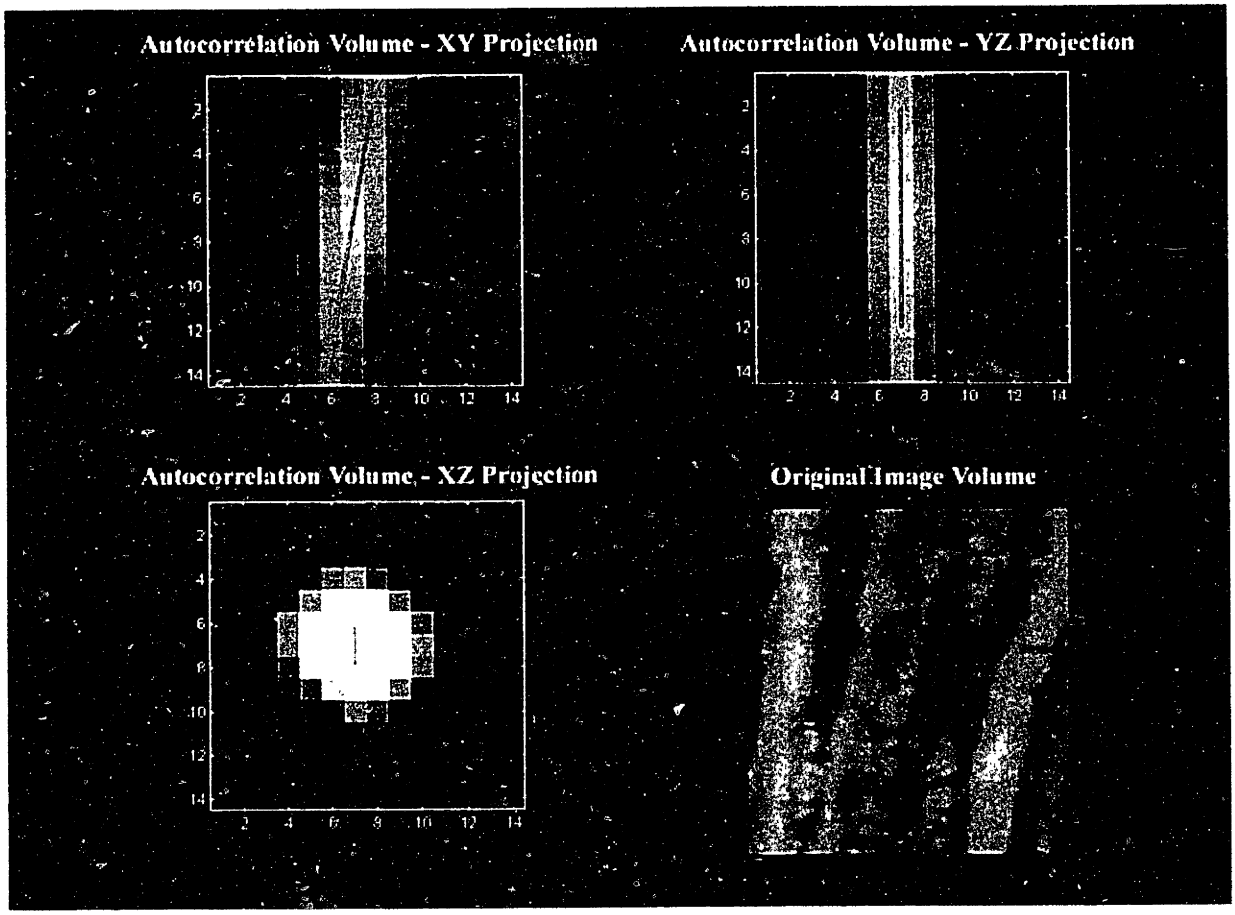

Figure 2-12 Mean 3D fiber orientation within the two-photon datasets was computed with an autocorrelation algorithm. (D) sample image dataset shown on end. (A-C) The dataset's 3D autocorrelation volume presented in xy, xz, and yz projections, with the computed orientation vector superimposed (red).

Diffusion Tensor Imaging was performed on whole porcine tongue specimens with a 1.5T Siemens Vision System equipped with head coil. A double-echo EPI sequence was utilized (TR/TE 5000/100 msec) with an image matrix of 96x128, corresponding to a phase-encoded interpolated voxel resolution of 1.95 x 1.95 x 8.00 mm. The double-echo sequence was utilized to limit image artifact produced by deleterious eddy currents resulting from gradient switching and corresponded to a b-value to 620 s/mm^2 (gradient strength = 18 mT/m, Δ = 15.79msec, Δ = 14.47msec, Δ = 15.79msec, δ = 12.67msec).

The complete 3D diffusion tensor was computed for each image voxel and was visualized as an octahedron icon, whose axes were scaled by the size of the eigenvalues and oriented along the corresponding eigenvectors (**Figure 2-13**). Only voxels with significant fiber content (i.e. anisotropy index as ratio of eigenvalues λ_1 / λ_2 > 1.15) were included in the analysis. A total of n = 15 tensors were

analyzed for correlation with two-photon microscopy. The mean fiber orientation for each voxel was calculated and the data presented in two ways: as a cubic spline-smoothed polar histogram plot and in table format.

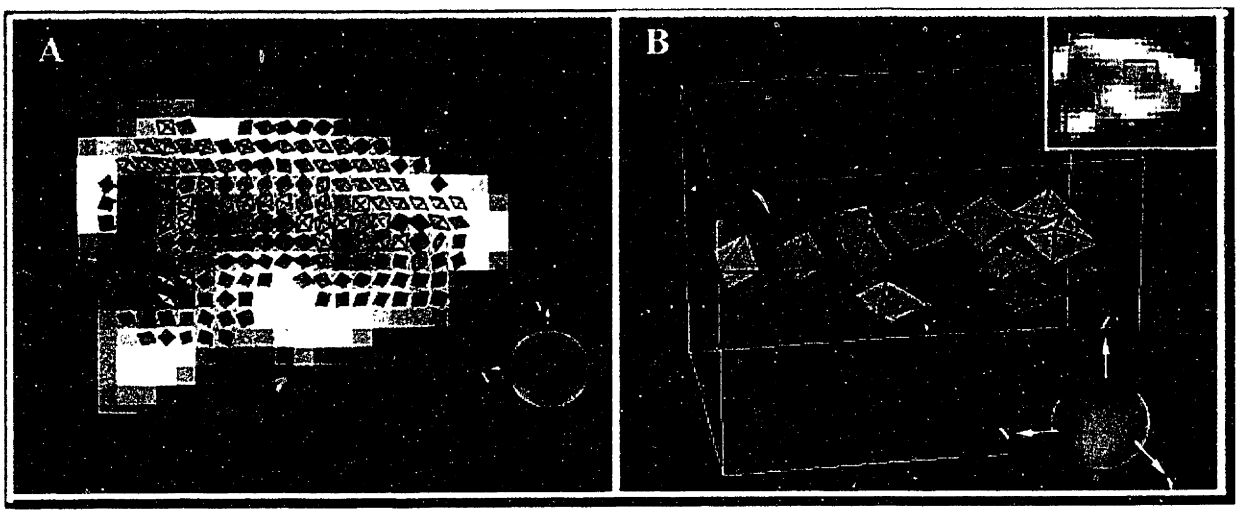

Figure 2-13 Diffusion Tensor Imaging was performed on an axial slice of the porcine tongue. The diffusion tensors are shown as octahedra oriented along the eigenvectors of the diffusion tensor, and color-coded according to the orientation of the principal eigenvector. (A) The entire axial slice was composed of a core region of in-plane fibers oriented approximately orthogonal to each other (red and green) corresponding to the verticalis and transversus muscles, and a peripheral region of longitudinally oriented fibers (blue). (B) The region later sampled with two-photon microscopy was comprised of orthogonally oriented fiber populations (red and green), mostly in-plane to the imaging slice.

Both diffusion tensor imaging (n=15) and two-photon microscopy (n=63) exhibited two distinct fiber populations (**Figure 2-14, Table 2-1**). By DTI, one composite fiber population was oriented in-plane at −16.8° relative to the horizontal, while another composite fiber population was oriented at 65.4°, yielding a relative in-plane fiber angle of 82.2°. Similarly with two-photon microscopy, the transversus fiber population was oriented in-plane at 3.6° relative to the horizontal, while the verticalis fiber population was oriented at 84.0°, corresponding to a relative in-plane fiber angle of 80.4°. Moreover, sampling from both diffusion tensor imaging and two-photon microscopy supported the consistently in-plane fiber orientation of the anterior tongue core, as mean through-plane angle was 1.3° (σ = 9.4°) and -0.3° (σ = 5.1°), respectively.

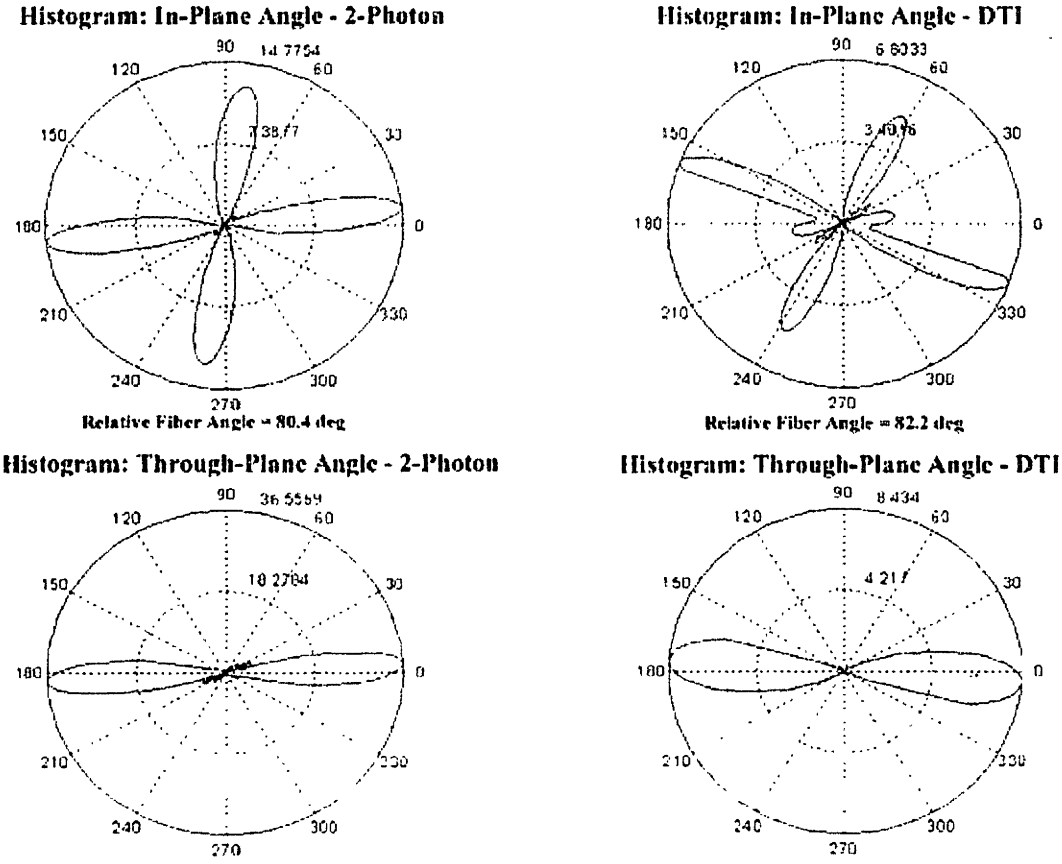

Figure 2-14 Polar histogram plots of in-plane and through-plane fiber angle represent the data gathered by both DTI and 2-photon microscopy for the same tongue sample. Both diffusion tensor imaging (n=15) and two-photon microscopy (n=63) demonstrated two distinct fiber populations. By DTI, the relative in-plane fiber angle was 82.2°, while for two-photon microscopy, the relative in-plane fiber angle was 80.4°. Both imaging modalities supported the consistently in-plane fiber orientation of the anterior tongue core, as mean through-plane angle was 1.3° (σ = 9.4°) and -0.3° (σ = 5.1°), for DTI and 2-photon respectively. The plots were smoothed with cubic splines

Comparison of muscle fiber orientation with DTI and two-photon microscopy					
Diffusion tensor imaging (n=15)			**2-photon microscopy (n=63)**		
Fiber Population	***Mean***	***St. Dev.***	**Fiber Population**	***Mean***	***St. Dev.***
Composite Fiber Pop. 1 In-Plane Angle (n=9)	-16.8°	13.8°	**Transversus m. In-Plane Angle (n=35)**	3.6°	15.4°
Composite Fiber Pop. 2 In-Plane Angle (n=6)	65.4°	5.7°	**Verticalis m. In-Plane Angle (n=28)**	84.0°	10.2°
Relative Angular Separation	*82.2°*	--	**Relative Angular Separation**	*80.4°*	--
Combined Through-Plane Angle (n=15)	1.3°	9.4°	**Combined Through-Plane Angle (n=63)**	-0.3°	5.1°

Table 2-1 Quantitative data analysis from the diffusion tensor imaging (n=15) and two-photon microscopy (n=63) datasets is presented as a table of in-plane and through-plane angle. Both imaging modalities presented two distinct fiber populations – the transversus muscle and the verticalis muscle. For DTI, the two populations were referred to as "composite fiber populations" due to the confounding nature of DTI in heterogeneous tissue regions (see below). Relative in-plane fiber angle found with DTI was 82.2°. Similarly, the relative in-plane fiber angle found with two-photon microscopy was 80.4°. Sampling from both diffusion tensor imaging and two photon microscopy supported the consistently in-plane fiber orientation of the anterior tongue core, as mean through-plane angle was 1.3° (σ = 9.4°) and -0.3° (σ = 5.1°), respectively.

The results confirmed the classical anatomical description of the lingual core as two distinct in-plane fiber populations, specifically the intrinsic transversus and verticalis muscles. Based on diffusion tensor imaging, we discerned a near orthogonal angular separation between these fiber populations. This orthogonal relationship was recapitulated at the microscopic level, thus indicating that the orthogonal relationship between fibers or fiber bundles exists as a repeating event throughout the tissue. Through two-photon microscopic imaging, we were able to discriminate the explicit 3D structural basis for the orthogonal fiber relationship. As was shown in **Figure 2-11**, the fibers in the lingual core region were not, in fact, aligned as interwoven individual fibers, but rather were organized into fiber bundle sheets. The composition of the mammalian tongue core is likely to incorporate serially alternating sheets of transversus muscle and verticalis muscle, which, at least in the case of the canine tongue, traverse the entire intrinsic core region (Mu and Sanders, 1999). The exact size and geometry of the bundles could not be determined from the data, since the slicing technique allowed for the possibility that a given axial slice holds any number of verticalis or transversus bundles. However, other investigators have estimated that the number of repeating fiber bundle sheets approaches 100 in the human (Takemoto, 2001).

Fiber orientation as conceived at a macroscopic level through depiction of the NMR diffusion tensor, differed fundamentally from the determination of fiber orientation, conceived at a microscopic level through two-photon microscopy. In the case of NMR diffusion tensor imaging, since the two fiber populations of the lingual core were nearly orthogonal to one another, and the b-value employed was relatively low, the principal eigenvector of the diffusion tensor tended to alternate between two orientations (see **Figure 2-13**). The low anisotropy present in the sampled voxels confirmed the existence of more than one fiber population (Wedeen, Reese et al., 2001). Furthermore, with two fiber populations, estimating fiber orientation with a single second-order tensor will produce a result somewhere in between the two populations, as the diffusion influenced NMR signal equation is based on a non-linear summation of the two populations, under the slow exchange hypothesis:

$$\frac{S_1}{S_0} = f_1 e^{-k_1^T \mathbf{D}_1 k_1 \tau} + f_2 e^{-k_1^T \mathbf{D}_2 k_1 \tau} \tag{2.8}$$

where S_1 denotes the NMR echo peak intensity corresponding to the gradient direction given by $\mathbf{k}_1$ (one of six different gradient directions), S_0 denotes the intensity without a diffusion sensitization gradient. f_1 and f_2 denote the respective fiber fractions of the two populations ($f_1 + f_2 = 1$), $\mathbf{k}_1$ is the spatial modulation vector given by $\mathbf{k}_1 = 2\pi\gamma_H t_d \mathbf{G}_1$ (γ_H is the proton gyromagnetic ratio, t_d is the diffusion time, and $\mathbf{G}_1$ is the magnetic field gradient). $\mathbf{D}_i$ is the second-order diffusion tensor corresponding to the i^{th} fiber population and τ denotes the diffusion sensitization gradient spacing for a classic two gradient experiment.

In order to analyze the resolving power of DTI for structural heterogeneity, a computer simulation was performed which modeled tissue with two fiber populations of equal fiber fraction (**Figure 2-15**). Each actual fiber population was modeled by a single diffusion tensor ellipsoid whose principal eigenvalue was 3 times greater than the second or third eigenvalue. The two populations were oriented 80° apart, which was comparable to the actual tongue core tissue as visualized with two-photon microscopy. The standard 7 point diffusion tensor experiment was simulated by setting the sum of these two exponentials[1] equal to the signal due to a single composite diffusion tensor (that which would be measured by the DTI experiment). A system of non-linear equations was then solved for the composite tensor. The results showed that for equal fiber fraction, the predicted tensor orientation would be exactly between the two actual fiber populations, resulting in significant error relative to either population (40° in this case). An explicit correction to the DTI data could indeed be made if both

fiber fraction and relative angular orientation were known for every voxel sampled. However, as this information is unknown, it must be stressed that only the plane in which the two actual fiber populations lie can be definitively deduced from the DTI data; it is the plane defined by the first two tensor eigenvectors and was found to be "in-plane." Furthermore, the reason that the principal eigenvector of the diffusion tensor toggles between two distinct states was due, serendipitously, to the near orthogonal nature of the two actual fiber populations. Since the diffusion tensor's principal eigenvector will nearly bisect the acute angle formed by the fiber crossing, the Cartesian quadrant in which that eigenvector will land is dependent on the quadrant in which the acute angle of the fiber crossing is located. That is, if the transversus muscle is defined to lie along the x-axis in a standard Cartesian x-y coordinate system, and the verticalis muscle is at 80°, the bisected angle will be 40°. However, if that verticalis m. population is now at 100° (note that the fiber crossing angle would still be the acute 80° angle), the bisected angle along which the diffusion tensor's principal eigenvector now lies would be 140°. In fact, a singularity exists if the fiber crossing angle is exactly 90° (**Figure 2-15**). This phenomenon explains the toggling nature of the octahedra in our DTI data, and the reason why the term "composite fiber population" was used in **Table 2-1**.

[1] These two exponentials defined the NMR signal intensity corresponding to the two populations

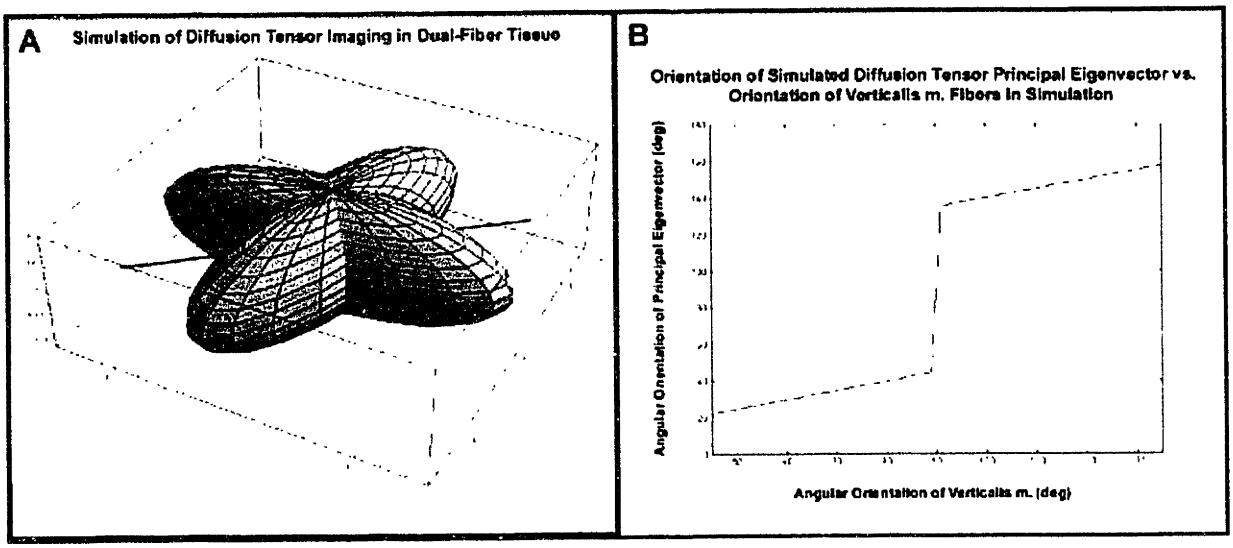

Figure 2-15 A Computer simulation showed error in using DTI to calculate fiber direction for tissue with multiple fiber populations. (A) Computer modeling of two equally distributed fiber populations oriented 80° apart in-plane and modeled by a single diffusion tensor ellipsoid (seen in the figure). A standard 7 sample DTI experiment produced a single diffusion tensor whose principal eigenvector was exactly between the two actual fiber populations (red line segment) – a 40° error relative to either actual fiber population. B) A graph of the DTI simulated experiment demonstrates the change of the diffusion tensor's principal eigenvector in response to varying the relative angular orientation of the tongue's two intrinsic myofiber populations. If the transversus muscle is defined to lie along the x-axis and the verticalis muscle is varied from 45° to 135°, the orientation of the diffusion tensor's principal eigenvector will "jump" from 45° to 135° as the verticalis orientation passes through 90°. This phenomenon was due to the fact that the principal eigenvector will bisect the *acute* fiber crossing angle, and explains the toggling nature of the octahedra in our DTI data.

Limitations in the current DTI technique may be improved by several means. If we assume a diffusion time on the order of 100 msec (as calculated from the EPI pulse sequence), and diffusivity of 2.2 x 10^{-3} mm^2/s which is typical of skeletal muscle, the rms diffusion length ($x_{rms} = (2\mathbf{D}t)^{1/2}$) is approximately 20 μm. This relatively short diffusion length would most likely limit proton movement through the semi-permeable sarcolemma of the myofibers; which are 20-80 μm in diameter, hence mitigating the distinction between aligned and fiber patches and continuously interwoven fiber network. Further experiments may take advantage of longer mixing times in the DTI pulse sequence to ascertain the properties of the diffusion tensor (anisotropy, orientation) at varying diffusion times. Longer diffusion times should increase tensor anisotropy as fiber barriers are encountered by a greater number of protons diffusing orthogonal to the long axis, while motion along the fiber axis remains less restricted (Basser, Mattiello et al., 1994). In the extracellular space, proton displacement should also be more anisotropic at longer diffusion times. Movements across and through the myofiber patches would be hindered to a greater degree than displacements along the axes of individual fibers. Thus, the second eigenvector of the diffusion tensor may point across the myofiber patch (orthogonal to the fiber

direction) or orthogonal to both the fiber direction and patch plane. The extent to which diffusion is affected by the stoma of blood vessels or nerves surrounding the fibers is also unknown. With our current voxel resolution, this latter question is difficult to answer, as a single voxel may have multiple heterogeneously aligned patches, and DTI accounts only for the mean diffusivity within that voxel. Hence to answer this question, DTI voxels need to be co-registered precisely with the microscopic field-of-view and the two must be conceived on similar length scales.

Viewed from the perspective of the whole muscle, DTI effectively depicted regions of high and low anisotropy, a fact which may have particular relevance when considering the behavior of tissue undergoing stimulated proliferation or pathological remodeling. DTI was most accurate in resolving fiber direction and in defining constituent fiber population when the tissue was most spatially homogeneous, i.e. possessing high diffusion anisotropy. However, the resolution of fiber direction by DTI was more limited in tissues whose fiber populations were spatially heterogeneous, i.e. possessing low diffusion anisotropy[1]. Analysis of fiber orientation in spatially heterogeneous tissues was most aptly discerned by microscopic methods. The combination of diffusion tensor imaging and two-photon microscopy; therefore, provides a robust method for characterizing heterogeneous architectural environments in biological tissues, inasmuch as structural organization can be considered at varying length scales in the same specimen.

The physiological implications of these results will be more thoroughly discussed in chapter 3 and 4, however a brief discussion is warranted here. Similarly oriented fiber bundles may either act *en masse* as distinct contractile units, or serve to localize a portion of a myofiber population's fibers into a specific region so that regional contraction employs fibers from different fiber populations. During physiological motions, the efficient execution of different lingual tasks most likely employs a combination of both these strategies. For instance in human swallowing, serially alternating transversus and verticalis bundles may allow for the bolus accommodating depression in the tissue to translate posteriorly, bringing food deeper into the oropharynx. Both fiber populations are necessary as verticalis muscle contraction allows for a depression to be formed, while transversus muscle contraction creates orthogonal expansion toward the hard palate, thus following the principles of a muscular hydrostat.

[1] This issue was further addressed via Diffusion Spectrum Imaging in the "Future Directions" section of Chapter 5.

Chapter 3

3 Deriving Lingual Physiology with Tagging MRI

Livingston, 1956, stated that "before the tongue can increase its usefulness it must increase its mobility" (Livingston, 1956). In deglutition, the tongue acts to contain and propel a bolus of food, whereas in phonation, the tongue assumes stereotyped conformations that determine vocal tract shape. The determination of tongue mechanics associated with these physiological functions requires an analysis of internal muscular dynamics, not just a characterization of external tongue contour. Previous studies of tongue mechanics have utilized such techniques as direct observation, wherein the investigator studied the conformations of the tongue in partially edentulous (toothless) subjects after having them part their lips (Abd-El-Malek, 1955). More modern technologies have included video-fluoroscopy (Cook, Dodds et al., 1989; Dodds, Stewart et al., 1990; Kahrilas, Logemann et al., 1992), video-fluoroscopy with ultrafast CT (Kahrilas, Lin et al., 1993), sonography (Shawker, Sonies et al., 1984; Hamlet, Stone et al., 1988; Stone, 1990; Wein, Bockler et al., 1991), magnetic markers (Perkell, Cohen et al., 1992), or magnetic resonance imaging (Gilbert, Daftary et al., 1998) to determine tongue contour and to theorize about the underlying muscular activity. However, due to the redundancy of muscular elements found in the tongue, it is difficult to determine internal contraction patterns solely through measures of external shape. This critical point was the motivation for the current research effort.

To address this issue, various methods have been developed in the past to resolve internal tissue deformation, although each has limitations. Finite element modeling has successfully portrayed the theoretical internal mechanics of the tongue, but has been compromised by model instability when setting optimization functions and incorporating the proper anatomy (Hashimoto and Suga, 1986; Wilhelms-Tricarico, 1995; Sanguineti, Laboissiere et al., 1997). Similarly, attempts using simplified geometrical analog modeling have provided only a global understanding of tissue physiology (Chiel, Crago et al., 1992). Past empirical methods have been limited by inadequate temporal or spatial resolution. For example, studies exploring tongue deformation with fluoroscopy and implanted metal

markers (surgical wire or injected solder) detailed broad mechanisms of tongue protrusion in animal models (Smith, 1984; Hiiemae and Crompton, 1985; Smith, 1986), but were limited in spatial resolution and, due to the invasive nature of the method, could not be extended to humans. Electromyography (EMG) studies of the genioglossus with intraoral (Doble, Leiter et al., 1985) or intramuscular (Sauerland and Harper, 1976; Krol, Knuth et al., 1984) wire electrodes have yielded insight into gross myoelectric activity and physiologic muscle recruitment. However, intramuscular electrodes are invasive in nature and ambiguous in signal source. Intraoral (surface) electrodes are less invasive, but are limited to testing only surface myoelectric activity, which introduces difficulty in deriving distinct fiber population activity in an organ with such a compact, interwoven muscular mesh.

Direct methods for non-invasive measurement of muscle deformation have been developed using various magnetic resonance imaging techniques, such as phase-contrast imaging, to derive strain rates (Wedeen, 1992; Drace and Pelc, 1994). Another MRI method is to apply rectilinear magnetic tags that deform with deforming tissue (Zerhouni, Parish et al., 1988; Axel and Dougherty, 1989; Young and Axel, 1992; Azhari, Weiss et al., 1993; Young, Axel et al., 1993). This technique has been termed SPAMM, or Spatial Modulation of Magnetization, and has been applied to study cardiac strain and contractility, but certain caveats do exist. While strain constitutes a measure of localized deformation, it is only a secondary marker of contraction or relaxation. For instance, contracting fiber bundles, such as fibers of the extrinsic palatoglossus or styloglossus, can deform adjacent regions in the tongue (and induce compressive strain) in the absence of direct muscular contractions in those regions. In the current study, the technique of tagged magnetization was extended to assess regional strain in the tongue during *in-vivo* physiological motion. The technique was further optimized by maximizing the number of tracked deforming elements and providing quantification of discrete element deformation with spatially resolved strain mapping. Three cardinal motions of the tongue were studied: protrusion out of the oral cavity, protrusion with lateral bending, and sagittal bending with tongue tip toward the hard palate. These motions can be considered foundations of the more complex physiological motions involved in deglutition and phonation.

As intramural strain during deglutition was also investigated in this thesis, a brief review of the swallow is warranted. The human swallow is divided up into three stages: the oral (~1sec.), the pharyngeal (<1sec.), and the esophageal (~6-8sec.). The tongue is involved in the first two stages, undergoing a stereotypical sequence of muscular deformations (**Figure 3-1**). The ingested bolus is initially contained in a groove-like depression in the middle dorsal surface of the tongue (early accommodation). The tongue tip is thrust against the upper incisors and hard palate while the tongue sides contact the hard palate in the molar region. Pressure exerted by the tongue tip has been estimated

to be 75 ± 50 g/cm^2, while the tongue sides exert pressures closer to 140 ± 50 g/cm^2 (Proffit, 1973). These actions effectively contain the bolus and seal off anterograde flow. The surface depression on the lingual dorsum is then translated posteriorly in a progressive distal squeezing of the tongue against the hard palate (Lowe, 1981). The bolus then reaches the posterior edge of the tongue (late accommodation). Finally, the oral stage of the swallow is concluded by the rapid clearance of the bolus retrograde into the oropharynx at speeds approaching 100 cm/s (Miller, 1982). During the pharyngeal stage, the bolus is stripped from the walls of the pharyngeal chamber by the persistent action of the tongue against the contracting constrictor muscles (Lowe, 1981). It was once thought that negative pressure was the main pulsive force responsible for deglutition (Barclay, 1929); however that hypothesis has been disproved, and it is now known that the tongue provides an active pulsive force to the bolus (Pouderoux and Kahrilas, 1995). The extent of muscular tissue deformation may vary under normal conditions as a function of bolus volume (Dantas, Kern et al., 1990) or viscosity (Pouderoux and Kahrilas, 1995), whether the bolus is solid, liquid, or even a sword (Devgan, Gross et al., 1978). Muscular deformation may also be modified by pathological effects on muscle contractility and/or neuromuscular regulation (Miller, 1982). Abnormal swallowing is known as dysphagia, which is classified as a symptom and suggests the existence of underlying disease. Technically, dysphagia is defined as an "abnormality in the transfer of a bolus from the mouth to the stomach" (Groher, 1997).

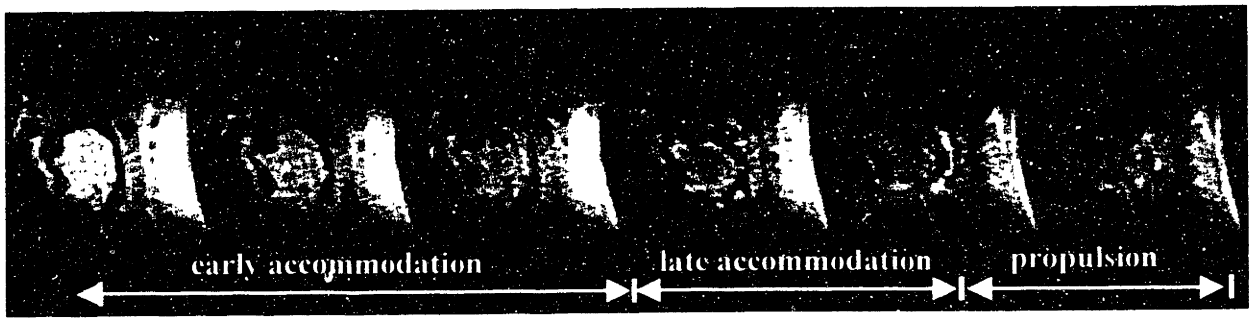

Figure 3-1 A sequence of mid-sagittal images of tongue deformation acquired at 10 Hz using a HASTE MRI pulse sequence depicts early accommodation, late accommodation, and propulsion. The subject is swallowing a 10ml bolus of water.

3.1 Tagging MRI Methodology

The methodology for applying this technique involves both the application of the proper MRI pulse sequence, as well as the post processing analysis of the deformed grid images. These two components will be discussed in turn in this section.

3.1.1 Magnetic Resonance Imaging

MR imaging was performed with a 1.5 Tesla Siemens Vision MRI system and an anterior neck coil using a single-shot fast asymmetric gradient echo pulse sequence. The imaging parameters were as follows: TR/TE 2.25/0.8 msec, matrix size 80 x 128, slice thickness 10 mm, and effective image spatial resolution 1.33 x 1.33 mm. The imaging pulse sequence was preceded by 90° RF tagging pulses which served to saturate the longitudinal magnetization of the affected tissue (**Figure 3-2**).

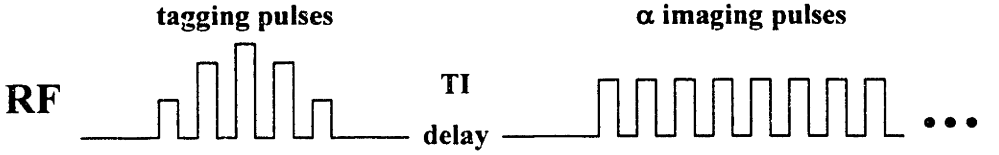

Figure 3-2 The tagging pulse sequence was compiled by first producing 90° saturation radiofrequency (RF) pulses, followed by a series of α imaging pulses, thereby visualizing the MR tagging grid. The tissue deformed during the TI delay time.

The tagging pulses were arranged in a 1-4-6-4-1 power configuration to simulate a sinc shape. The summation of the entire tagging pulse train amounted to a 90° pulse; that is, it would flip the magnetization vector of the tagged tissue completely onto the transverse plane, thus saturating the effected magnetic spins. The Fourier transform of the comb function in a sinc envelope is an equally spaced, constant intensity banded grid. Hence, this sequence was applied in two orthogonal directions to comprise a square, rectilinear tagging grid (**Figure 3-3**). The spacing of the tags on the image could be altered by altering the spacing of the tagging RF pulses, while the width of the tags could be altered by altering the width of the entire tagging RF pulse train. Tongue tagging was completed with tags spaced 7mm apart. The imaging portion of the sequence (TurboFLASH), consisted of small flip angle (8°) alpha pulses which provided enough transverse magnetization to

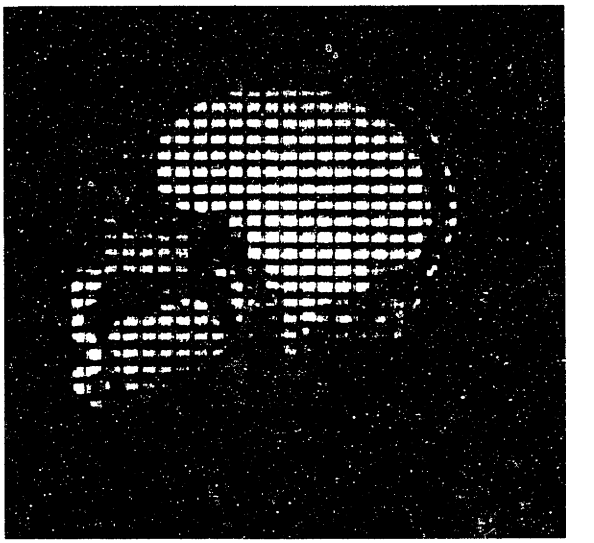

Figure 3-3 Tagging MRI with undeformed grid

produce an asymmetric gradient echo. The entire imaging portion of the sequence lasted 180ms. K-space (frequency domain) was traversed asymmetrically (half Fourier space sampling) with 80 phase encode steps and 128 frequency encode samples. The image was then reconstructed with an inverse Fourier transform of the data from half of the frequency space. It is important to note that the entire sequence was "single-shot"; that is, no averaging, partial k-space reconstruction, or gating was necessary.

Since the relative brightness of a pixel (in a proton density weighted image) is due principally to the amount of longitudinal magnetization just prior to the imaging pulse sequence, tissue affected by the tagging pulses appeared dark in contrast to the surrounding tissue. The tagged tissue's longitudinal magnetization decays back to M_0 exponentially with rate constant T_1 (**Figure 3-4**). Thus, T_1 limits TI, the length of delay time from tagging to imaging (when the motion occurs), and also limits the maximum duration of physiologic motion that can be studied. T_1 for tongue skeletal muscle was found to be 870ms, and maximum TI was approximately 1100 ms.

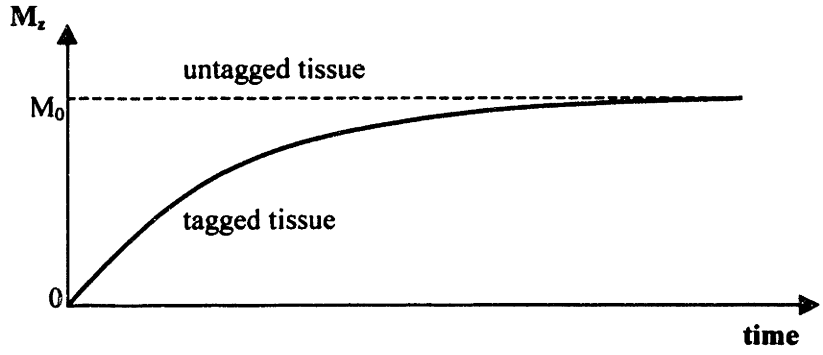

Figure 3-4 This graph presents the effect of RF tagging pulses on M_z, the longitudinal magnetization. The difference between the tagged and untagged tissue curves represents tag contrast.

3.1.2 Post Processing Data Analysis

Derivations for the following methodology have been included in **Appendix D**. Deformation was quantified in image post-processing with measures of non-linear strain, a unitless measure of localized deformation. Inasmuch as relatively large strains were predicted for this tissue, the non-linear Green's strain tensor was used:

$$\mathbf{E}_{\text{Green}} = \frac{1}{2}\left(\mathbf{U}^2 - \mathbf{I}\right) \tag{3.1}$$

Where **U** is the right stretch tensor and **I** the identity tensor. The relationship between axial stretch and various strain definitions, linear and non-linear (Green, Hencky-logarithmic), demonstrated that while the three converge at stretch values close to unity (small strain approximation), there are significant differences when deformations are finite, necessitating non-linear strain measurements (**Figure 3-5**).

While the Green strain tensor is a valid non-linear measure of finite strain, it contains, by definition, an asymptotic limit for compressive strain of -0.5. This conclusion is derived from taking the limit of equation (3.1), as stretch approaches zero. Thus, the positive limit (+∞) and the negative limit of the strain measure used are unequal, and any comparison of positive and negative strain results must consider this asymmetry. For example, under hypothetical axial strain conditions, a 50% compression of tissue stretch (a line segment of unit length contracting to a length of 0.5) would correspond to a strain of -0.375, whereas a 50% expansion of tissue stretch (a line segment of unit length expanding to a length of 1.5) would correspond to a strain of 0.625.

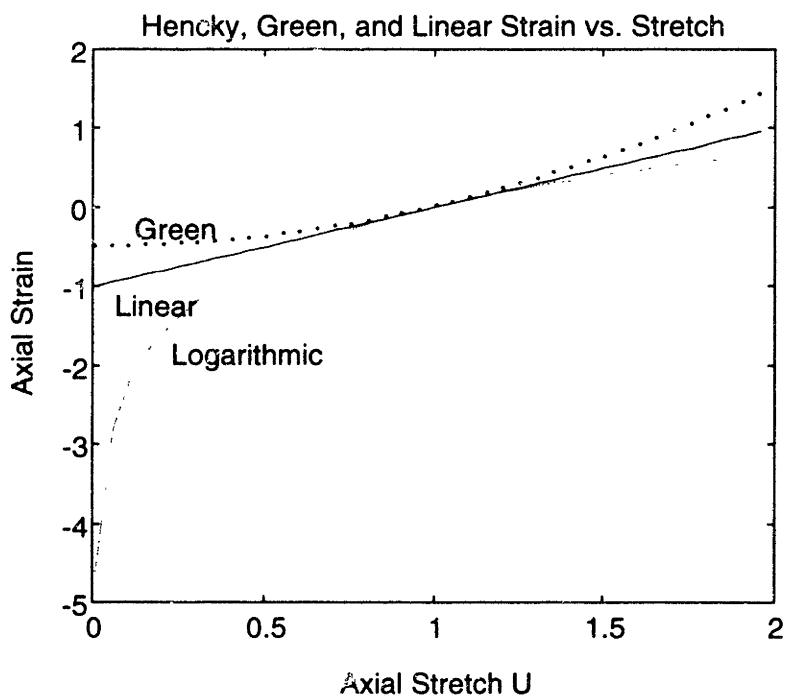

Figure 3-5 A plot of axial strain vs. stretch shows two non-linear strain definitions (Green and Hencky or logarithmic) compared to classic linear strain. Note that Green's strain has a minimum asymptotic limit of -0.5.

In order to resolve the idealized material continuum of the tongue, discrete triangular deforming elements were defined by digitizing nodes at tag line intersections. Thus each triangular element was composed of two independently deforming line elements; one along the x-axis and the other along the y-axis in the rest configuration. Each line element had length s at rest, which was defined by the tag spacing. Axial strains were calculated based on the lengths of the deformed line elements (s_1 and s_2 respectively), while shear strain was calculated based on line element lengths, as well as the relative angle between adjacent line elements (90° - ϕ):

$$E_{xx} = \frac{1}{2}\left(\frac{s_1^2}{s^2} - 1\right) \tag{3.2}$$

$$E_{yy} = \frac{1}{2}\left(\frac{s_2^2}{s^2} - 1\right) \tag{3.3}$$

$$E_{xy} = \frac{s_1 s_2}{2s^2}\sin\phi \tag{3.4}$$

Although this tagging technique is inherently two-dimensional, the out-of-plane axial strain was calculated knowing the 2-D strain condition, assuming that tongue muscle was incompressible[1] (hence isochoric), and that out-of-plane shear strains were negligible:

$$E_{33} = \frac{1}{2}\left(\frac{1}{(1+2E_{11})(1+2E_{22})} - 1\right) \tag{3.5}$$

where E_{11}, E_{22}, and E_{33} are the principal strains. Since shear strains E_{xz} and E_{yz} were assumed nil, $E_{zz} = E_{33}$ regardless of the reference frame, and thus, each finite triangular element in the tagging grid had an associated non-linear (Green's) symmetric strain tensor given by

$$\begin{bmatrix} E_{xx} & E_{xy} & 0 \\ E_{yx} & E_{yy} & 0 \\ 0 & 0 & E_{zz} \end{bmatrix} \tag{3.6}$$

[1] Experiments on frog sartorius muscle have demonstrated that volume decrease during muscular contraction is less than 0.01% (Abbott and Baskin, 1962).

Directional axial or shear strains were represented individually as a color-coded "map" overlaying the original tagged image. This map constituted a pseudo-surface whose height at a given spatial location was defined by the amount of strain at that location, as determined by its proximity to a finite element centr'd. The surface was smoothed by bi-cubic approximating splines.

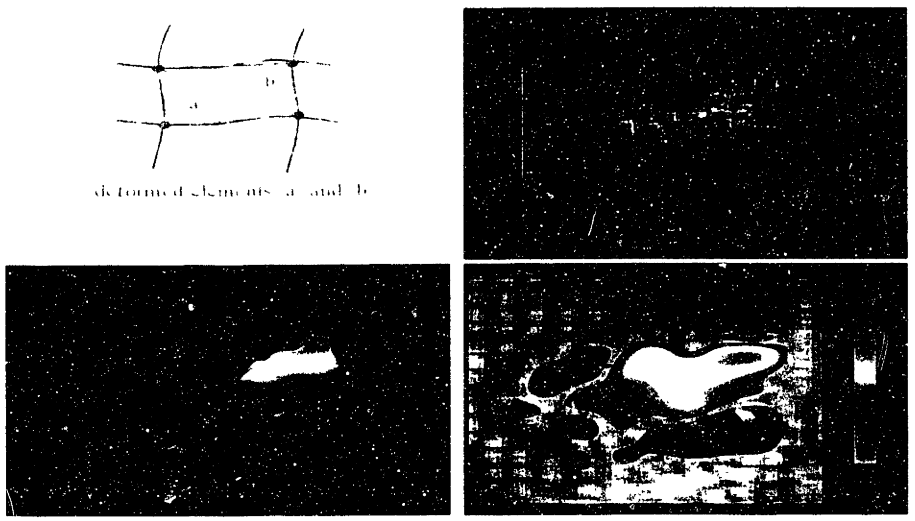

Figure 3-6 Strain mapping was completed using triangular elements. (Upper left) Triangular element mesh defined as nodes located at the tag line intersections, with elements, a and b, shown. (Upper right) Strain represented as a pseudo-surface whose height denotes the amount of strain for each element. (Lower left) Pseudo-surface smoothed by bicubic splines. (Lower right) Transposition allowing strain to be viewed as a color-coded map from above.

The entire strain tensor was alternately represented by a spatial array of octahedra, with each octahedron centered on a tagging element's centroid. The major and minor axes of these octahedra were oriented according to the directions of the eigenvectors, and scaled to the linear directional axial stretch measured in the given tagging element. In addition, the relative size of an octahedron was based on a scaling factor, f, defined by a function of the strain tensor's independent eigenvalues (λ_1, λ_2):

$$f = \sqrt{\lambda_1^2 + \lambda_2^2} \tag{3.7}$$

3.2 An Analysis of Primitive Lingual Deformations

3.2.1 Methodology and Protocol

Subjects (n = 8) were chosen for study who possessed no history or current abnormalities of speech or swallowing. These studies were approved by the Institutional Review Board for Human Research of Beth Israel Deaconess Medical Center. For a given experiment, the protocol was as follows: 1) application of magnetic tags to the resting undeformed tongue muscle tissue, which, through an audible click, prompted the subject to perform the prescribed tongue motion; 2) delay of a set interval (400 – 500 msec) during which time the tissue deformed by voluntary action of the subject; and 3) imaging of the tagged, deformed tissue, held static in the deformed state by the subject.

3.2.2 Results of Analysis

The cardinal tongue motions of anterior protrusion (**Figure 3-7**), sagittal curl to the hard palate (**Figure 3-8**) and lateral tongue curl left (**Figure 3-10**) occurred as the result of coordinated intrinsic muscle contraction. The mechanical consequence of these contractions was depicted as strain tensors for individual elements, and represented as composite strain maps for each motion. Each strain map represented a single component of the strain tensor whose magnitude corresponded to a color-code and was referenced to resting tongue tissue. Negative strain values of -0.5 to 0 were represented as cyan and blue, while positive strain values of 0 to 2.0 were represented as green, yellow, and red.

Anterior protrusion produced positive strain in the anterior portion of the tongue, as evidenced by the strain tensor visualization (**Figure 3-7c**). The positive strain was along the axis of elongation (anterior-posterior, E_{xx}) and peaked at 2.18. This elongation coexisted with bi-directional contraction (negative strain) in the anterior tongue along the superior-inferior (E_{yy}) and medial-lateral (E_{zz}) axes. The contractile strain for the displayed image was calculated to be as low as -0.38 and -0.46 in the y and z directions respectively. The lower portion of the tongue was strain free.

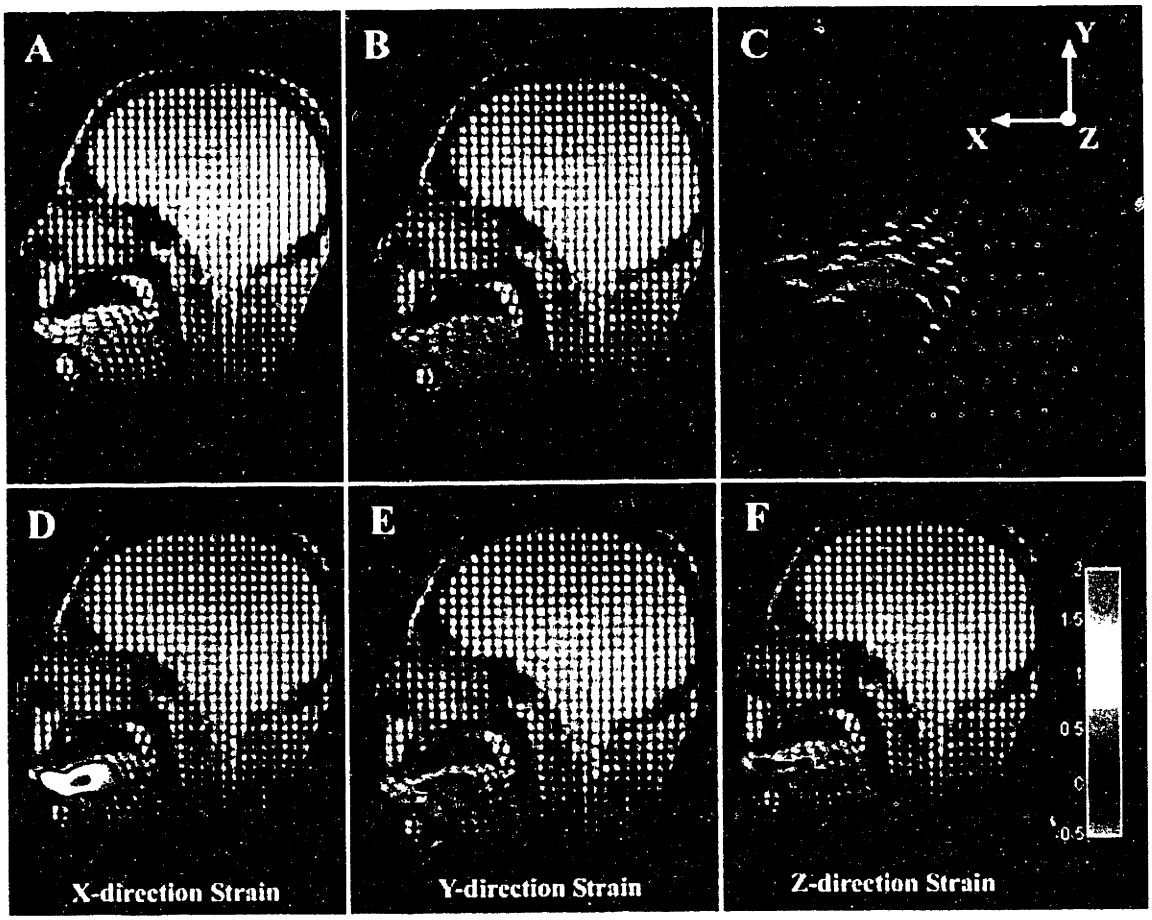

Figure 3-7 A mid-sagittal analysis of the human tongue in anterior protrusion. (A) Deformed grid imaged after tongue protrusion. (B) Triangular finite element mesh associated with this motion. (C) The 3D strain tensor for each element was represented by octahedra and demonstrated that the posterior and inferior regions of the tongue were strain-free. (D), (E), and (F) related the x, y, and z normal strain components of the strain tensor, respectively. These data show that a bidirectional contraction in the y and z directions resulted in tissue protrusion in the x-direction.

In order to study tongue bending, the methodology for deriving strain from a deformed grid image was combined with several statistical analyses. A plot of tissue strain versus distance from the inside edge of the bend was created. The relationship between these two variables was explored with the linear correlation coefficient. A single row of elements along the transverse section at maximum curvature was studied in each tongue. The variables were normalized such that the strain measure was divided by the maximum strain in the given row, and the distance from inside edge was divided by the width of the tongue along the radius of maximum curvature. This normalization allowed for the comparison of data points from tongues of various shapes and sizes, undergoing various degrees of bending.

Sagittal tongue curl to hard palate produced positive anterior-posterior (E_{xx}) strain that peaked at 1.09 and increased with distance outward from the center of curvature (**Figure 3-9**, $r = 0.9216$, $p < 0.0005$). This graded extension was also seen in the strain tensor visualization (**Figure 3-8c**). For the displayed image, the elongation was due to a commensurately graded medial-lateral (E_{zz}) contraction that was as low as -0.45. Superior-inferior (E_{yy}) strain was mainly positive, peaking at 0.42. The lower portion of the tongue was strain free.

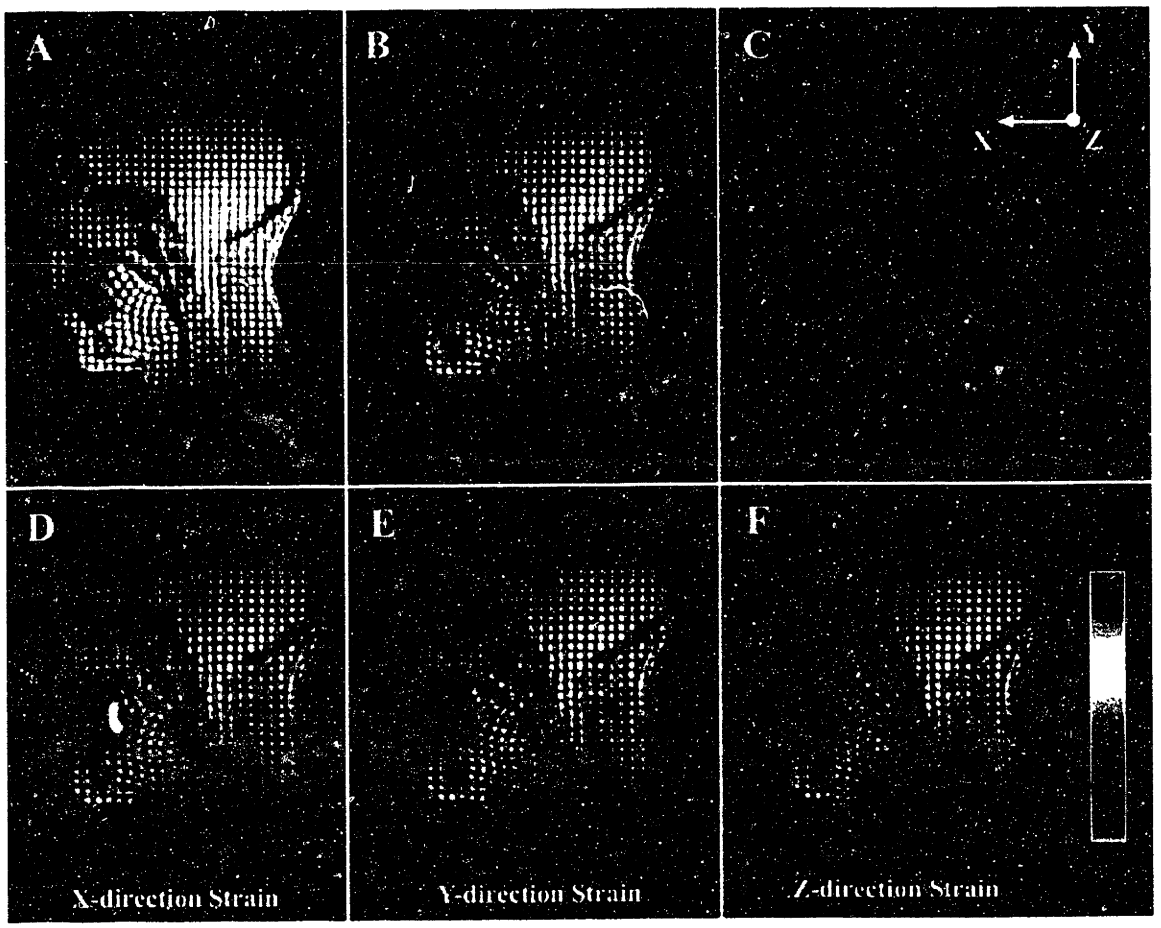

Figure 3-8 A mid-sagittal analysis of the human tongue in sagittal bending to the hard palate. (A) Deformed grid imaged after tongue bending. (B) Triangular finite element mesh associated with this motion. Each element's entire 3D strain tensor was represented in (C) and exhibited the posterior and inferior regions of the tongue to be strain free. (D), (E), and (F) relate the x, y, and z normal strain components of the strain tensor respectively. X-direction and z-direction strain increased and decreased radially from the center of curvature, respectively.

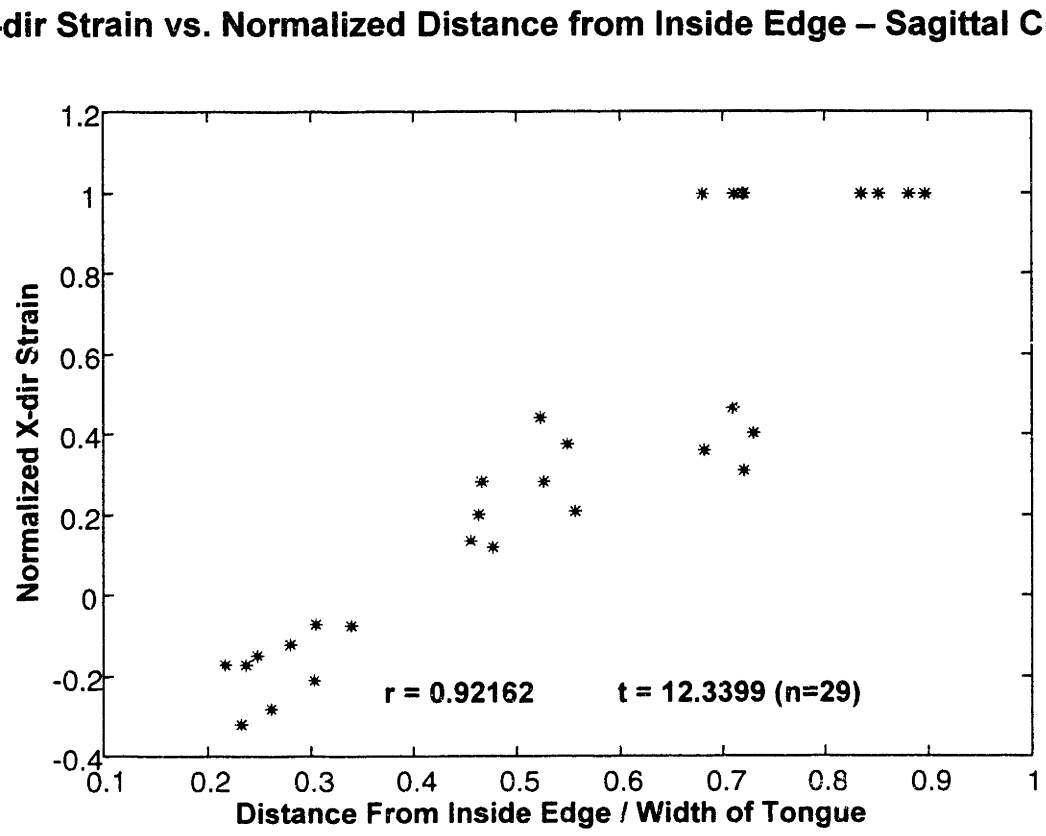

Figure 3-9 Anterior-posterior (x-direction) normal strain as a function of distance from the tongue bend's inside edge for sagittal tongue bending. Strain was normalized by the maximum value of strain in the analyzed cross-section, while distance from the inside edge was normalized by the width of the tongue at the relevant cross-section. A-P strain increased with distance from the inside edge (r=0.92). The negative strain values at the tongue inside edge suggested a uniaxial contraction of the longitudinal sheath fibers. These data represent 8 images (5 subjects); normalization was completed to allow for cross-comparison. The t-value tests whether the r-coefficient is significant for the sample size.

Lateral tongue curl left was fundamentally similar to sagittal tongue curl. Anterior-posterior (E_{yy}) strain was predominantly positive, peaked at 0.99 and increased with distance outward from the center of curvature (**Figure 3-11**, $r = 0.8978$, $p < 0.0005$). This graded extension was also evidenced by the strain tensor visualization (**Figure 3-10c**). For the image displayed, the elongation coexisted with a contraction in the superior-inferior (E_{zz}) direction whose lower bound was -0.35 and which decreased with distance from the center of curvature. The posterior of the tongue was under positive medial-lateral (E_{xx}) strain peaking at 0.83.

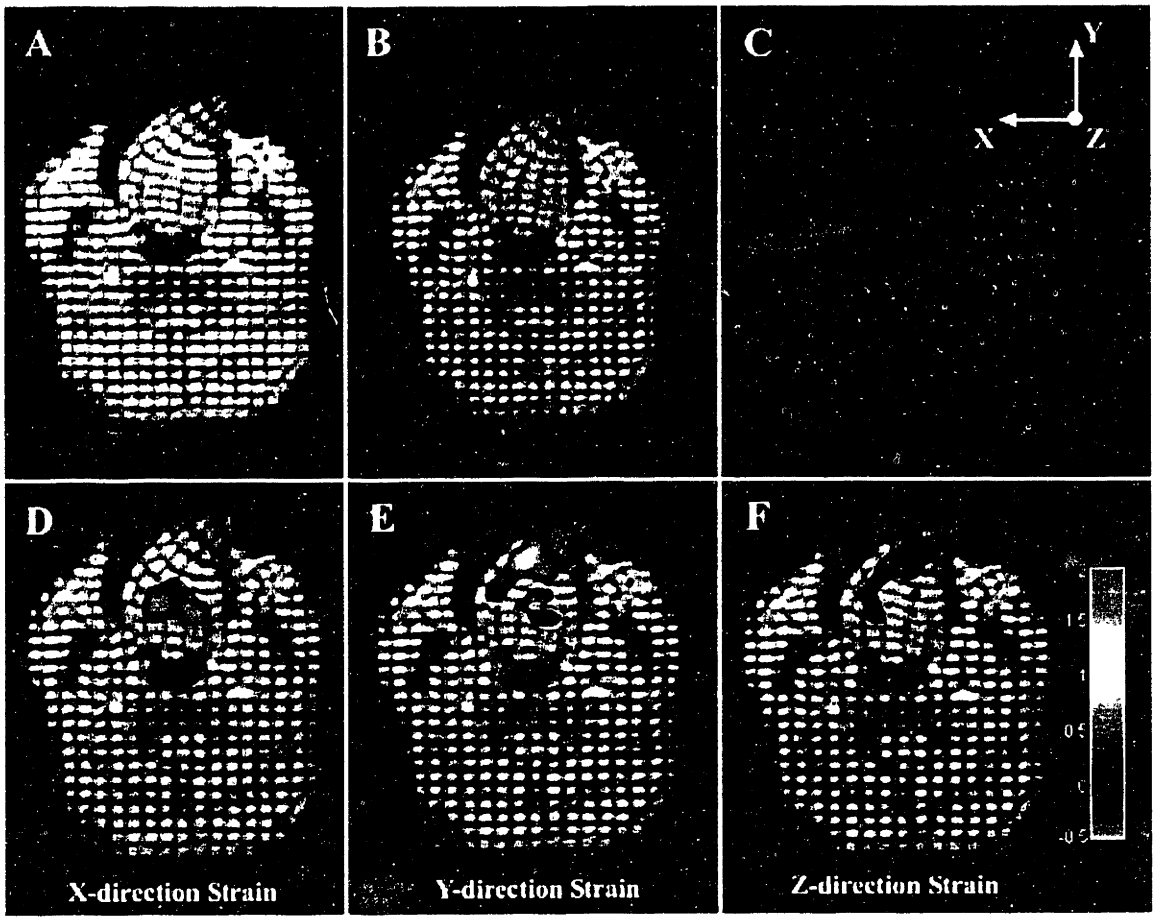

Figure 3-10 An analysis of the human tongue in lateral bending. (A) Axial slice of the deformed grid imaged after tongue bending. (B) Triangular finite element mesh associated with this motion. Each element's entire 3D strain tensor was represented in (C) - (D). (E), and (F) relate the x, y, and z normal strain components of the strain tensor respectively. Y-direction and z-direction strain increased and decreased radially from the center of curvature, respectively.

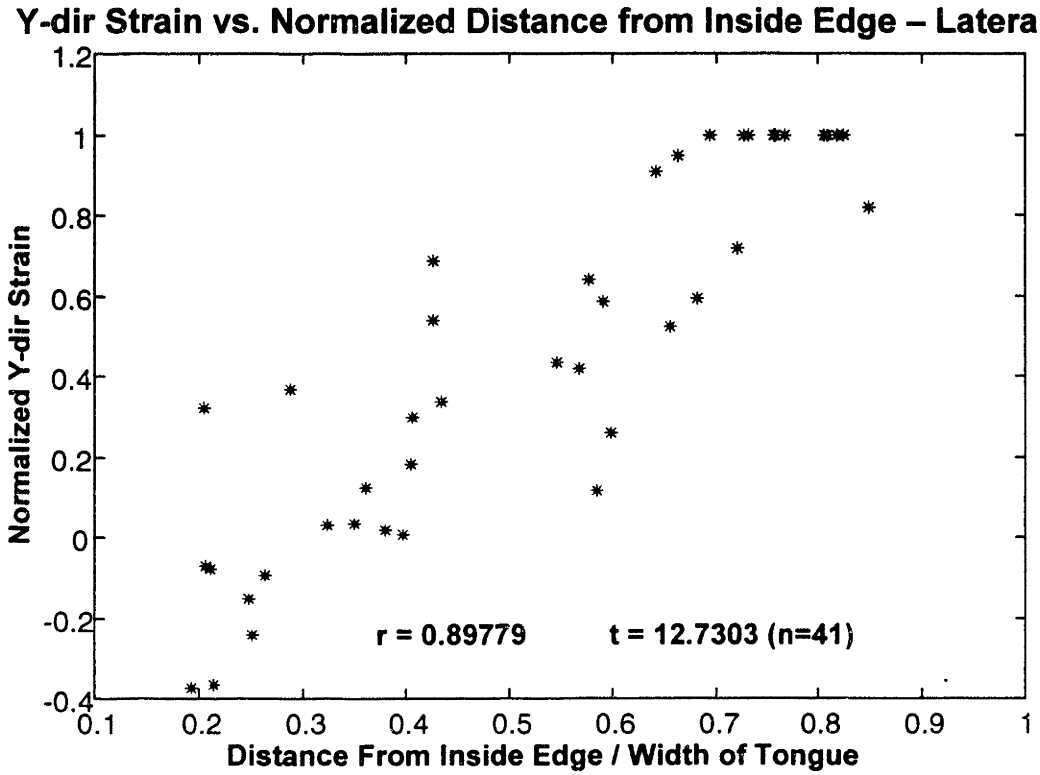

Figure 3-11 Anterior-posterior (y-direction) normal strain as a function of distance from the tongue bend's inside edge in lateral tongue bending. Strain was normalized by the maximum value of strain in the analyzed cross-section, while distance from the inside edge was normalized by the width of the tongue at the relevant cross-section. A-P strain increased with distance from the inside edge (r=0.827). The negative strain values at the tongue inside edge suggested a uniaxial contraction of the longitudinal sheath fibers. These data represent 9 images (3 subjects); normalization was completed to allow for cross-comparison. The t-value tests whether an r-coefficient is significant for the sample size.

3.2.3 Discussion: Tongue Protrusion and Bending

Tagging MRI was utilized to investigate the *in vivo* muscular strain in the human tongue. The analysis provided a biomechanical basis for understanding the effect of local muscular activity on the physiological function of the tongue, and proposed a general model relating local contraction and tissue deformation in muscular hydrostats.

The results demonstrated the manner in which regional activation of the intrinsic musculature results in protrusive and bending motions. In anterior tongue protrusion, bi-directional contraction of mutually orthogonal intrinsic muscle fibers residing in the core of the tongue resulted in protrusion along the tongue's longitudinal axis. This result was consistent with the tongue's role as a muscular hydrostat adhering to the isochoric condition (incompressibility), which specified that original volume was maintained throughout deformation. In fact, the mechanical advantage of lingual myoarchitecture

can be illustrated by assuming the tongue to be a right circular cylinder, with volume $\pi r^2 L$. If tissue incompressibility is assumed for the cylinder, an inverse square relationship between cross-sectional radius and tongue length is evident. Hence, small changes in tongue cross-section are amplified into large changes in tongue length. Specifically, contraction in the tongue core occurred in the superior-inferior and medial-lateral directions, consistent anatomically with the region's fiber orientation. This assumed that the x-y-z coordinate system of the image coincided with the anterior-superior-lateral coordinate system of the tongue, which was deemed reasonable from tagged images of the undeformed tissue. For this simple prototypical motion, negative strain presented in these directions was considered synonymous with muscle contraction because overlapping extrinsic muscle attachments lateral or superior to the regions in question were nonexistent. Such attachments could conceivably introduce compressive strain to uncontracted muscle tissue by deforming adjacent muscle fibers in the organ.

Anterior-posterior positive strain peaking at 218% was typical for the group studied and exemplified the notable expansive ability of the tongue tissue. While this value seems notably high compared to strain data collected from other animals, it may not be completely incongruous (**Table 3-1**). Smith used a cineradiographic technique with implanted lead marker beads (injected solder) to estimate lingual strain during physiological protrusion (Smith, 1984; Kier and Smith, 1985). The published data showed strains as high as 106% in *Tupinambis nigropunctatus* (tegu lizard). This value was derived using implanted lead markers (one in the posterior tongue and one in the anterior) and, hence, represents an averaged strain for the whole tongue. Our maximum strain value of 218% was a localized value based on a 7mm resting tag separation. Furthermore, Kier and Smith expressed their data with linear strain, i.e. $\Delta L/L_o$ or U-1 (in terms of stretch). If our high axial strain value (which was expressed as Green's strain, $\frac{1}{2}(U^2-1)$) were converted to linear strain for the sake of comparison, it would be 131%; close to the expansion range reported by Smith, 1984 – 90% to 120%. However, the appropriate comparison would be to calculate the linear strain from overall tongue length during protrusion and rest. This value was found to be 42%. Thus, while regions within the tongue are highly extensible in protrusion (up to 218%), the tongue as a whole protrudes only 42% of its resting length. Interestingly, Doran (1971) hypothesized that mammalian tongues could be subdivided into two groups: intra-oral and extra-oral (Doran and Baggett, 1971). The former use their tongues mainly within their oral cavities (for deglutition, mastication etc.), and hence extensibility from rest is less than 50%. The latter group also uses their tongues in food gathering and hence extensibility is greater than 100%. Intra-oral mammalia include Rodentia, Carnivora, and Primates; while extra-oral mammalia include Monotremata (*Tachyglossus*, an echidna), Marsupiala (*Tarsipes*, honey possum), and Pholidota (*Manis*, anteater). Other notable differences between our experiments and those of Smith *et al.* concerned the

fact that our methodology elicited protrusive efforts approaching maximal, whereas the Smith animal experiments elicited a more physiological effort with multiple protrusion cycles (lapping of water). Also, the injection of lead marker beads (and concurrently placed electromyography electrodes) may have artificially constrained the extensile capabilities of the tissue, thereby limiting the protrusive capabilities of the animals. With these caveats in mind, there still exists a basis for comparison in cross-species tongue protrusion.

Species	**N** (number of cycles)	**Expansion** (linear strain)
Tupinambis nigropunctatus (tegu lizard)	8	106%
Varanus exanthematicus (monitor lizard)	5	70%
Dasypus novemcinctus (nine-banded armadillo)	6	97%
Didelphis virginianus (opossum)	3	72%
Homo sapiens (human)	1	42%

Table 3-1 Axial strain observed in human lingual protrusion compared well with that observed in animal experiments. Animal data were derived from cineradiographic tracking of implanted lead marker beads and reflected physiological protrusion (water lapping) averaged over multiple cycles, N. Elongation was published as linear axial strain for the animal experiments. For comparison purposes, our data was converted to this strain definition.

The principal axis of tissue expansion was confirmed by visualization of the strain tensors (**Figure 3-7c**), which demonstrated that the major axis of octahedra in the anterior tongue coincided with the longitudinal axis of the organ; as would be expected for tongue protrusion. Furthermore, the absence of significant strain in the posterior and inferior portions of the organ refuted the hypothesis that the genioglossus muscle could be solely responsible for anterior protrusion (Bennett and Hutchinson, 1946; Abd-El-Malek, 1955; Scardella, Krawciw et al., 1993). If a portion of the genioglossus was active in the observed anterior protrusion, it would be only those extensions of the genioslossus' anterior most fibers which merge with the verticalis fibers (Takemoto, 2001). However, it is conceivable that in a maximum volitional effort, the genioglossus could augment protrusion by pulling the tongue base forward in the oral cavity (Bennett and Hutchinson, 1946). Interestingly, the region of positive superior-inferior strain (peaking at 0.472) observed in **Figure 3-7e** was due to the tongue body stretching slightly superior in order to extrude out from the oral opening.

While anterior protrusion could be attributed almost exclusively to the contraction of the transversus and verticalis muscles, retraction of the tongue is most likely not a simple consequence of the relaxation of said muscles. One hypothesis is that the superior and inferior longitudinalis muscles are the primary tongue retractors. While these muscle layers are too thin to be imaged adequately with Tagging MRI, this hypothesis has been put forth by previous investigators as well (Kier and Smith, 1985). As early as 1950, Chapman conceived that protrusion and retraction in worms[1] is accounted for by an antagonistic relationship between a muscle layer perpendicular to the long axis (circumferential) versus one that is parallel to the long axis (longitudinal) (Chapman, 1950). A similar relationship exists for the muscular hydrostat examined in this thesis. Protrusion produced by muscles perpendicular to the long axis (transversus and verticalis) was most likely counteracted by retraction produced by muscles parallel to the long axis (superior and inferior longitudinalis). The idea that retraction is enacted by an elastic recoil of collagen fibers crumpled during the transversus/verticalis contraction (as well as the recoil of longitudinal fibers extended in protrusion) cannot be discounted, but is most likely not the principle retraction method due to the lengthy time scale of such a process. Other theories posit that, at least in mammalian tongues, extrinsic muscles such as the styloglossus and hyoglossus also play a prominent role in tongue retraction (Bennett and Hutchinson, 1946).

Bending of the tongue, either upward or lateral, was caused by unilateral contraction of the longitudinal sheath combined with regional contraction of the core fibers. Contraction of the longitudinal muscle fibers on the side of the tongue closest to the center of curvature was demonstrated by the existence of negative strain values at the inside edge (**Figure 3-9**, and **Figure 3-11**). These results thus supported the prediction made by Smith and Kier (1989), who proposed that unilateral contraction of the peripherally located and longitudinally oriented sheath was a mechanism for bending in a muscular hydrostat. It must also be noted that ipsilateral styloglossus muscle contraction may also have played a role in lateral tongue bending, as the fibers of this extrinsic muscle have been found to extend to the tip on the lateral portion of the tongue, merging with longitudinal sheath fibers (Takemoto, 2001). The data additionally demonstrated a synergistic mechanism for tissue bending through graded core fiber contraction as a function of radial distance from the center of curvature. For sagittal bending, some subjects exhibited graded contraction as a summed response of medial-lateral *and* superior-inferior fibers. This graded contraction resulted in a commensurate expansion in the antero-posterior direction that increased with distance from the center of curvature, thereby efficiently supplementing the contraction of the longitudinal sheath in the production of bending. The positive

[1] Worms, as well as polyps and other invertebrate animals, are classical hydrostats in that muscle and connective tissue surround a fluid filled (incompressible) cavity.

relationship between antero-posterior strain and distance from center of curvature appeared linear, thus justifying the use of a linear correlation coefficient. Similar to tongue protrusion, the region of positive superior-inferior strain seen in the sagittal bending image resulted from the tongue body being stretched superiorly toward the hard palate. Furthermore, the inactivity observed in the posterior and inferior portions of the tongue supports the absence of genioglossus contraction in sagittal tongue bending. While neither tongue bending nor tongue protrusion manifested a significant contribution of the genioglossus muscle, this does not exclude a role for this muscle in more complex motor tasks, such as human speech or swallowing, in which the physiological demands for tissue versatility are greater. The absence of strain in the posterior portion of the tongue suggested that the styloglossus and hyoglossus muscles were also inactive during protrusion and bending. Since these muscles insert into the lateral aspects of the tongue body (and hence were not directly imaged in this study), the contraction of these muscles should manifest strain in the mid-sagittal slice by passive drag. Thus, the overall absence of strain in the posterior tongue, as was calculated by the analysis, lead to the conclusion that the extrinsic musculature was inactive for the motions studied.

Lingual contraction during bending resulted both in deformation and the skeletal support for that deformation. Hypothetically, if tongue bending were associated only with unilateral contraction of the longitudinal sheath (e.g. superior longitudinalis only), the tissue response would be longitudinal shortening. This behavior has been depicted in the form of idealized beams (**Figure 3-12**).

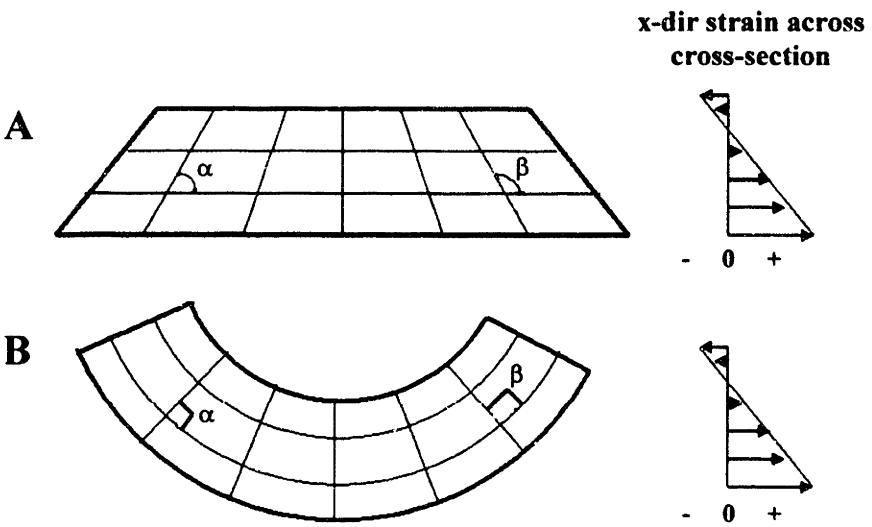

Figure 3-12 Idealized beams with equivalent x-direction strain patterns. One beam is deformed by normal and shear strains (A), while the other is deformed by pure bending (B). Distortion of the rectilinear grid under shear in A has resulted in the previously right angles α and β to become acute and obtuse, respectively. Pure bending in beam B has resulted in a deformed radially symmetric grid that has maintained α and β at 90°. The shear strain state seen in tongue bending was a combination of these two idealized conditions.

While both deformed contours exhibit the same x-direction normal strain across their cross-sections, beam A does not resist shear since angles α and β deviate from the undeformed value of 90° (**Figure 3-12a**). Hence, the left portion of the beam is subjected to positive (clockwise) shear, while the right is subjected to negative (counter-clockwise) shear. On the other hand, beam B is completely devoid of shear strain since α and β remain right angles, thus defining pure bending (**Figure 3-12b**). Another way to describe this behavior would be to state that for pure bending tongue cross section must remain unchanged. For beam A above, the 2D cross-section increases by $1/\sin(\alpha)$; while for beam B, the cross-section remains unchanged.

The data indicated that sagittal tongue bending was a compromise between these two idealizations. Pure tongue bending was superimposed upon the shear deformation exhibited by the right portion of beam A. The existence of negative shear (**Figure 3-13**) resulted from the inferior constraint imposed by the uncontracted genioglossus muscle. Due to the close anatomical relationship between the intrinsic and extrinsic muscle groups, shear strain is necessarily introduced when tissue expansion (as seen in the intrinsic core fibers) occurs adjacent to an uncontracted muscle (such as the genioglossus fibers inferior to the intrinsic core). Furthermore, the amount of shear strain produced when the intrinsic musculature contracts to impose x-direction normal strain will depend on the shear modulus (modulus of rigidity) of the tissue. The greater the shear modulus, G, the lower will be the shear strain. In order to resist shear during bending and maintain a constant cross-section throughout deformation, the core fibers must contract. This contraction increases the tissue's shear modulus by increasing muscle tone, thereby simulating skeletal support. Sagittal tongue bending was further developed by a modeling study, presented in Chapter 4.

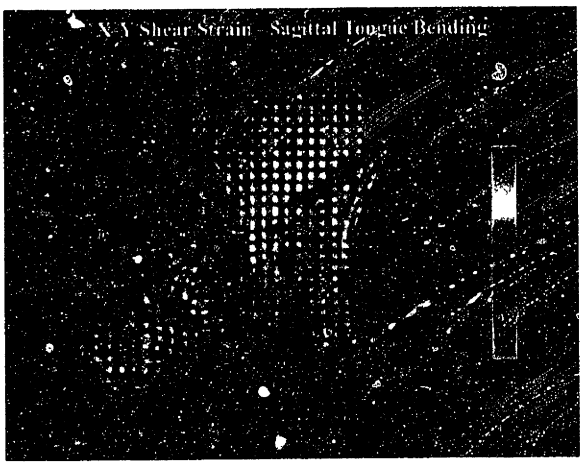

Figure 3-13 Raw element x-y non-linear shear strain map for sagittal tongue bending. The magnitude of shear strain was color-coded with cyan, blue, and purple corresponding to negative shear (-0.4 to 0), and green, yellow, and red corresponding to positive shear (0 to 0.4) The tissue was predominantly under negative (counter-clockwise) shear strain presumably due to the inferior constraint imposed by the uncontracted genioglossus muscle.

In order to extend the two-dimensional strain analysis of single shot tagging MRI, it was assumed that the tongue muscle tissue was incompressible, and hence isochoric. Mathematically, this means that the determinant of the deformation gradient tensor is equal to unity. This one equation can be solved for its one unknown (E_{zz}, through-plane axial strain) if it is assumed that the through-plane shear strains, E_{xz} and E_{yz}, are negligible. For tongue motions that are symmetric with respect to the imaging plane, this assumption was likely to be valid; however, tongue motions asymmetric to the imaging plane would likely introduce through-plane shears, which cannot be measured, and may therefore invalidate this assumption. These issues were explored more formally in **Appendix E**.

Furthermore, this methodology was inherently dependent upon the presence of adequate tag contrast. Tag fading, i.e. loss of contrast between tagged and untagged tissue, can result from one of several causes, namely T_1 decay of the tagged tissue's longitudinal magnetization, motion artifact, and through-plane motion. T_1 decay is an intrinsic tissue property, and therefore serves to limit the TI time between tagging and imaging. Blurring of the tags may also result if physiological tissue motion is substantial during the imaging time, whether this motion is within the imaging slice or "through-plane." Blurring or fading of the tags decreases the contrast between tagged and untagged tissue, potentially making the grid unrecoverable. Thus, minimizing imaging time is important for mitigating motion artifact.

3.3 *A Further Exploration of Lingual Protrusion Patterns*

In order to test the physiological versatility of the anterior tongue's intrinsic fibers, a more exploratory study of tongue protrusion was completed using tagging MRI. The anterior human tongue is comprised of regions of heterogeneously aligned intrinsic muscle fibers (transversus and verticalis muscles), which have already been proven to be particularly important for producing anterior protrusion as well as providing mechanical stiffness for an extensive array of lingual deformations (Napadow, Chen et al., 1999). In providing for this capability, we hypothesized that the core fibers may function either as uni-directional or as bi-directional actuators, depending on the recruitment of different motor units.

This hypothesis of variable activation was rooted in the innervation and composition of lingual myoarchitecture. For instance, in a recent study of nerve-muscle relationships in the canine tongue, Mu and Sanders suggested that considerably more complexity may exist at the nerve-muscle interface. In particular, based on their analysis, the orthogonally oriented muscle sheets of the core intrinsic muscles (transversus and verticalis muscles) appeared to be individually innervated by separate branches of the trigeminal (sensory) and hypoglossal (motor) nerves. Moreover, there were many examples of cross innervation involving the major branches of XII, IX, and V projecting to the discrete fibers innervating the serial intrinsic muscle sheets. Thus, highly variable temporal and spatial patterns of activation could exist on both the sensory and motor sides, resulting in multiple conceivable patterns of fiber recruitment within the musculature of the tongue. Furthermore, it is known that individual motoneurons innervate muscle fibers of a single histochemical fiber type (Burke, 1981). Thus, the variability of fiber type seen in the same anatomical muscle population suggests a potential for segmental activation, wherein intrinsic muscles may be subdivided into independently controllable neuromuscular compartments (English and Letbetter, 1982; Depaul and Abbs, 1996). In other words, transversus and verticalis fiber bundles (as described in Chapter 2) may be differentially innervated, allowing for the fine control necessary in deformations involved in speech and mastication.

3.3.1 Methodology

Subjects were chosen to attempt the anterior protrusion maneuver using various combinations of transversus and verticalis muscle recruitment. Some training of the subjects before imaging was required and several subjects were not capable of performing the maneuver. Subjects were imaged with

a Siemens Vision 1.5T MRI scanner using an ultrafast gradient echo tagging pulse sequence (TR/TE 2.3/0.8 msec, slice thickness 10 mm, and effective spatial resolution 1.3 x 1.3 mm). Tissue strain was quantified from discrete deforming elements. These triangular elements were defined by tag intersections from MR images of the protruded tongue. Tissue strain was depicted graphically as color-coded 2D strain maps and in tensorial form as octahedra whose axes corresponded to the 3D strain properties for each element. This methodology was similar to that employed for the other tagging MRI studies described in this chapter.

3.3.2 Results of Heterogeneous Protrusion Study

Anterior protrusion could be elicited by contraction of either the transversus muscle, the verticalis muscle, or by both of these intrinsic muscles simultaneously. The unidirectional contractions produced two distinctly different anterior protrusions (**Figure 3-14**). In protrusions dominated by verticalis muscle contraction, the tongue appeared flattened in the axial plane. This profile was termed "Flat Tongue" and was in contrast to transversus dominated protrusion, which produced a more rounded tongue cross-section and was termed "Fat Tongue."

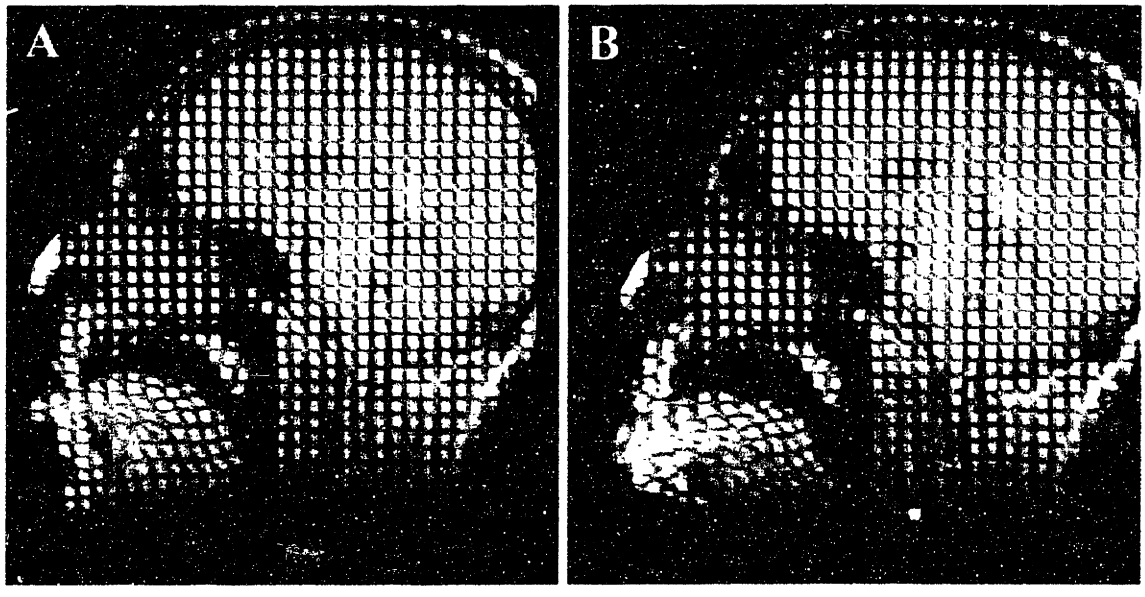

Figure 3-14 Tagged mid-sagittal images of tongue protrusions resulting from contraction of different intrinsic muscle groups. (A) Verticalis dominated anterior tongue protrusion was flattened in the axial plane, and was termed "Flat Tongue." (B) In contrast, transversus dominated tongue protrusion was rounded in cross-section and was termed "Fat Tongue." These characteristic differences could be easily appreciated by gross imaging alone.

Transversus dominated protrusion (anterior protrusion dominated by transversus muscle contraction) produced medial-lateral contractile strain (z-direction strain) peaking at -0.35 (**Figure 3-15**). Tissue incompressibility produced positive strain (expansion) in the x-direction and y-direction. Strain in the posterior tongue suggested some extrinsic genioglossus m. contribution to the protrusion. Verticalis protrusion (anterior protrusion dominated by verticalis muscle contraction) produced superior-inferior (y-direction) contractile strain peaking at -0.30 (**Figure 3-16**). Tissue incompressibility produced positive strain (expansion) in the x-direction and z-direction. Strain in the posterior tongue again suggested some extrinsic genioglossus muscle contribution to the protrusion. Combined protrusion (both transversus and verticalis) was discussed previously (**Figure 3-7**) and produced contractile strain along both medial-lateral and superior-inferior directions, peaking at levels similar to uni-directional contractile protrusion.

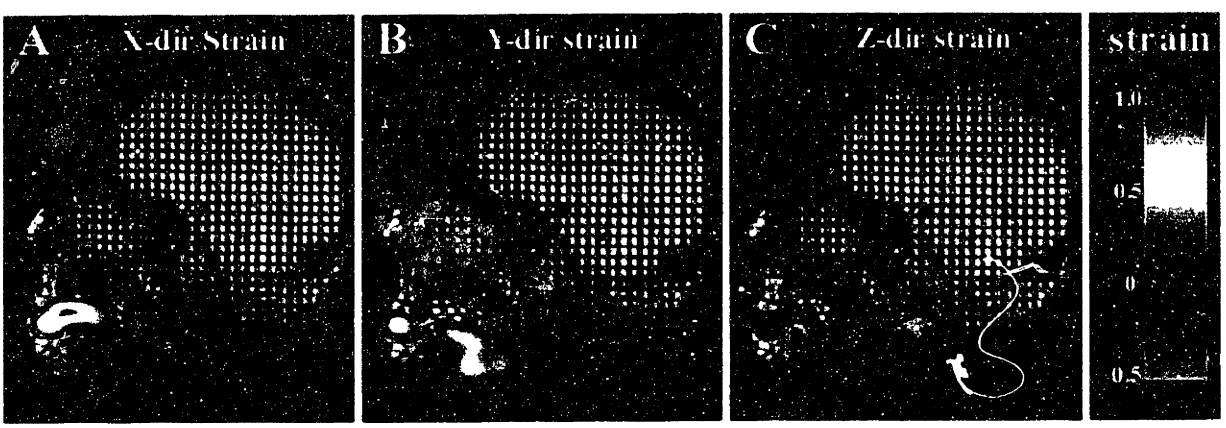

Figure 3-15 Transversus dominated protrusion (anterior protrusion dominated by transversus muscle contraction) produced medial-lateral (z-direction) contractile strain - corresponding to the orientation of the transversus musculature.

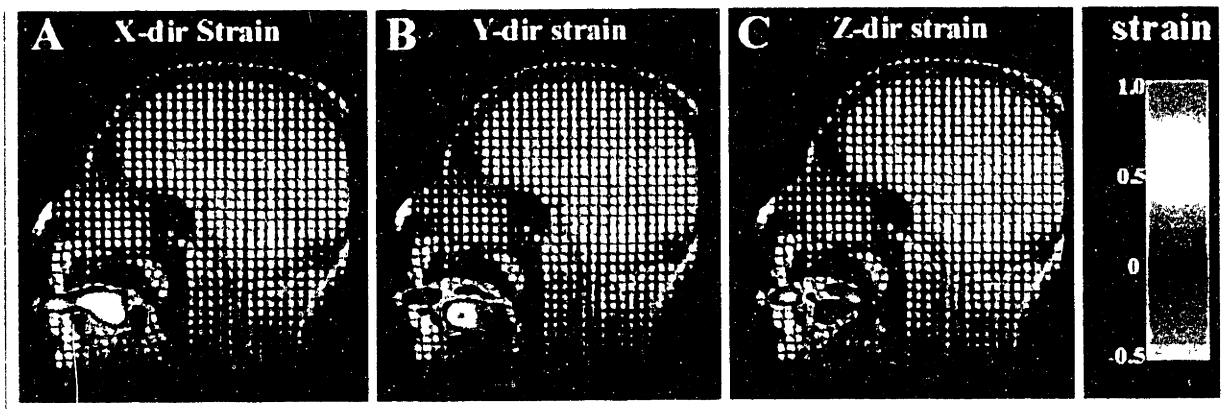

Figure 3-16 Verticalis dominated protrusion (anterior protrusion dominated by verticalis muscle contraction) produced superior-inferior (y-direction) contractile strain corresponding to the orientation of the verticalis musculature.

These data demonstrate that anterior tongue protrusion can be accomplished by at least three different mechanisms: contraction of the verticalis muscle, contraction of the transversus muscle, or the simultaneous contraction of both of these muscle groups. All three mechanism were presented in one figure which plotted verticalis (superior-inferior) and transversus (medial-lateral) strain for each contraction scenario (**Figure 3-17**). The existence of distinct verticalis- or transversus-dominated contraction suggests that myoarchitecture specific motor units differentially innervate these intrinsic muscle groups.

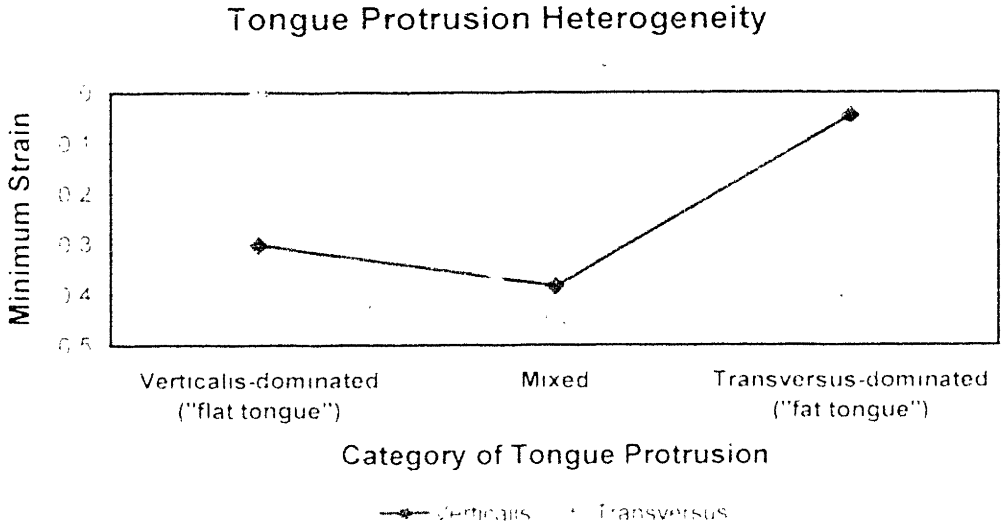

Figure 3-17 This figure demonstrates the spectrum of transversus and verticalis contraction during anterior protrusion. Anterior tongue protrusion can be accomplished by at least three different mechanisms: contraction of the verticalis muscle, contraction of the transversus muscle, or the simultaneous contraction of both of these muscle groups.

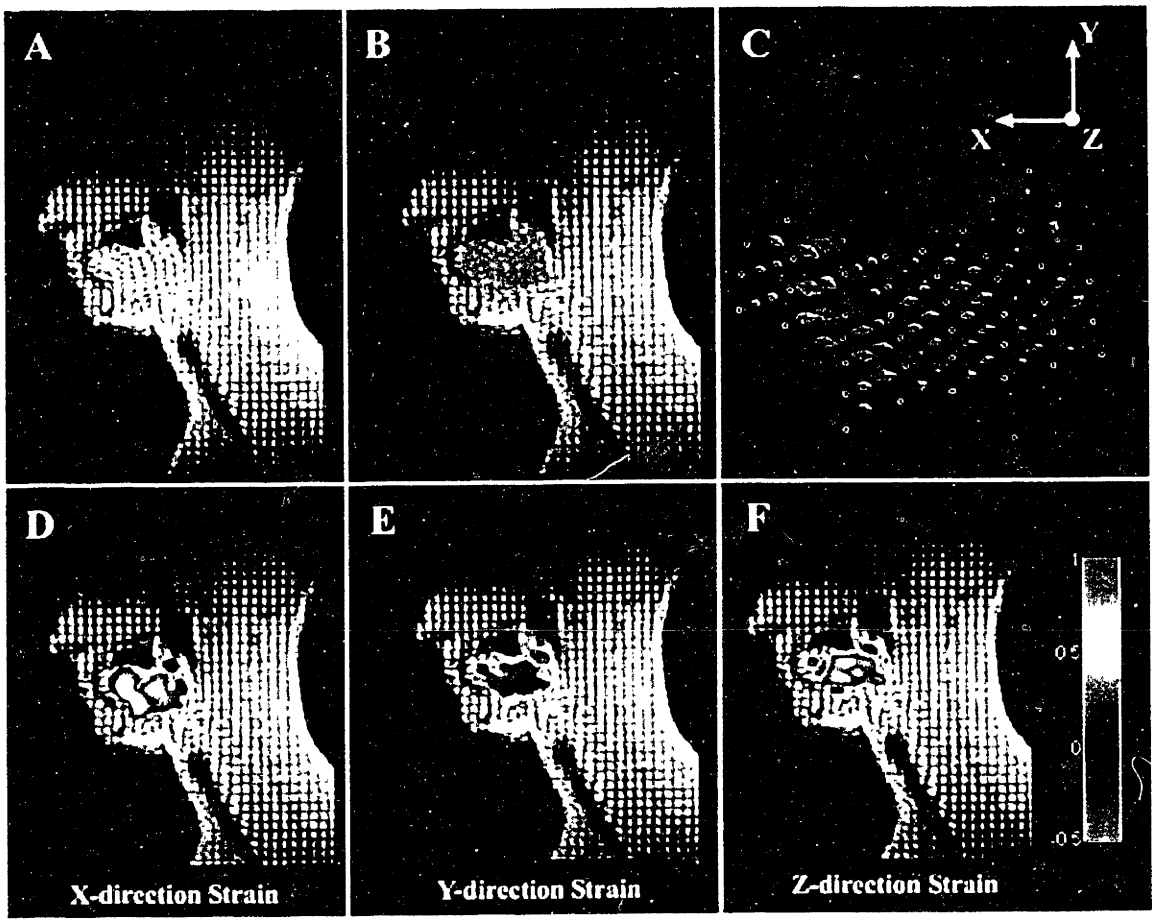

Figure 3-19 Lingual strains during early accommodation were visualized with color coded strain maps and octahedra. (A) Deformed grid associated with tongue movement. (B) Triangular finite element mesh associated with tongue movement. (C) 3D strain tensor depicted as octahedra corresponding to each element. (D-F) 2D strain maps depicting axial strain in the x (D), y (E), and z (F) directions. Bolus containment is associated with negative y direction strain consistent with a synergistic contraction of the anterior genioglossus and hyoglossus, with concomitant x and z direction expansion.

During late accommodation (**Figure 3-20**), with the subject holding the bolus in a posterior depression, the anterior tongue displayed positive y-direction strain (peak strain 0.151). The posterior tongue displayed significant negative y-direction strain (peak strain -0.302) with commensurate expansion along the x and z direction (peaking at 0.358 and 1.845 respectively). Inter-subject mean data also corroborated these deformation patterns ($p < 0.01$) (**Table 3-2**). Thus, bolus accommodation (early and late) principally represents a combination of contraction of the intrinsic core muscles in the anterior tongue (with commensurate anterior or superior expansion), and inferiorly-directed contraction of the extrinsic muscles (genioglossus and hyoglossus) in the middle and posterior regions of the tongue.

3.4 An Analysis of Deglutition

3.4.1 Methodology and Protocol

Subjects (n = 8) were chosen who possessed no history or current abnormalities of speech or swallowing. These studies were approved by the Institutional Review Board for Human Research of Beth Israel Deaconess Medical Center. Dry (saliva only) swallows were elicited from the subjects, and magnetic resonance imaging was performed for each swallow. The timing of image acquisition was determined in order to visualize the various phases of oral stage deglutition. For a given subject, the experimental protocol was as follows:

- application of magnetic tags to the resting undeformed tongue muscle tissue, which through an audible click, prompted the subject to swallow
- imposition of a variable delay time interval, TI (300 – 800 msec, incremented by 100msec), to cover the different phases of the swallow (oral stage)
- imaging of the tagged, deformed tissue.

Inter-subject variation during swallowing was accounted for by a statistical treatment of the strain data. In order to obtain mean directional strain data, four regions in the mid-sagittal slice of the tongue (anterior, mid-superior, posterior, and inferior – **Figure 3-18**) were sampled in the x, y, and z directions. Data were analyzed for each region for three phases of oral stage deglutition: early accommodation, late accommodation, and propulsion. P-values were computed for a one-sided t-test, which tested whether or not a sample mean was significantly greater than or less than zero. The means and standard errors for the one-sided t-test were computed for each condition.

Based on previous determinations of tissue myoarchitecture and function in the mid-sagittal plane, the anterior tongue region (region 1) encompassed the tongue's intrinsic musculature (transversus, verticalis, and longitudinalis muscles). The middle superior tongue region (region 2) encompassed the anterior fibers of the genioglossus muscle and a portion of the intrinsic muscles. The posterior tongue region (region 3) encompassed predominantly the posterior fibers of the genioglossus muscle. While regions 2 and 3 subdivide the genioglossus muscle, there is precedent for heterogeneous, localized activity in this muscle, as has been previously suggested by EMG studies (Miyawaki, Hirose et al., 1975). The inferior tongue region (region 4) encompasses the inferior fibers of the genioglossus muscle, as well as the geniohyoid muscle. The coordinate axes x, y, and z

correspond to anterior-posterior (x-direction), inferior-superior (y-direction), and medial-lateral (z-direction) directions.

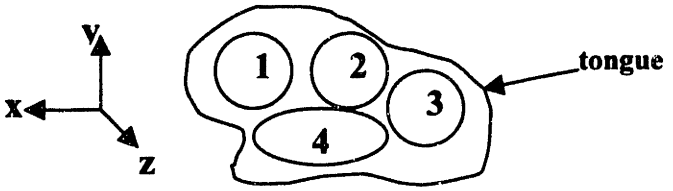

Figure 3-18 Regional analysis of tongue mechanics was performed by the segmentation of the mid-sagittal imaging slice into four functional regions. Region 1: intrinsic musculature, including transversus, verticalis, and longitudinalis. Region 2: anterior genioglossus and posterior intrinsic fibers. Region 3: posterior fibers of the genioglossus muscle. Region 4: inferior genioglossus and geniohyoid fibers. The coordinate axes x, y, and z correspond to anterior-posterior (x-direction), inferior-superior (y-direction), and medial-lateral (z-direction) directions.

3.4.2 Results of Analysis

Direction-dependent strain fields were acquired for the mid-sagittal slice of the tongue using a tissue tagging nuclear magnetic resonance technique. Normal subjects were studied during three phases of dry swallows: early accommodation, late accommodation, and propulsion. Strain data were visualized either as two-dimensional strain maps (axial strain in the x, y, and z directions) for representative subjects, or as octahedra representing the complete strain tensor (directional strain in principal directions) for each deforming element. In addition, inter-subject axial strain means for each of four functional regions of the tongue were also displayed (**Table 3-2**).

In early accommodation, the subject contained the bolus in the middle portion of the tongue's dorsal surface (**Figure 3-19**). The anterior tongue showed a characteristic pattern of positive (expansive) x-direction strain (peak strain 0.521), while the middle tongue showed negative (contractile) y-direction strain (peak strain -0.319), along with positive x and z direction strain (peak strain 0.477 and 0.803, respectively). The posterior and inferior regions of the tongue demonstrated x direction expansion (peaking at 0.208 and 0.477, respectively). Inter-subject mean data corroborated these deformation patterns ($p<0.01$) (**Table 3-2**).

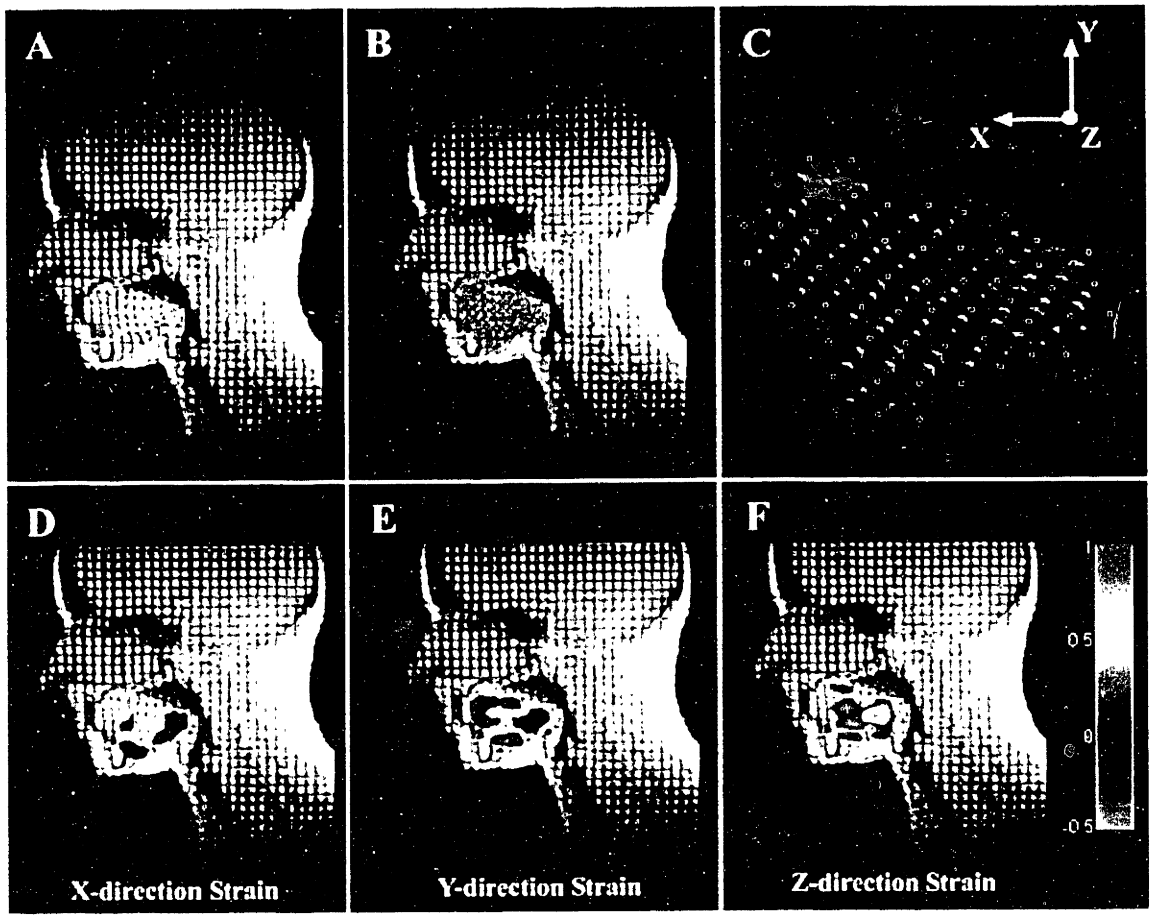

Figure 3-20 Lingual strain during late accommodation were visualized with strain maps and octahedra. The combination of y direction contraction in the posterior tongue and expansion in the anterior tongue results in shifting of the bolus to the posterior dorsal surface of the tongue, consistent principally with contraction of the posterior genioglossus and concomitant x and z direction expansion.

During the propulsive phase of the swallow (Figure 3-21), the bolus is propelled retrograde into the oropharynx by posterior displacement and deformation of tongue tissue. During this phase, the strain results in the posterior genioglossus presented expansive x and y direction strain (peaking at 0.469 and 0.684 respectively), and contractile z direction strain (peaking at -0.374). These results were also seen as statistically significant deformation patterns in inter-subject mean strain calculations ($p < 0.001$) (**Table 3-2**). This result was consistent with the existence of postero-superior directed passive stretch in the midline, and suggests concurrent contraction of the laterally inserted styloglossus (not visualized in the current study), as well as contraction of the z directed muscle fibers characteristic of the intrinsic transversus muscle.

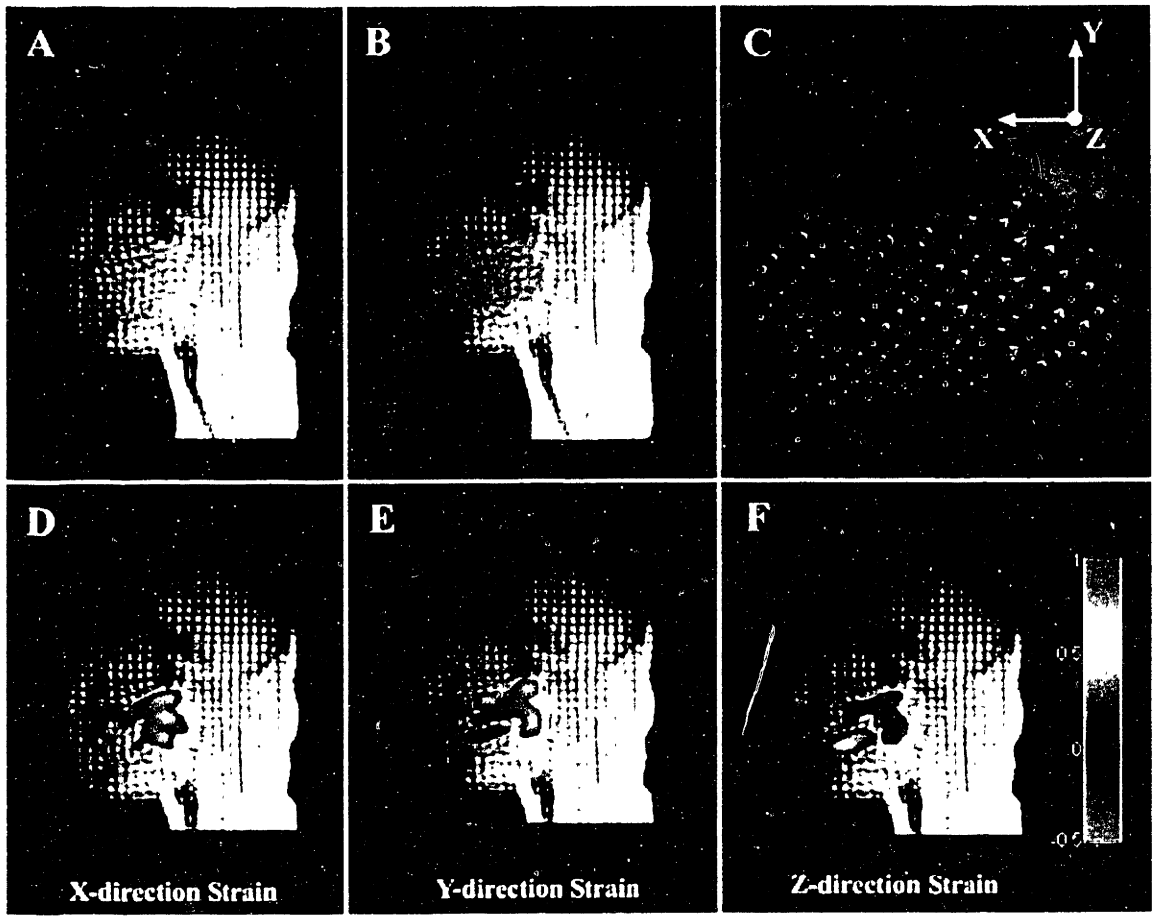

Figure 3-21 Lingual strain during propulsion was visualized by color-coded strain maps and strain tensor octahedra. X and y direction expansion in the posterior tongue was consistent with contraction of the laterally-inserted styloglossus (with associated passive drag) and z direction contraction of the posterior located transversus fibers. This synergistic contraction exemplifies a common property in the tongue – that of muscular redundancy.

In addition to the previous figures, inter-subject axial strain statistics (mean, standard deviation, and p-value) were tabulated for each of four functional zones of the tongue (**Table 3-2**). These zones corresponded to distinct myoarchitectural regions (see **Figure 3-18** for more detail). Low p-values associated with the strain statistics indicated that a certain axial strain value was pervasive amongst the sample of subjects tested.

EARLY ACCOMMODATION				LATE ACCOMMODATION				PROPULSION			
ZONE 1				ZONE 1				ZONE 1			
	mean	st.dev	p-val		mean	st.dev	p-val		mean	st.dev	p-val
x	0.135	0.121	0.0081	x	0.027	0.063	0.1726	x	0.034	0.053	0.0680
y	-0.006	0.105	0 4345	y	0.136	0 089	0.0067	y	0.083	0 067	0 0085
z	0.034	0.114	0.2140	z	-0.048	0.066	0 0685	z	-0.031	0.064	0.1252
ZONE 2				ZONE 2				ZONE 2			
	mean	st.dev	p-val		mean	st.dev	p-val		mean	st.dev	p-val
x	0.188	0.071	0.0001	x	-0.009	0 040	0 2981	x	0.065	0.081	0.0388
y	-0.165	0.054	0.00003	y	-0.074	0.062	0 0163	y	0.050	0.093	0.1045
z	0.179	0 114	0.0015	z	0 192	0 093	0.0020	z	-0 014	0.080	0 3323
ZONE 3				ZONE 3				ZONE 3			
	mean	st.dev	p-val		mean	st.dev	p-val		mean	st.dev	p-val
x	0.083	0.057	0.0023	x	0 131	0 043	0.0003	x	0.173	0.045	0.00003
y	-0.034	0.035	0 0140	y	-0 125	0 061	0.0020	y	0.098	0 050	0 0010
z	0.021	0.054	0 1526	z	0.202	0 134	0 0071	z	-0.109	0 040	0 0002
ZONE 4				ZONE 4				ZONE 4			
	mean	st.dev	p-val		mean	st.dev	p-val		mean	st.dev	p-val
x	0 093	0.046	0.0004	x	0 073	0 047	0 0063	x	0 064	0.044	0.0043
y	-0.050	0.063	0 0312	y	-0 010	0 070	0 3688	y	0 008	0.058	0 3713
z	0 032	0.072	0 1272	z	0.023	0 101	0 2984	z	-0.004	0 061	0 4275
n =8				n =6				n =7			

Table 3-2 Axial strain in the tongue was quantified for the three functional phases of oral stage deglutition. Means, standard deviations, and p-values were tabulated for early accommodation, (n = 8), late accommodation (n = 6), and propulsion (n = 7), for each of four functional zones of the tongue. The data were also organized by axial strain along each spatial direction (x, y, and z).

3.4.3 Discussion: Deglutition

The tongue is a muscular organ, which is instrumental in the manipulation, configuration, and delivery of the ingested bolus from the oral cavity to the oropharynx during swallowing. These functions are carried out through a series of characteristic deformations, which are designed to first control (early and late accommodation) and then rapidly propel the bolus (propulsion). In order to determine the intramural dynamics of the lingual musculature associated with these deformations,

tagging magnetic resonance imaging was used to quantify local muscle deformation (i.e. strain) in relation to overall tissue shape.

Early accommodation was characterized by the containment of the bolus in a grooved depression at the middle portion of the tongue's dorsal surface. This grooved depression appeared to have been created by a synergistic contraction of the anterior genioglossus in concert with the hyoglossus, verticalis (intrinsic), and transversus (intrinsic) muscles. Verticalis contraction was seen as a region of negative y-direction strain in the anterior tongue (**Figure 3-19d**), resulting in x-direction expansion of the tongue tip toward the incisors. Transversus contraction was suggested on the basis of subtle z-direction negative strain (**Figure 3-19e**). There was, however, strong evidence of negative y-direction strain directly below the bolus, producing a depression of the containing groove. This tissue contraction could be the direct result of genioglossus contraction, or could have been caused through passive drag by contraction of the hyoglossus, which inserts into the mid-portion of the tongue body, laterally from below (hence not visualized in the mid-sagittal slice). Genioglossus contraction in the swallow has been demonstrated by previous EMG studies (Miyawaki, Hirose et al., 1975); whereas, synergistic involvement of the hyoglossus could be inferred from the strain tensor visualization map (**Figure 3-19c**). This strain map demonstrated that the contractile eigenvectors (visualized as the short axes of octahedra – the direction of greatest contractile strain when z-direction strain is positive) were oriented postero-inferiorly. Since the mid-sagittal slice is directly medial to the lateral insertions of the hyoglossus, this strain pattern was consistent with either genioglossus or hyoglossus contraction, occurring independently or in concert. These contractions were associated with x and z-direction expansion in this region, elongating the grooved depression and improving bolus containment. A common observation in early accommodation is the placement of the tongue tip behind the upper incisors (Miller, 1982). While not evidenced directly by our strain mapping results, this action may be aided by a slight sagittal bending action imparted by contraction of the superior longitudinalis. X-direction expansion in the posterior tongue aided in closing off the oropharynx to the contained bolus.

Late accommodation was characterized by a shifting of the bolus toward the posterior dorsal surface of the tongue, in effect, "priming the lingual pump" before eventual propulsion into the oropharynx. The soft palate was shifted superiorly, thus closing off the nasopharynx. The most prominent finding during this phase was an increase of negative y-direction strain (i.e. inferior-directed contraction) in the posterior region of the tongue, which contained the bolus. This contraction is responsible both for the creation of the posterior depression, and for the extension of the bolus depression in the x and z directions (due to tissue incompressibility). The extent to which these contractions are due to activity of the posterior fibers of the genioglossus or to passive drag secondary

to hyoglossus contraction cannot be conclusively determined from these data. The genioglossus fans out into the mid-sagittal slice from its attachment on the mandible and would present octahedral long axes oriented anterior-inferiorly. In contrast, the hyoglossus originates from the hyoid bone and enters the mid-posterior tongue at its lateral aspect, and would thus produce octahedral long axes oriented posterior-inferiorly. Some strain tensor octahedra in the posterior tongue do tilt postero-inferiorly, providing evidence that there is at least some contractile assistance from the hyoglossus (**Figure 3-20c**). Conceivably, the degree to which these muscles contribute to the accommodating depression in the posterior tongue may also vary as a function of bolus volume or viscosity, or as a function of pathological regulation of tongue contractility. Translation of the contractile region from the anterior to the posterior genioglossus (early to late accommodation) transferred the bolus retrograde via the grooved depression, preparing the bolus for propulsion.

Bolus propulsion was characterized by the retrograde motion of the tongue toward the pharyngeal wall, thus expelling the cradled bolus from the oral cavity. The most prominent effect was on the posterior tongue, with significant expansion of the tissue in the x and y directions and concomitant z direction contraction. The styloglossus, which inserts into the posterior tongue body on its lateral aspects and is directed postero-superiorly towards its attachment point on the styloid process, most likely produced this universally observed strain pattern by passively dragging the tissue in the tongue's mid-sagittal slice. This mechanism was supplemented by contraction of intrinsic transversus muscle fibers, which are also located in the posterior tongue. This contraction would cause tissue expansion in the x and y directions due to incompressibility of the tongue tissue. Octahedra in the posterior tongue had their principal eigenvector (octahedral long axis), or the direction of greatest expansion, oriented in a postero-superior direction. Sole contraction of the styloglossus (in a postero-superior direction) could not produce expansive strain *above* its insertion point, in the mid-portion of the tongue's lateral surfaces since the tongue is constrained from below. Thus, styloglossus contraction could only stretch the tongue tissue located between its insertion point and the tongue's inferior attachment. Because postero-superior expansion in the posterior tongue was seen to exist all the way to the dorsal surface, a synergistic mechanism must be at work. This effect could only come from contraction of the z-directed transversus muscle, posteriorly located in the intrinsic core.

Axial strain values were reported as the mean of all elements in a given region across all subjects (**Table 3-2**), as well as peak values in a given region for a representative subject. While the former technique sufficiently mitigates spurious digitization errors, accounts for inter-subject variability, and provides a datum for gross activity in the region, the result may not differentiate two distinct contractile regions or contraction of only a portion of the muscle, such as localized

genioglossus contraction of specific motor units. Conversely, the latter technique of reporting maximum and minimum peak values could potentially differentiate localized muscle function (at the resolution of the element), however it is highly sensitive to digitization error.

Since the imaging technique was inherently two-dimensional, the calculation of axial strain in the through-plane direction (at right angles to the sagittal imaging plane) required two key assumptions: 1) The tissue maintained a constant volume with deformation, i.e. incompressibility condition, and 2) through-plane shear strain was negligible. The latter condition is valid for tongue motions, which are symmetric about the midline sagittal plane, as was the case for normal swallows. However, these assumptions may not be valid under pathological conditions in which one region of the tongue is asymmetrically affected, such as stroke or muscular tissue injury. The application of tagging MRI in these settings may thus require accurate gating of MR imaging to swallow onset, thereby significantly lowering imaging time and permitting the application of the technique along asymmetric slices without significant motion artifact.

These data were consistent with a biomechanical model in which the intrinsic and extrinsic fibers function synergistically rather than as independent actuators. In this regard, the unique myoarchitecture of the tongue allows the organ to function efficiently as a muscular hydrostat (Smith and Kier, 1989); a term whose properties include 1) tissue incompressibility derived from a highly aqueous composition and 2) the ability to elicit tissue deformation while simultaneously providing skeletal support for that tissue. Contracting lingual myofibers induce tissue compression along fiber directions and tissue expansion along directions orthogonal to the fibers (due to tissue incompressibility). In both accommodation and propulsion, physiologic function was performed though a synergistic combination of tissue compression and expansion. In fact, tissue incompressibility necessitated the simultaneous existence of both compression and expansion for a given tissue element, while the tongue's interdigitating myofibers insured that compression/expansion coupling synergistically produced the intended function. Conceivably, deglutitive function in patients with oral stage dysphagia may be impaired through a pathological reorganization of the underlying myoarchitecture. This myopathic condition could then produce a dysfunctional alteration of this compression/expansion distribution.

Chapter 4

4 An Analog Model of Sagittal Tongue Bending

The human tongue is a versatile muscular organ, whose structural complexity provides interesting modeling challenges. In this chapter, we further explore the tongue's structure-function relationships by synthesizing the myoarchitectural characteristics of the tongue (Chapter 2) with the organ's physiological characteristics (Chapter 3). Specifically, we modeled a primitive movement of the tongue, sagittal tongue bending. This deformation can be considered a foundation of the lingual deformations seen in oral phase swallowing, wherein the tongue undergoes sagittal bending to place the tip posterior to the top row of teeth, forming an accommodation pouch in which a bolus of food is held. Sagittal bending is one of several primitive deformations assumed by the tongue during swallowing. Classically, superior-directed tongue bending is considered to result from contraction of the superior longitudinalis muscle alone (Smith and Kier, 1989). In contrast, we hypothesized that sagittal bending may be better depicted by the combined contractions of the transversus and the longitudinalis muscles. This theory converges well with the depiction of the tongue as a muscular hydrostat (Kier and Smith, 1985; Smith and Kier, 1989), an organ that functions by deforming in a plane orthogonal to the contraction axis by conservation of volume. One of the goals of this modeling effort was to evaluate the extent to which combined contractions of the transversus and longitudinalis muscle account for sagittal tongue bending. In order to validate our model, we compared the theoretical results to the previously published empirical measurements obtained by Tagging MRI and presented in Chapter 3 (Napadow, Chen et al., 1999).

The theoretical model of tongue bending was based on classical bimetal strip theory (Suhir, 1989; Matthys and DeMey, 1996), which is typically applied in electronics design. Bimetal strip theory applies to the case in which two metals of different thermal expansion coefficient are bonded together at an interface and are subjected to a temperature change (Timoshenko, 1925). Under these conditions, the thermal expansion response of each layer differs, yet the bond between the layers remains fixed. Thus, the only way for the strip to accommodate the differing expansions is to bend. Development of

this theory was important in electronics design, where thermal mismatch stresses and strains between two attached devices can produce failure at the material interface. In addition, this theory has also been applied to the design of thermostats which work by the transduction of temperature change into a bent beam deflection (Timoshenko, 1925). In the case of sagittal tongue bending, a beam curvature is produced when one muscle layer (specifically the longitudinalis muscle) contracts more so than the other layers. Hence, if muscular contractile strain can be considered analogous to thermal contractile strain, the layered muscular sandwich within the tongue can be adequately modeled by a classical bimetal strip. One strip layer was composed of the superior longitudinalis muscle and was bonded to the other layer, composed of the transversus and verticalis muscles. Once the strip was subjected to a temperature change, contraction of the longitudinalis and transversus muscles was accomplished by specifying the directionally dependent thermal expansion coefficients for the different layers.

Previous models of lingual muscular activity have emphasized relatively simple geometry and few elements, incorporating realistic activation and dynamics properties (Chiel, Crago et al., 1992), as well as multi-element finite element models, incorporating correct three-dimensional geometry and viscoelastic constitutive properties (Wilhelms-Tricarico, 1995). The geometry of the former model was particular to certain reptilian tongues and significantly divergent from human tongues. The latter model's complexity provided greater flexibility of deformation, yet introduced model instability when setting optimization functions. Still other models have adopted a two-dimensional approach to simulate intrinsic and extrinsic contractions in the human tongue by subdividing the muscular organ into gross directional myofiber elements (Hashimoto and Suga, 1986; Sanguineti, Laboissiere et al., 1997). While not wholly parcellating the organ as a finite element model, these models attempted to retain some of the flexibility of a generalized description, while still somewhat limiting the scope of investigation. For instance, both of these models utilized linear elastic isotropic constitutive descriptions. Model comparisons to empirical results were lacking. However, the Hashimoto and Suga model, which involved tongue deformations in the production of vowel sounds, was validated by comparison to cine x-ray images.

Our model differed from past investigations in that it was an analog model comparing the tongue to a common mechanical engineering device, a bi-layered beam with differing thermal expansion properties. Secondly, we validated our model with not just gross geometry (i.e. global curvature through cine x-ray), but with internal deformation metrics (i.e. cross-sectional axial strain profile determined by Tagging MRI). This model was created to answer a specific question: to what extent are different muscular elements of the human tongue involved in the tongue deformation: sagittal bending toward the hard palate.

4.1 Modeling Methodology

4.1.1 Development and validation of analog model

Our mechanical analog model was compared to strain measurement data derived from a prior tagging MRI study (Napadow, Chen et al., 1999). In this study, we explored two different mechanisms by which the tongue might achieve sagittal bending in vivo. One mechanism required the superior longitudinalis muscle to contract without concurrent contraction of the inferior longitudinalis muscle (otherwise the tongue would simply shorten), thereby producing a longitudinal strain gradient through the cross-section as well as a curved global deformation, consistent with sagittal bending. By an alternative mechanism, superior longitudinalis muscle contraction was aided by contraction of the transversus muscle, which produced an anticlastic curvature about the medial-lateral axis, thereby augmenting sagittal bending.

In order to address this mechanistic distinction, we modeled the tongue as a composite beam, which has an initial curvature in its rest configuration, and then undergoes a change in curvature due to dissimilar contraction patterns of the beam elements. The top beam element (beam 1) represents the longitudinalis muscle layer, while the bottom beam element (beam 2) represents the intrinsic core of the tongue which is composed of the transversus and verticalis muscles. Muscular contraction has been simulated in the bimetal strip model by assigning different thermal expansion coefficients ($\alpha(\mathbf{x})$) to the different beam layers. Using this approach, we assessed the relative contribution of the transversus and longitudinalis muscles to sagittal bending.

The bimetal strip bent beam analog solution is derived from the classical mechanics theory (Timoshenko, 1925; Shanley, 1957) with several modifications. The following assumptions were made in order to produce a set of governing equations which could be readily solved by analytical methods: (1) cross-sections originally planar and perpendicular to the beam's curved long axis, remain planar and perpendicular to the new curved long axis after deformation, (2) contraction does not produce shear deformation, i.e. only pure bending is modeled (Bernoulli-Euler beams), (3) the two beams are connected by rigid plates at the ends, hence concentrated force at the ends is transformed into a linear stress variation through the cross-section (otherwise shear deformation occurs at the ends, conflicting with assumption 1), (4) the solutions for concurrent contractions of the longitudinalis and transversus muscles can be superimposed, and lastly (5) both beams were assumed to be comprised of isotropic, linear elastic materials with orthotropic thermal expansion coefficients.

In classical bimetal strip theory, a composite beam is formed by two beams of different material composition bonded at an interface. The two beams can have different thickness (h_1, h_2), Young's modulus (E_1, E_2), Poisson's ratio (ν_1, ν_2), and thermal expansion coefficient (α_1, α_2). **Table 4-1** contains definitions of the relevant parameters used in the model.

Parameter	Definition
h_1:	Height of beam 1 (superior longitudinalis m.)
h_2:	Height of beam 2 (transversus and verticalis m.)
h:	Total height of bimetal strip ($h = h_1+h_2$)
b:	Width of beam
L:	Length of beam (measured along convex edge)
E_1:	Young's Modulus of beam 1
E_2:	Young's Modulus of beam 2
ν_1:	Poisson's ratio for beam 1
ν_2:	Poisson's ratio for beam 2
α_1:	Thermal expansion coefficient for beam 1
α_2:	Thermal expansion coefficient for beam 2
ΔT:	Temperature change experienced by the bimetal strip
R_o:	Initial radius of curvature to bimetal strip neutral axis
k_o:	Initial curvature ($k_o=1/R_o$)
R_{o1}:	Initial radius of curvature to beam 1 neutral axis
R_{o2}:	Initial radius of curvature to beam 1 neutral axis
R_b:	Radius of curvature induced by the bending moment
R_f:	Final radius of curvature of bimetal strip neutral axis
P_1:	Axial load applied to beam 1
P_2:	Axial load applied to beam 2
M_1:	Moment applied to beam 1
M_2:	Moment applied to beam 2

Table 4-1 Model Parameter Definitions

If $\alpha_1 > \alpha_2$ and there is a temperature drop ΔT, beam 1 will want to contract more than beam 2. However, since the two beams are bonded together, beam 2 restricts beam 1's contraction by applying shearing forces at the bonding interface. If each beam is then taken as a separate free-body diagram, the shearing forces, since they are not applied centrally, produce bending moments on each beam. These

two moments may be different since the beams can have different thickness; however, equilibrium dictates that the sum of the moments must equal the moment-couple created by the shearing forces acting centrally on each beam (**Figure 4-1**):

$$P_1 = P_2 = P \tag{4.1}$$

$$M_1 + M_2 = P_1\left(\frac{h_1}{2}\right) + P_2\left(\frac{h_2}{2}\right) = P\left(\frac{h}{2}\right) \tag{4.2}$$

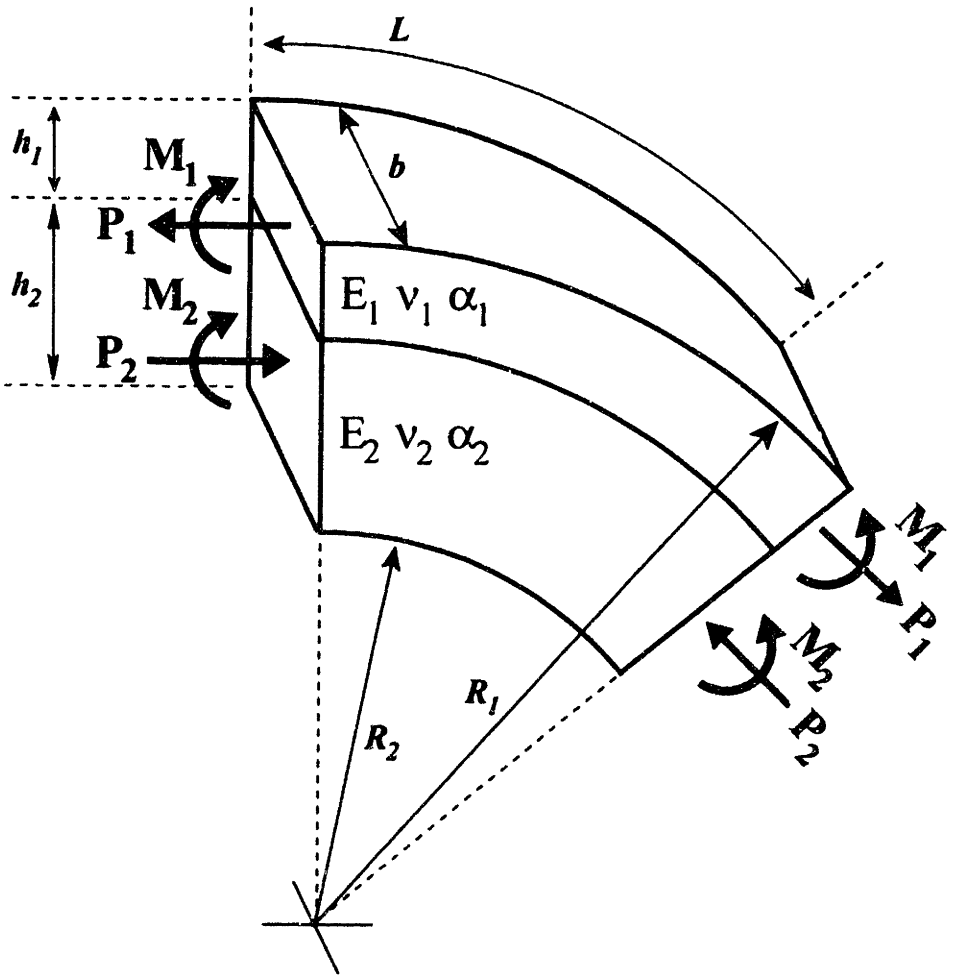

Figure 4-1 The analog model was defined by two materials bonded together at an interface. The bimetal strip was initially concave-downward; each material was constituitively defined by its material properties and spatial dimensions (see Table 4-1). Upon contraction of the top material, the "bimetal strip" is subjected to the forces and moments defined on the schematic.

Constitutive relations describe the relationship of material deformation to loading. For the case of a curved beam bimetal strip problem, the relationship between moment and curvature can be found

by integrating the differential moment produced by the bending stress distribution across the indicated cross-section.

$$M = \int y\sigma \, dA \tag{4.3}$$

Since the curvature changes that are anticipated in the tongue model are very large, linear strain definitions could not be used. Instead, we chose to use Green's strain, $\varepsilon = {}^1/_2(U^2-1)$, to define non-linear bending strain in a curved beam (see **Appendix F** for derivation):

$$\varepsilon = \frac{1}{2}\left[\left(1+\frac{yR_o}{y+R_o}\left(\frac{1}{R_b}\right)\right)^2 - 1\right] \tag{4.4}$$

where y is the distance from the neutral axis, R_o is the original radius of curvature to the neutral axis of the curved beam (see **Appendix F** for derivation of R_o), and R_b is the radius of curvature caused by the bending moment, M. Using equation (4.4) and assuming that tongue musculature behaves as a linear elastic material, equation (4.3) can be evaluated analytically:

$$\begin{aligned} M = {} & \frac{Eb}{2(1-\nu^2)}\left[(R_1+R_2)hR_o - 4hR_o^2 + 2R_o^3 \ln\frac{R_2}{R_1}\right]\left(\frac{1}{R_b}\right) \\ & + \frac{Eb}{4(1-\nu^2)}\left[(R_1+R_2)hR_o^2 - 6hR_o^3 + 6R_o^4 \ln\frac{R_2}{R_1} + 2R_o^5\left(\frac{1}{R_2}-\frac{1}{R_1}\right)\right]\left(\frac{1}{R_b^2}\right) \end{aligned} \tag{4.5}$$

where b is the width of the beam, and R_1 and R_2 are the inner and outer radii, respectively, of a beam initially bent concave down. Note that M is defined to be positive clockwise. Hence, the non-linear strain definition produces a moment-curvature relation, which is itself quadratic.

In order to solve for the curvature produced by a given contraction, a compatibility relation must be imposed at the interface of the two beams. That is, for the two beams to remain bonded at the interface, the longitudinal strain experienced by the lower plane of the upper beam and that experienced by the upper plane of the lower beam must be equal. The longitudinal strain is the sum of the thermal, axial, and bending strain. At the interface, this strain matching can be expressed mathematically as:

$$\varepsilon_{xx_1}(R_2+h_2) = \varepsilon_{xx_2}(R_2+h_2) \tag{4.6}$$

$$\alpha_1\Delta T + \frac{P}{E_1h_1b} + \frac{1}{2}\left[\left(1+\frac{(R_2+h_2-R_{o_1})R_{o_1}}{R_2+h_2}\left(\frac{1}{R_b}\right)\right)^2-1\right] = \alpha_2\Delta T - \frac{P}{E_2h_2b} + \frac{1}{2}\left[\left(1+\frac{(R_2+h_2-R_{o_2})R_{o_2}}{R_2+h_2}\left(\frac{1}{R_b}\right)\right)^2-1\right]$$

where R_{o_1} and R_{o_2} are the radius of curvature to the neutral axis of beam 1 and beam 2, respectively. Finally, the change in curvature produced in the bimetal strip can be found by combining equation (4.6) with equation (4.2) (in elasticity theory, this is a combination of equilibrium, constitutive relations, and compatibility). The radius of curvature produced by the bending moments acting on the strip can be found by solving the quadratic equation:

$$\left[\frac{(R_2+h_2-R_{o_1})^2R_{o_1}^2-(R_2+h_2-R_{o_2})^2R_{o_2}^2}{(R_2+h_2)^2} - \frac{4(B_1+B_2)}{h}\left(\frac{1}{E_1h_1}+\frac{1}{E_2h_2}\right)\right]\frac{1}{\mathbf{R_b^2}} +$$

$$\left[\frac{2\left[(R_2+h_2)(R_{o_1}-R_{o_2})+R_{o_2}^2-R_{o_1}^2\right]}{R_2+h_2} - \frac{4(A_1+A_2)}{h}\left(\frac{1}{E_1h_1}+\frac{1}{E_2h_2}\right)\right]\frac{1}{\mathbf{R_b}} + 2(\alpha_1-\alpha_2)\Delta T = 0 \tag{4.7}$$

where A_1 and A_2 represent the constant in front of the linear term in equation (4.5) for beam 1 and beam 2, respectively. B_1 and B_2 represent the constant in front of the quadratic term in equation (4.5) for beam 1 and beam 2, respectively. A sensitivity analysis of these equations was completed wherein the effect of varying a given parameter was evaluated by the variability induced on the computed curvature.

The final radius, R_f, of the bimetal strip can now be found. A beam with initial curvature R_o, undergoing bending described by a change in curvature of radius R_b, assumes a final radius defined by:

$$\frac{1}{R_f} = \frac{1}{R_b} + \frac{1}{R_o} \tag{4.8}$$

Contraction of the superior longitudinalis muscle produces bending in the x-y plane. However, due to the existence of Poisson's effects, an anticlastic curvature in the beam is formed in the y-z plane (**Figure 4-2**). This curvature (which can be seen when bending a common rectangular rubber eraser) is equal to $-\nu/\rho$, where ρ is the radius of curvature for bending in the x-y plane and ν is Poisson's ratio, which was set to ½, corresponding to an incompressible material. Tissue incompressibility is commonly assumed in tongue models (Chiel, Crago et al., 1992; Wilhelms-Tricarico, 1995) as the tissue is highly aqueous. This is what gives the tongue its capability to behave as a muscular hydrostat. Intuitively, the anticlastic curvature can be explained by the fact that the concave edge of a bent beam is in compression along the longitudinal dimension (x), while the convex edge is in tension. Thus, by Poisson's effect, the concave edge must be in tension along the orthogonal through-plane dimension (z), while the convex edge must be in compression along this dimension. The consequence is that a secondary curvature is formed in the beam in the y-z plane; this curvature is called the anticlastic curvature. In fact, it is this curvature that explains how contraction of the transversus muscle can augment the contraction of the superior longitudinalis muscle in producing sagittal bending (x-y plane) of the tongue. Contraction of the transversus muscle produces a curvature in the y-z plane, and can be modeled in a similar manner by a bimetal strip analog. In addition, this contraction produces an anticlastic curvature, this time in the x-y plane, which augments sagittal tongue bending. In our model, superposition was used to combine the effects of superior longitudinalis and transversus muscle contraction.

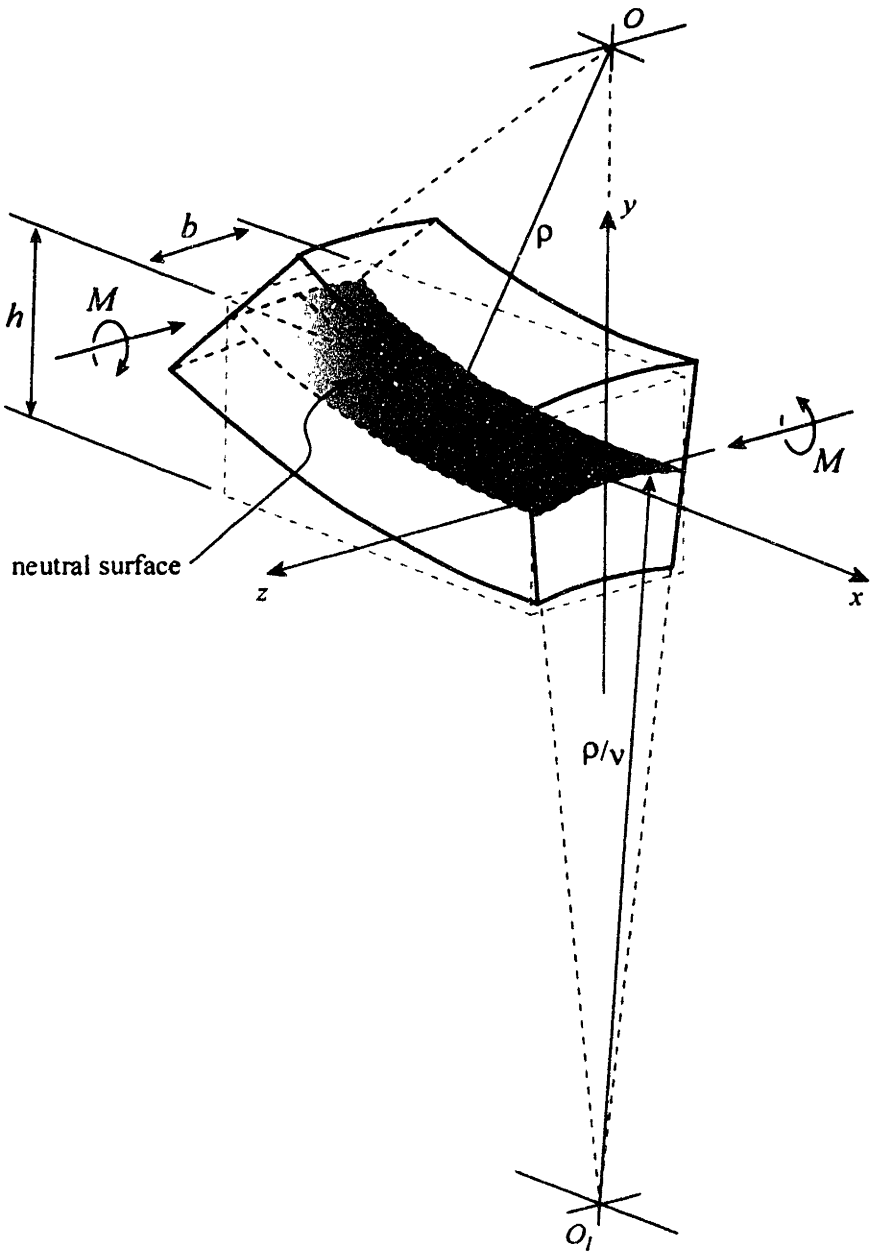

Figure 4-2 The phenomenon of anticlastic curvature arises from Poisson effects. When a beam is bent, the concave edge is under longitudinal compression, while the convex edge is under longitudinal tension. Poisson's effect dictates that the contracted edge must expand orthogonally, while the edge under tension must contract orthogonally. This requirement creates a curvature (the anticlastic curvature), which is itself in a plane orthogonal to the plane of primary bending.

Model parameters were derived principally from MRI images and the Visible Human: Male database (**Figure 4-3, Table 4-2**). MRI images of the same human subject from whom the empirical strain data were derived, were used to measure total height of beam, h; width of beam, b; length of beam, L; initial curvature, R_o; and final curvature, R_f (which was used to help corroborate model output). The initial and final curvatures were measured by fitting a circle to a set of points digitized along a contour (**Figure 4-4**). This was accomplished by minimizing the rms error while varying the circle radius and center location. A mid-sagittal slice from the Visible Human Male database was used to find the percentage composition of dorsal epithelium, superior longitudinalis muscle, transversus/verticalis muscles, inferior longitudinalis muscle, lingual gland and frenulum in a transverse x-section through the anterior tongue (approximate location from which the empirical strain data was derived). These data were used to find the heights of the individual beams, h_1 and h_2. The Young's Modulus, E, of contracted (E=0.01 MPa) and relaxed muscle (E=0.006 MPa) was found from other tongue models in the literature (Sanguineti, Laboissiere et al., 1997) and material test results (Duck, 1990). Finally, muscle contraction was modeled by assigning specific values to the thermal expansion coefficients of each beam. Due to the lack of adequate data on human tongue muscle, results from the frog (*Rana pipiens*) sartorius muscle were used (Matsumoto, 1967). The strain of muscular contraction was found to be -0.3 using the length changes (l_{new}/l_o = 0.7) reported by this reference for isotonic contractions under low load. This value was also affirmed by Gans and Bock, 1965, who stated that, "the vast majority of entire muscles cannot shorten by more than 30%..." (Gans and Bock, 1965; Kier and Smith, 1985). Thus, if the temperature change, ΔT, is set to -1°C, contracted muscle was defined by a thermal expansion coefficient, α, equal to $0.3°C^{-1}$, while uncontracted muscle was defined by an α equal to $0°C^{-1}$.

The results of both of the tested contraction scenarios (superior longitudinalis muscle alone and both superior longitudinalis and transversus muscles) was visualized by a bent beam graphic showing the modeled beam in its final, contracted configuration. Beam deflection was tracked by visualizing the deflection of 75 points defining the convex, concave, and interfacial contours.

Parameter	Value	Source
h_1:	2.0mm	Visible Human data, MRI
h_2:	5.8mm	Visible Human data, MRI
b:	30.0mm	MRI
L:	35.0mm	MRI
E_1(run 1):	0.01MPa	Duck, 1990
E_2(run 1):	0.006Mpa	Duck, 1990
E_1(run 2):	0.01MPa	Duck, 1990
E_2(run 2):	0.01Mpa	Duck, 1990
ν_1:	0.5	Duck, 1990
ν_2:	0.5	Duck, 1990
$\alpha_{1\text{-}x}$(run 1):	$0.3°C^{-1}$	Matsumoto, 1967
$\alpha_{2\text{-}x}$(run 1):	$0°C^{-1}$	Matsumoto, 1967
$\alpha_{1\text{-}z}$(run 1):	$0°C^{-1}$	Matsumoto, 1967
$\alpha_{2\text{-}z}$(run 1):	$0°C^{-1}$	Matsumoto, 1967
$\alpha_{1\text{-}x}$(run 2):	$0.3°C^{-1}$	Matsumoto, 1967
$\alpha_{2\text{-}x}$(run 2):	$0°C^{-1}$	Matsumoto, 1967
$\alpha_{1\text{-}z}$(run 2):	$0°C^{-1}$	Matsumoto, 1967
$\alpha_{2\text{-}z}$(run 2):	$0.3°C^{-1}$	Matsumoto, 1967
ΔT:	-1°C	Matsumoto, 1967
k_o:	$28.5\ m^{-1}$	MRI

Table 4-2 Model Parameter Values

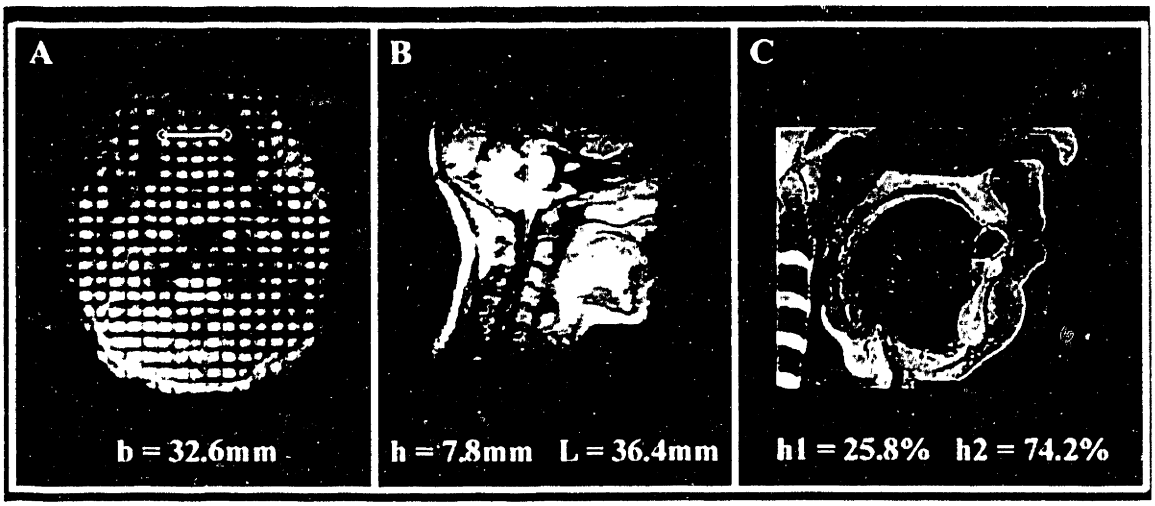

Figure 4-3 The spatial parameters used in the model were derived from either MRI images of the tongue or the Visible Human Male database. (A) Coronal view MRI image (with tag lines superimposed) of the tongue depicting the width, b = 32.6 mm, of the tissue in the mid-anterior position. (B) Sagittal view MRI image of the tongue depicting the functional length along its curvatures of the anterior tongue, 36.4 mm, and the corresponding height, h = 7.8 mm. (C) Sagittal view cross-section of the muscular structure of the anterior tongue derived from the Visible Human database, showing the relative composition percentage of the longitudinal (25.8%) and transverse (74.2%) muscle layers.

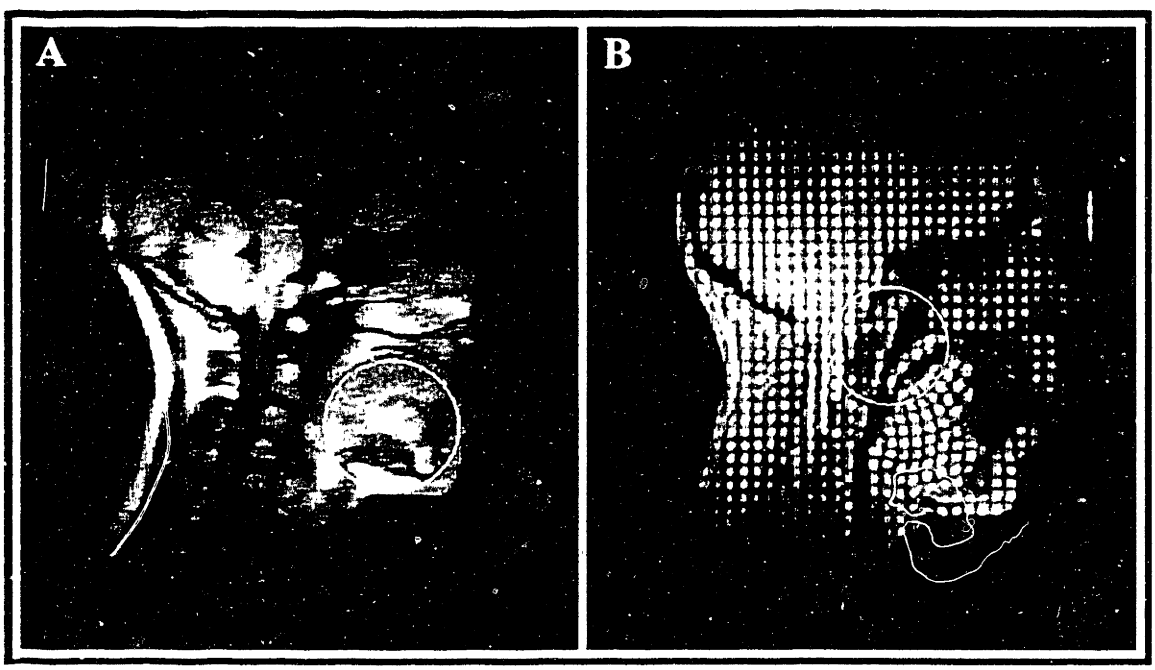

Figure 4-4 The initial (A) and final (B) tongue curvatures were measured by fitting a cubic B-spline curve to the [illegible] approximate shapes of the tongue/airway interfaces. The B-spline curve was [illegible] MRI image [illegible] MRI data.

4.1.2 Correlation of analog model with empirical data (Tagging MRI)

Corroboration of theoretical results with empirical results was accomplished by both comparing the final curvature achieved in modeled and real deflection (MRI); as well as by comparing the longitudinal strains calculated across the tongue cross-section in the model with the longitudinal strains derived from the Tagging MRI data for sagittal bending. The MRI data were taken from the anterior tongue within the portion corresponding anatomically to the superior longitudinalis and transversus muscles. This portion was deduced by cross-sectional percentage measurements from the Visible Human: Male data.

Tagging MRI has been previously used to derive qualitative and quantitative measures of internal tissue deformation (Niitsu, Kumada et al., 1994; Napadow, Chen et al., 1999; Napadow, Chen et al., 1999) and was described in Chapter 3. In brief, Tagging MRI is a non-invasive NMR tagging technique that allowed for the selective saturation of bands of magnetic spins in resting tongue tissue (Zerhouni, Parish et al., 1988; Axel and Dougherty, 1989; Young and Axel, 1992). These bands were localized along the antero-posterior and superior-inferior directions of the mid-sagittal plane, resulting in a square rectilinear grid. As the tongue tissue deformed, the previously rectilinear grid also deformed, and axial and shear strains relative to the rest condition were determined by imaging the tongue in its deformed state, thereby tracking the relative displacement of triangular element nodes defined by MR tag line intersections.

4.2 Results of Analog Modeling

The results of this analysis demonstrated that sagittal tongue bending could be adequately represented by an analog beam model, and could, in fact, be depicted in terms of the contractions of the tongue's constituting myofiber populations.

From its initial curved state, the tongue was found to reverse its curvature under both the "superior longitudinalis muscle only" contraction scenario, as well as the scenario wherein both the superior longitudinalis and transversus muscles contract (**Table 4-3, Figure 4-5**). Positive curvature is defined as concave down, while negative curvature is defined as concave up (i.e. sagittal tongue bending). Under the condition of longitudinalis muscle contraction alone, the moment produced by the contraction induced a curvature change of $-46.9 m^{-1}$, which resulted in a final curvature of $-18.4\ m^{-1}$.

	Longitudinalis m. only Contraction	Longitudinalis and Transversus m. Contraction
Initial curvature ($k_o=1/R_o$)	28.5 m^{-1}	28.5 m^{-1}
Curvature induced by contraction (k_b)	-46.9 m^{-1}	-58.8 m^{-1}
Final curvature (simulated k_f)	-18.4 m^{-1}	-30.4 m^{-1}
Final curvature (empirical k_f)	-30.9 m^{-1}	-30.9 m^{-1}
% Error	**40%**	**2%**

Table 4-3 The global results of both contraction scenarios are expressed by the pre and post contraction lingual curvature under both contraction scenarios - longitudinalis only, and synergistic longitudinalis and transversus contraction. The results demonstrated that compared to the actual empirically derived sagittal curvature, the longitudinalis only contraction scenario was considerably in error; whereas, the synergistic contraction scenario predicted a final curvature that very closely approximated the actual curvature.

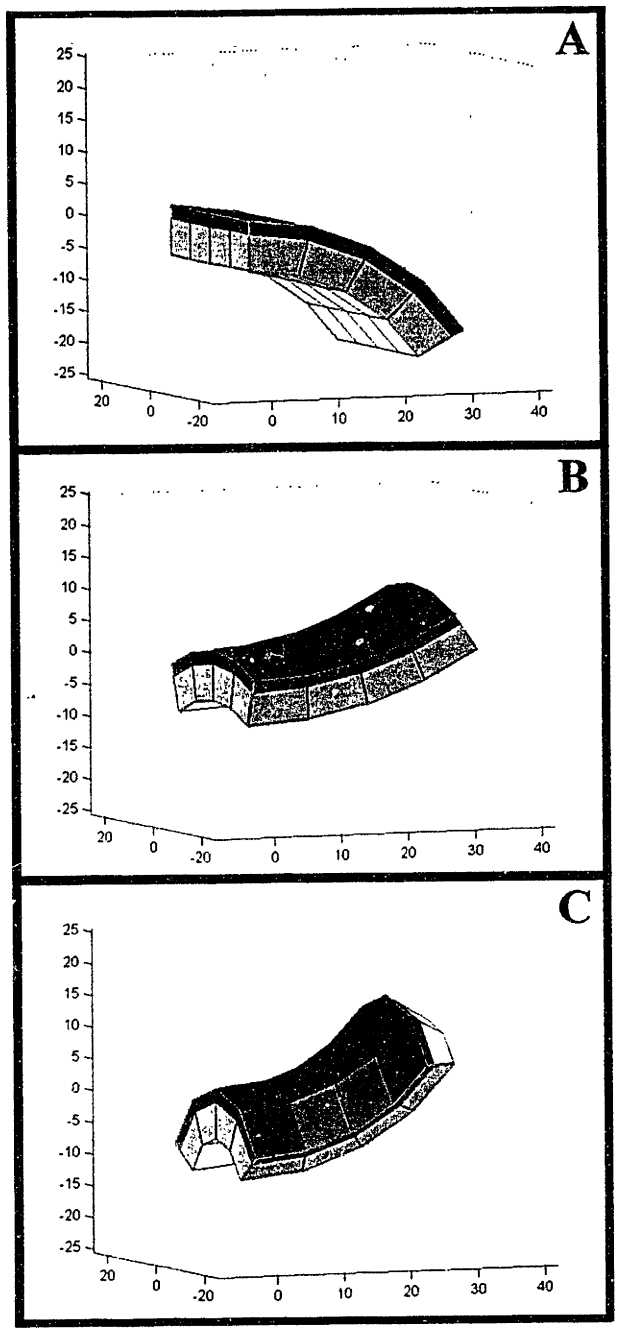

Figure 4-5 Shown are the graphic representations of the 3D model of the tongue in various functional configurations. (A) The bimetal model in the initial configuration. (B) The final configuration of the model (sagittal bending) in the case of longitudinalis only contraction, and (C) The final configuration (sagittal bending) for the case of synergistic longitudinalis and transversus muscle contraction. Beam deflection was tracked by visualizing the deflection of 75 points defining the convex, concave, and interfacial contours. The results demonstrate that the initially concave down bent beam was effectively straightened by longitudinalis muscle contraction, and achieved its maximal sagittal bending configuration with the aid of transversus muscle contraction.

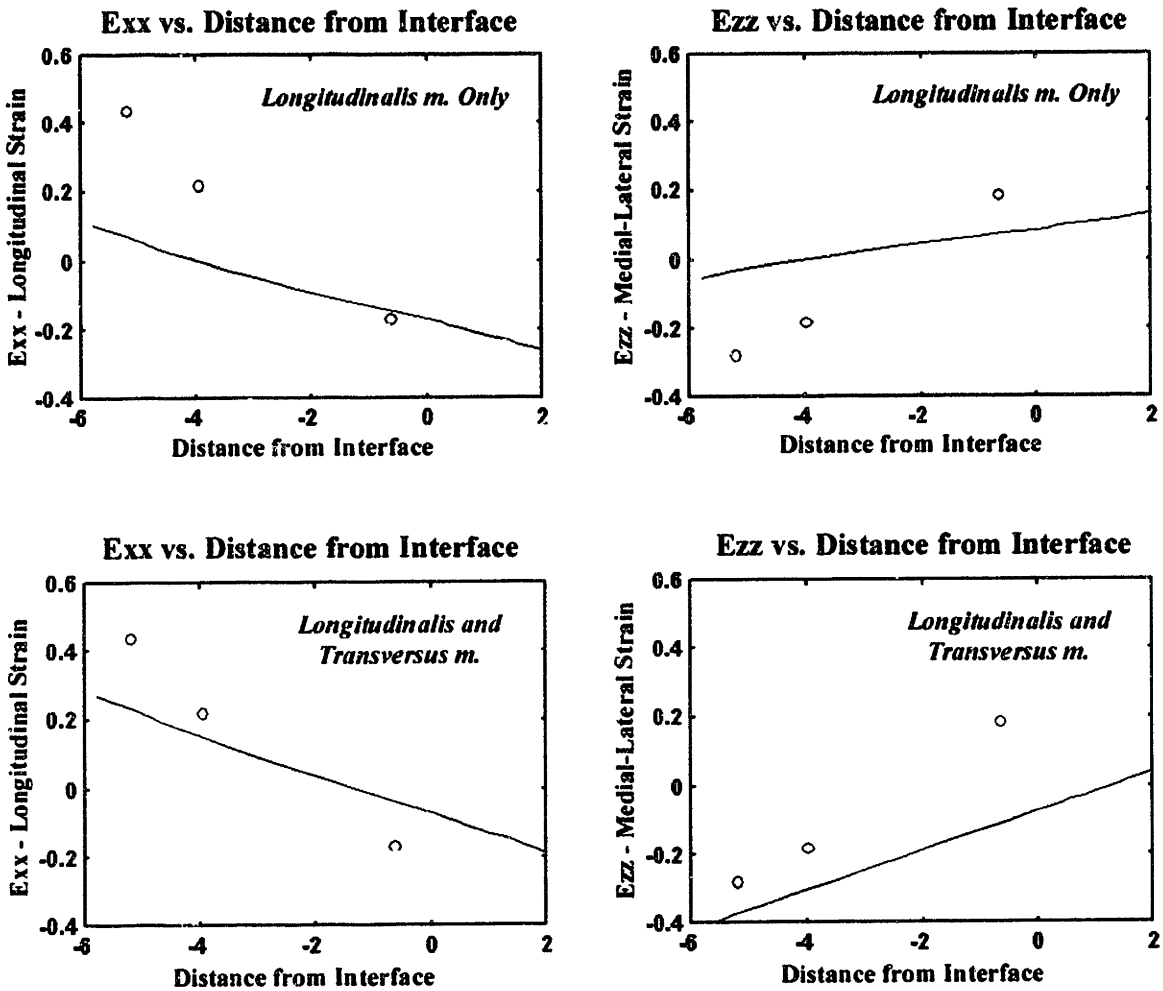

Figure 4-6 Modeled strain data were computed and graphed as a curvilinear line with regard to location along the tongue cross-section. The empirical (Tagging MRI derived) data points were plotted as circles on the same graph for comparison purpose. For the longitudinalis muscle only contraction scenario, theoretical longitudinal strains (E_{xx}) ranged from -0.26 at the superior edge of the longitudinalis muscle layer (most negative) to 0.10 at the inferior edge of the transversus/verticalis muscle layer. Medial-lateral (or through-plane) strains (E_{zz}) ranged from 0.13 at the superior edge of the longitudinalis muscle layer to -0.05 at the inferior edge of the transversus/verticalis muscle layer. For the longitudinalis and transversus muscle contraction scenario, theoretical longitudinal strains (E_{xx}) ranged from -0.19 at the superior edge of the longitudinalis muscle layer to 0.27 at the inferior edge of the transversus/verticalis muscle layer. Medial-lateral (or through-plane) strains (E_{zz}) ranged from 0.04 at the superior edge of the longitudinalis muscle layer to -0.41 at the inferior edge of the transversus/verticalis muscle layer. This synergistic scenario compared more favorably to the empirical (Tagging MRI derived) data which found that longitudinal strain was contractile (-0.17) at a location close to the interface of the longitudinalis muscle layer and transversus/verticalis muscle layer, and was extensile (0.44) near the inferior edge of the transversus/verticalis muscle layer.

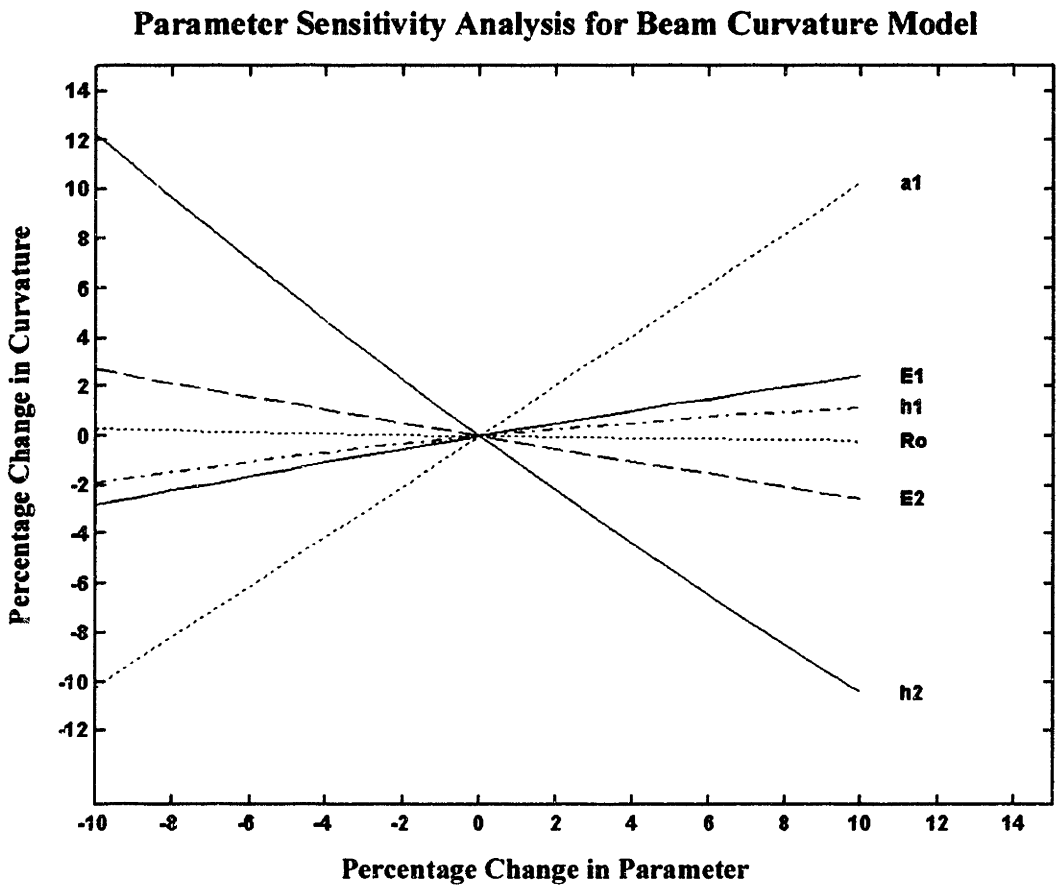

Figure 4-7 Sensitivity analysis of the equations involved in the model was completed by finding the effect induced on the computed curvature by varying a given model parameter. Model parameters were varied by +/- 10% and percentage effect on curvature was computed throughout. This analysis showed that curvature was most sensitive to α_1, the thermal expansion coefficient of beam 1 (the beam containing the superior longitudinalis muscle), and h_2, the height of beam 2 (the beam containing the transversus and verticalis muscles). The curvature was less sensitive to E_1, the Young's modulus of beam 1, E_2, the Young's modulus of beam 2, and h_1, the height of beam 1. The curvature was very minimally sensitive to R_o, the initial curvature of the strip. These results provide insight into which parameters contribute most to model error, and hence should be derived with greatest precision. Furthermore, these results can also be extrapolated to derive insight into which parameters may be used by the tongue to most efficiently modulate its range of motion.

4.3 Discussion: Modeling Sagittal TongueBending

The human tongue is a structurally heterogeneous and extremely flexible organ with a seemingly infinite number of degrees of freedom. In this modeling effort, our purpose was to gain insight into the mechanisms of a single, fundamental deformation, sagittal tongue bending. A better understanding of this basic maneuver could lead to a better understanding of some of the more complex deformations associated with human speech and swallowing.

4.3.1 Model Results and Validation

We explored two contraction scenarios to see which best approximates actual tongue bending (as determined by tagging MRI). Both the "superior longitudinalis muscle only" contraction scenario, and the synergistic "longitudinalis and transversus muscle" contraction scenario produced a change in curvature wherein the tongue switched conformation from concave down to concave up. However, in order for the tongue tip to achieve the strain pattern and curvature associated with a fully bent configuration, approximating the hard palate (as shown by tagging MRI, **Figure 4-8**), co-contraction of the superior longitudinalis and transversus muscles was necessary (**Table 4-3**).

Longitudinalis muscle contraction alone was sufficient to cause tongue straightening, an action important for anterior protrusion. However, our results demonstrated that in order for the tongue to achieve the more extreme sagittal curvature associated with hard palate contact, maximal efforts from both the longitudinalis and transversus myofiber populations were necessary. Examination of the cross-sectional strain field revealed that the anterior tongue experiences large longitudinal tensile strains, E_{xx}, in the range of 44% at the inferior border of the transversus muscle layer. These strains were not well approximated by contraction of the longitudinalis muscle alone. In contrast, the strain values predicted by synergistic contraction of the muscle layers more closely approximated the experimental values for strain and curvature. It was notable, however, that even

Figure 4-8 Tagging MRI for sagittal tongue bending

the synergistic strain values shown by the model underestimated actual longitudinal strain. We speculate that the larger longitudinal strain values seen in the empirical data may very well have been exaggerated by secondary effects, such as verticalis muscle co-contraction, which, while not augmenting global curvature, would produce greater tensile longitudinal strain. Such secondary effects were not accounted for in the current model.

Our data also demonstrated that the large contractile medial-lateral (through-plane) strains, E_{zz}, measured from the tagging MRI data were not adequately modeled by the contraction of the longitudinalis muscle alone. Medial-lateral contraction occurred only through Poisson's effects for this scenario, and produced the anticlastic curvature. However, under the synergistic contraction scenario, medial-lateral contraction (especially in the transversus/verticalis muscle layer) occurred primarily due to active contraction of the transversus musculature. The model produced contractile strains which overestimated slightly the actual contractile deformation. This may have resulted from the model assumption that the entire transversus muscle layer contracts uniformly. In reality, contraction is most likely modulated such that the superior portion of this layer contracts less than the inferior portion. This would maximize the curvature producing effects of muscle contraction. Since the height of this layer is significantly greater than the longitudinalis muscle layer (5.8mm compared to 2.0mm), not accounting for gradations in transversus muscle contraction could have produced this overestimate in medial-lateral contraction strain, as well as the underestimation in tensile strain in the longitudinalis muscle layer.

4.3.2 Model Assumptions and Derivations

In order to gain a better understanding of which parameters have greatest influence on tissue deformation, the analog model was dissected along its governing equations. This was important as the various parameters employed by the model had different degrees of measurement error. Our sensitivity study was accomplished by varying several key parameters by +/-10% and measuring the percentage effect propagated to the ultimate calculation of curvature (**Figure 4-7**). Due to the non-linear nature of the equations involved in the model, the sensitivity study was done graphically, since the calculation of partial derivatives with respect to various parameters would offer only infinitesimal sensitivity about the mean values. This study demonstrated that the model was most sensitive to α_1, the thermal expansion coefficient, and to h_2, the height of the transversus/verticalis muscle layer. A +10% change in α_1 resulted in a +10.3% change in curvature, k_b; while a -10% change in α_1 resulting in a -10.2% change in k_b. Conversely, a +10% change in h_2 resulted in a -10.4% change in k_b; while a -10% change

in h_2 resulting in a +12.2% change in k_b. Hence, even though the model was composed of many nested non-linear equations, the relationship of the curvature to the model's most influential parameters was close to linear with unity slope, within a physiologically reasonable range of variation. Furthermore, there was not a single parameter to which the curvature showed hypersensitivity ($k \propto |cx|^n$; $n \geq 2$), underscoring the stability of the model within a physiological range. The model proved to be less sensitive to the Young's modulus (E_1 or E_2), and to h_1, the height of the longitudinalis muscle layer. The height of layer 1 was less influential than the height of layer 2 because percentage changes of a significantly smaller value (h_1 = 2mm; h_2 = 5.8mm) translate to a smaller variability in composite beam height, h (a summed parameter important for ultimate curvature change). Finally, the model was almost completely insensitive to the initial curvature of the resting tongue (variability of k_b was less than 0.2% for a 10% change in R_o). This variable had a greater effect on the calculated *final* curvature through equation (4.8).

While the analog model adequately approximated sagittal tongue bending, offering insight into the contractions involved, there were several assumptions adopted during the modeling effort which need discussion. In regard to model development, the assumption that planar sections remain planar, i.e. that there was no shear deformation, reflected our idealization of sagittal bending. In actuality, MRI data (Napadow, Chen et al., 1999) showed that postero-inferior muscular attachments of the anterior tongue constrain the bending deformation, leading to the development of finite shear strains (**Figure 3-13**). Because this shear strain was external in nature, and did not arise directly from intrinsic muscular contraction, it was neglected in the model. Future iterations of this model could incorporate various boundary conditions (such as the postero-inferior attachment of the genioglossus muscle) and shear accommodating Timoshenko beams, rather than Bernoulli-Euler beams. Another assumption made in the development of the model was that the synergistic effects of longitudinalis and transversus muscle contraction could be combined by the theory of superposition (Crandall, 1959). This theory states that strains arising from various multi-dimensional stresses can be combined by summation as long as the constitutive relations are in a linearly elastic range. Hence, in order to explore synergistic effects in this modeling effort it was important to model the constitutive properties of the bimetal strip with isotropic linear elastic definitions. Since our model was static (bimodal - either deformed or undeformed) and did not include dynamic behavior (viscoelasticity, calcium homeostasis, dependence of stretch reflex on shortening speed, or reflex delays), we felt that this assumption was adequate. Moreover, this assumption was also made in several previous lingual modeling efforts (Kiritani, Miyawaki et al., 1976; Kakita and Fujimura, 1977; Hashimoto and Suga, 1986; Sanguineti, Laboissiere et al., 1997).

Regarding the definition of model parameters, data derived from MRI (such as b, L, h, k_o) were deemed sufficiently robust, as all were derived from the same subject. On the other hand, the longitudinalis and transversus cross-sectional composition percentage values were taken from the online Visible Human database, and thus were likely to have a higher degree of measurement and applicability error, as they came from an unrelated cadaver. Nonetheless, it is a fair assumption that the relative myofiber composition is stable within a species, especially for gender-matched individuals. Finally, it should be noted that the contraction scenarios studied involved maximal muscular contractions. In reality, maximal tetanic tension is rarely reached in a physiologic system. This assumption was considered appropriate for our scenarios due to the fact that the deformation studied was a relatively extreme motion, and maximal muscular effort would have been approached.

One of the most significant insights derived from the current modeling study was the paramount role muscular synergy played in creating tissue deformation. For example, during anterior protrusion (a highly functional, if sometimes culturally offensive, act), the transversus, verticalis, and even the extrinsic genioglossus muscle play active contractile roles (Sanguineti, Laboissiere et al., 1997; Napadow, Chen et al., 1999). In light of our modeling results, we hypothesize that the superior longitudinalis muscle also acts in concert with the above muscle groups to straighten the tongue from its resting bent configuration. Though subtle, this action is nevertheless functionally important, and illustrates the physiological reliance of synergistic muscular synchrony in the regulation of tissue deformation. This phenomenon further supports the concept of the tongue as a muscular hydrostat. Another example of the synergistic interplay of the tongue's muscular elements is the retrograde thrusting of the posterior tongue during the bolus propulsion stage of the swallow. This maneuver is important in clearing the bolus from the oral cavity into the oropharynx. Previous investigations found that bolus propulsion results from synergistic contraction of the posterior transversus muscle, as well as by external traction from the styloglossus muscle (Napadow, Chen et al., 1999). Conceivably, such redundancies are important to assure physiological success, even if one of the contractile elements becomes dysfunctional due to disease or trauma. As in other biomechanical manipulator systems in nature, synergistic muscular contractions augment physiological motion and add support and rigidity to the system. From a teleological perspective, muscular synergy may represent a necessary adaptation for life-sustaining functions, such as feeding, control of the respiratory tract, and communication.

Chapter 5

5 Conclusions and Future Directions

5.1 A Summary of Thesis Conclusions

The goal of this thesis was to highlight and expound upon the structure-function relationships of the human tongue. To this end, we have quantitatively explored lingual contraction patterns as well as the myoarchitecture that produces them. Specifically, we adapted a diffusion sensitive Magnetic Resonance Imaging technique to explore *in vivo* the myofiber orientations of the lingual musculature. Diffusion Tensor Imaging was adapted to provide adequate spatial resolution to image the human tongue. Furthermore, we tested the limits of this technique by comparing our MRI results to those of a three-dimensional microscopic investigation. Our results demonstrated that regions with variability in fiber orientation existed throughout the tongue. However, the interwoven intrinsic core region, where the interdigitating fibers confound experimental attempts to quantify lingual myoarchitecture, epitomized this heterogeneity. While difficult to image, heterogeneity does provide the tongue with a versatility in deformation not seen in any other organ in the human body. In this thesis, we also adapted an imaging technique to explore the internal deformation patterns exhibited by the tongue during various physiological tasks, including swallowing. Tagging MRI was used to quantify lingual strain, thereby inferring the degree of synergistic co-contraction that we hypothesized was responsible for lingual deformations such as swallowing, anterior protrusion, and lateral/sagittal bending. Finally, this thesis presented a biomechanical analog model of sagittal tongue bending, which developed the characterization of the tongue as a muscular hydrostat. This description defined the tongue as an organ whose musculature was organized and activated to produce tissue contraction and concomitant tissue expansion patterns, balanced for overall physiological effect.

In order to summarize the results of our physiological analysis of lingual musculature, I have provided a succinct tabular compendium of the various intrinsic and extrinsic muscles and their role in the deformations studied in this thesis (**Table 5-1**).

		Basic Lingual Deformations			**Oral Stage Deglutition**		
		Anterior Protrusion	**Sagittal Bending**	**Lateral Bending**	**Early Accommodation**	**Late Accommodation**	**Propulsion**
Intrinsic Musculature	**Superior Longitudinalis**		bilateral contraction	ipsilateral contraction	helps place tongue tip behind upper incisors (sagittal bending)		
	Inferior Longitudinalis			ipsilateral contraction			
	Transversus	bilateral contraction	augments bending, provides support		helps push tongue tip behind upper incisors		posterior fibers - helps propel bolus into pharynx
	Verticalis	bilateral contraction		augments bending, provides support	anterior fibers - forms grooved depression	posterior fibers - aids genioglossus	
Extrinsic Musculature	**Genioglossus**	aids by pulling the tongue base forward			anterior fibers - forms grooved depression	posterior fibers - transfers bolus retrograde	
	Hyoglossus				aids in forming the grooved depression	aids in depressing posterior tongue	
	Styloglossus			ipsilateral contraction - aids longitudinalis			primary effector of retrograde tissue motion
	Palatoglossus						aids styloglossus and transversus

Table 5-1 This table summarizes lingual fiber involvement for the various tongue deformations studied in this thesis. Evidence is provided from strain maps derived with Tagging MRI. Some muscles constitute the role of primary effector for a given deformation, while others offer supplementary assistance, or simply provide structural support. These different roles define the tongue as a muscular hydrostat. More detailed explanations can be found in Chapter 3.

It is clear that no one muscle produces a given deformation. There are always prime movers, antagonists and synergists, just as in any musculoskeletal joint system.

The characterization of the tongue as a muscular hydrostat warrants some more consideration. The first structure-function description of the tongue as a muscular hydrostat was in 1985 by Kier and Smith (Kier and Smith, 1985). In their work, the authors compared the tongue to other free standing muscular organs such as elephant trunks and squid tentacles – all of which capitalize on their tissue incompressibility to provide skeletal support in deformation. The common morphology in these seemingly disparate organs was the coexistence of muscular populations perpendicular (transverse, vertical, circumferential, or radial) and parallel (longitudinal) to the organ's long axis. As corroborated by our work, "perpendicular" muscles produce protrusion and provide skeletal support, while "parallel" muscles produce retraction and bending. In addition, the placement of longitudinal muscle fibers relative to the central axis, reflects their purpose. If the primary function of the longitudinal fibers is to produce retraction, these muscles are located along the central axis of the organ – as seen in certain reptilian tongues (e.g. *Varanus exanthematicus*, monitor lizard, and *Thamnophis*, garter snake). Certain mammals (e.g. *Manis*, pangolin[1]) also present with this morphology, though it is much more rare. However, if the longitudinal muscles are also to produce bending, their location is more peripheral in order to produce a greater moment about the bending axis. Furthermore, some muscular hydrostats (such as elephant trunks and certain lizard tongues, but not mammalian tongues) have muscular elements oriented helically about the organ's long axis, and perpendicular to one another. These fibers produce positive and negative torsion in the organ and are also located along the periphery to maximize bending moment.

The human tongue is a somewhat unique muscular hydrostat, as lingual myoarchitecture is organized into both intrinsic and extrinsic fibers. Thus, the contortions and undulations produced by the usual intrinsic components of a muscular hydrostat are augmented and modified by extrinsic muscular elements that tether the tongue to the surrounding skeletal structure. Historically, it was thought that extrinsic muscles alter tongue position, while intrinsic muscles alter tongue shape; a misconception that has, on occasion, persisted to present day (Agur and Lee, 1999). In fact, this thesis has demonstrated

[1] Within mammalia, the tongue length champion is *Manis*, the pangolin (scaly anteater). The intrinsic pangolin tongue extends back, posterior to the sternum, and down to an attachment on a specialized xiphoid cartilage. Notably, the extrinsic sternohyoid attaches to both the xiphoid process and caudally all the way to the right iliac fossa of the pelvis. Tongue length for *Manis gigantia*: 70cm; rather long for only a 120-140cm long body (Livingston, 1956; Doran and Allbrook, 1973)! The tongue's caudal cross-section is composed of longitudinal fibers surrounded by circular fibers (perpendicular to the long axis). The xiphoid plate is analogous to the hyoid bone in other mammals as it is an attachment for extrinsic muscles including the genioglossus and geniohyoid (protractor muscles) and sternohyoid (retractor muscle). The *Manis* hyoid bone is instead used by the tongue to scrape termites off of its sticky mucosa and into the esophagus.

that extrinsic and intrinsic muscles work in concert to produce both changes in tongue position and tongue shape[1]. For example, the extrinsic genioglossus merges with fibers of the intrinsic verticalis muscle, contributing to anterior protrusion and bolus accommodation in swallowing. During bolus propulsion, the extrinsic styloglossus muscle pulls the posterior tongue retrograde, working synergistically with the retrograde hydrostatic expansion produced by intrinsic transversus muscle contraction. Kier and Smith (1985) theorized that muscular hydrostats optimize speed and flexibility in deformation while sacrificing force production (typically maximized in non-hydrostatic systems by large moment arms about a bony skeleton supported joint). One may speculate that extrinsic muscles in the tongue serve to enhance the force production capabilities of the tongue's otherwise freestanding body. Extrinsic muscle contractions impose more gross deformations, analogous to "coarse tuning." For example, bolus propulsion during swallowing is a maneuver necessitating force and may depend more principally on extrinsic styloglossus contraction. Conversely, contractions of the intrinsic musculature may instead be likened to a "fine tuning" of the many diverse changes of lingual position and shape within the oral cavity.

5.2 Future Directions: Investigating Myoarchitecture in a Clinical Model

One obvious extension of the methodologies developed in this thesis would be to apply them to a disease model. The most common pathologies that produce dysphagia (and hence may result in abnormal lingual myoarchitecture) include myopathies (FSH, Becker's Muscular Dystrophy – BMD, Duchenne's Muscular Dystrophy – DMD), neuropathies (Parkinson's, Cerebral Vascular Accidents), and disorders of the neuromuscular junction (Myasthenia Gravis). It is hypothesized that the latter two may adversely alter lingual function by decreasing nervous stimulation (decreased nervous tone with CVA's and less available acetylcholine receptors with Myasthenia Gravis), thereby producing atrophic

[1] In a clinical setting, anterior tongue protrusion can localize hemispherical brain trauma due to CVA (stroke), as the tongue always deviates toward the effected side. Coincidentally, this finding is present with any unilateral paralysis of the tongue - such as with lower jaw anesthesia during dental procedures. As described by a classic experiment, Bennett and Hutchinson (1946) concluded that tongue tip deviation occurs from "(1) the forward pull of the genioglossus on the non-paralyzed side, (2) elongation of the tongue by intrinsic muscles on the non-paralyzed side, and (3) the weight or lag produced by the paralyzed half." The authors conducted hypoglossal nerve end-branch stimulation on whole and split canine tongues and demonstrated that the effect of the genioglossus on anterior protrusion was minimal compared to that of transversus and verticalis contraction (Bennett and Hutchinson, 1946).

change and decreased tongue mobility. Muscular dystrophy results from the abnormal production of the protein *dystrophin* (absent in Duchenne's, decreased in production and dysmorphic in Becker's), which has been localized to the I and M bands in myocytes and has been implicated in maintaining sarcolemmal membrane integrity during the shape change associated with muscular contraction. Histological changes associated with BMD and DMD include a variation in fiber diameter, necrosis and phagocytosis of myofibers, and the gradual replacement of contractile tissue with proliferating endomysial connective tissue (**Figure 5-1**).

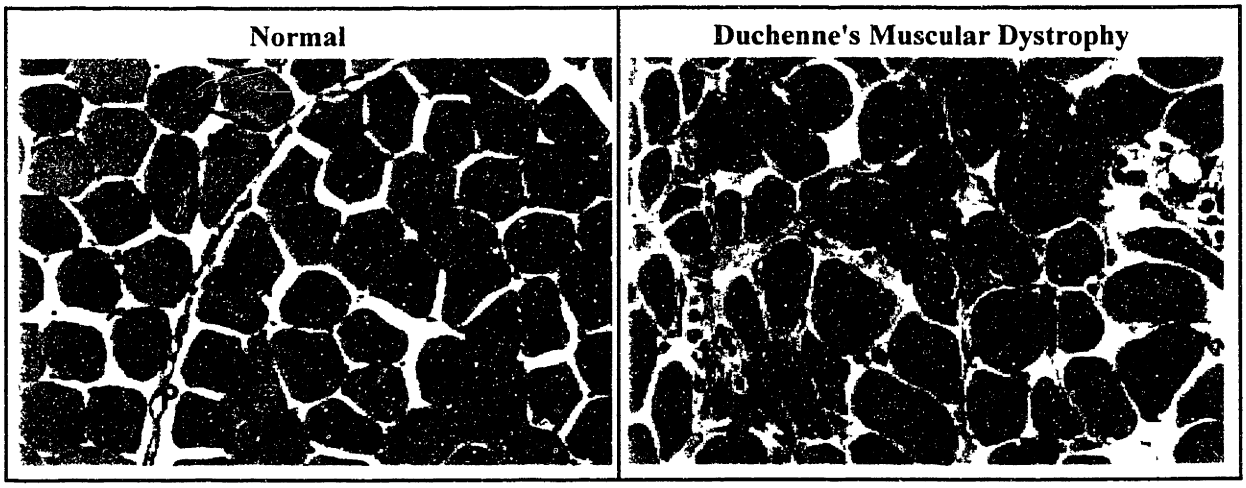

Figure 5-1 Cross sectional H&E histology of normal skeletal muscle (left) and that of a patient with Duchenne's Muscular Dystrophy (right) shows marked differences. Dystrophic muscle demonstrates inflammation, variations in fiber diameter, and fibrosis, resulting in an assumed alteration of molecular diffusion and diffusion tensor anisotropy. C: capillary; P: perimysium. (Images taken from pathology text (Cotran, Kumar et al., 1994))

Within the tongue (which is also composed of skeletal muscle), these changes produce an enlarged hypotonic organ (Kumada, Niitsu et al., 1992). Furthermore, all of these changes could have profound effects on DTI metrics, such as tensor anisotropy and trace. An enlarged organ composed of randomly oriented fibrous and edematous tissue should result in lower anisotropy than tissue with a higher composition of a prevalent fiber population. The changes impacting myofiber organization may also be visualized with 2-photon microscopy. For instance, pathology may produce intrinsic fiber populations (i.e. transversus and verticalis m.), which would now be oblique to the axial plane (normally they were found to be relatively orthogonal and in-plane) – a dysmorphic condition that could be both visualized and quantified by 2-photon microscopy.

5.3 *Diffusion Spectrum Imaging (DSI) of the Tongue*

While diffusion tensor imaging proved adequate in deciphering homogeneous fiber orientations, DTI could not fully resolve multiple intravoxel myofiber populations. An extension of the DTI technique, termed Diffusion Spectrum Imaging (DSI), samples the tissue voxel with greater resolution and hence shows promise in the characterization of structurally complex tissue (Wedeen, Reese et al., 2000).

The DSI technique is based on the same principles as DTI – namely that signal attenuation from magnetic field gradient refocusing is due primarily to diffusion displacement along the direction of magnetic gradient. However, the "spin" on the basic DTI technique with DSI is that the displacement profile at a given location can be determined directly by Fourier transforming the echo intensity against gradient strength at fixed gradient pulse spacing (Cory and Garroway, 1990). This can be accomplished in either a stimulated or spin echo experiment. More explicitly, the echo intensity, S(**g**), in such an experiment follows the equation:

$$S(\mathbf{g}) = \int \rho(\mathbf{r}_0) \int P(\mathbf{r}_0 \mid \mathbf{r}, t_d) \exp[i\gamma t_e \mathbf{g} \cdot (\mathbf{r} - \mathbf{r}_0)] d\mathbf{r} d\mathbf{r}_0 \tag{5.1}$$

where $\rho(\mathbf{r}_0)$ is the initial concentration as a function of the initial position, $\mathbf{r}_0$. $P(\mathbf{r}_0|\mathbf{r}, t_d)$ is the probability that a spin initially at $\mathbf{r}_0$ will move to $\mathbf{r}$ within time t_d. t_e is the encoding time. $\mathbf{g}$ is the magnetic field gradient strength, and γ is the gyromagnetic ratio. Direct Fourier transform of the echo intensity with respect to wavenumber, $\gamma t_e \mathbf{g}$ (with units μm^{-1}), yields the displacement profile, $I(\mathbf{x})$ along the known gradient direction, $\mathbf{x}$:

$$I(x) = \mathrm{FT}\{S(\mathbf{g})\}_{\gamma t_e \mathbf{g}} = \int \rho(\mathbf{r}_0) \int P(\mathbf{r}_0 \mid \mathbf{r}, t_d) \mathrm{FT}\{\exp[i\gamma t_e \mathbf{g} \cdot (\mathbf{r} - \mathbf{r}_0)]\}_{\gamma t_e \mathbf{g}} d\mathbf{r} d\mathbf{r}_0 \tag{5.2}$$

which approaches a delta function at $\mathbf{x} = \mathbf{r} - \mathbf{r}_0$, thus yielding

$$I(x) = \mathrm{FT}\{S(\mathbf{g})\}_{\gamma t_e \mathbf{g}} = \int \rho(\mathbf{r}_0) P(\mathbf{r}_0 \mid (\mathbf{r}_0 + x), t_d) d\mathbf{r}_0 \tag{5.3}$$

which is the convolution of the initial concentration with the conditional probability of relative displacement by $\mathbf{x}$. In preliminary experiments with DSI, the wavenumber was incremented by varying gradient strength, $\mathbf{g}$, while encoding time, t_e, was held constant (Wedeen, Reese et al., 2000). The

diffusion gradient sampling scheme consisted of a key-hole Cartesian acquisition to include q-space[1] values lying on a Cartesian grid (Δq=0.01μm^{-1}) within a sphere of radius q_{max}=0.1μm^{-1}, for a total of 500 sampling points. The above sampling scheme provided a diffusion spectrum resolution of $(q_{max})^{-1}$=5μm and a FOV $(\Delta q)^{-1}$=200μm.

The displacement profile could then be visualized by graphing 3D iso-contour icons for each voxel sampled. The iso-contours represented the displacement spectrum evaluated at a radius of 15μ, minus the minimum of the spectrum over all directions. Icon faces were color-coded based on orientation: longitudinal-red, vertical-green, and transverse-blue. Bulges along these icons represented probable fiber populations, since proton displacement by self-diffusion would be greatest along myofiber long axes.

This methodology represented an improvement on DTI since many voxels within the anterior core of the tongue were inhabited by multiple fiber populations. These populations were oriented in oblique directions to one another and their *relative* orientation could not be inferred from a single tensor. Whereas DTI used low anisotropy to suggest structural heterogeneity, it was limited to deriving only the plane of greatest angular dispersion (where the two myofiber populations lay). However, Diffusion Spectrum Imaging could potentially pinpoint the fiber orientations in both homogeneous and heterogeneous muscle regions.

Preliminary data were presented for an axial slice through the anterior *ex vivo* bovine tongue (**Figure 5-2**). The tissue sample was excised, treated, and handled similar to the DTI experiments. The data confirmed distinct fiber population heterogeneity in the anterior mammalian tongue. The longitudinal sheath was present on the periphery as a single through-plane fiber population (red). The tongue core exhibited both transversus (blue) and verticalis (green) myofiber populations. Inferior voxels again showed the existence of only a single fiber population – most likely the extrinsic genioglossus muscle (green) fanning superiorly into the tongue body. This clarity of data was not seen with DTI for voxels which contained multiple fiber populations. For the bovine tongue, these voxels were found in the intrinsic core region, where verticalis and transversus coexisted in serial sheets. Whereas DTI produced octahedra oriented along a direction representing a mixed average of the two populations, DSI was able to display both fiber populations independently in the same voxel.

[1] q-space is similar to k-space, where q is the wavenumber previously defined as $\gamma_e \mathbf{g}$

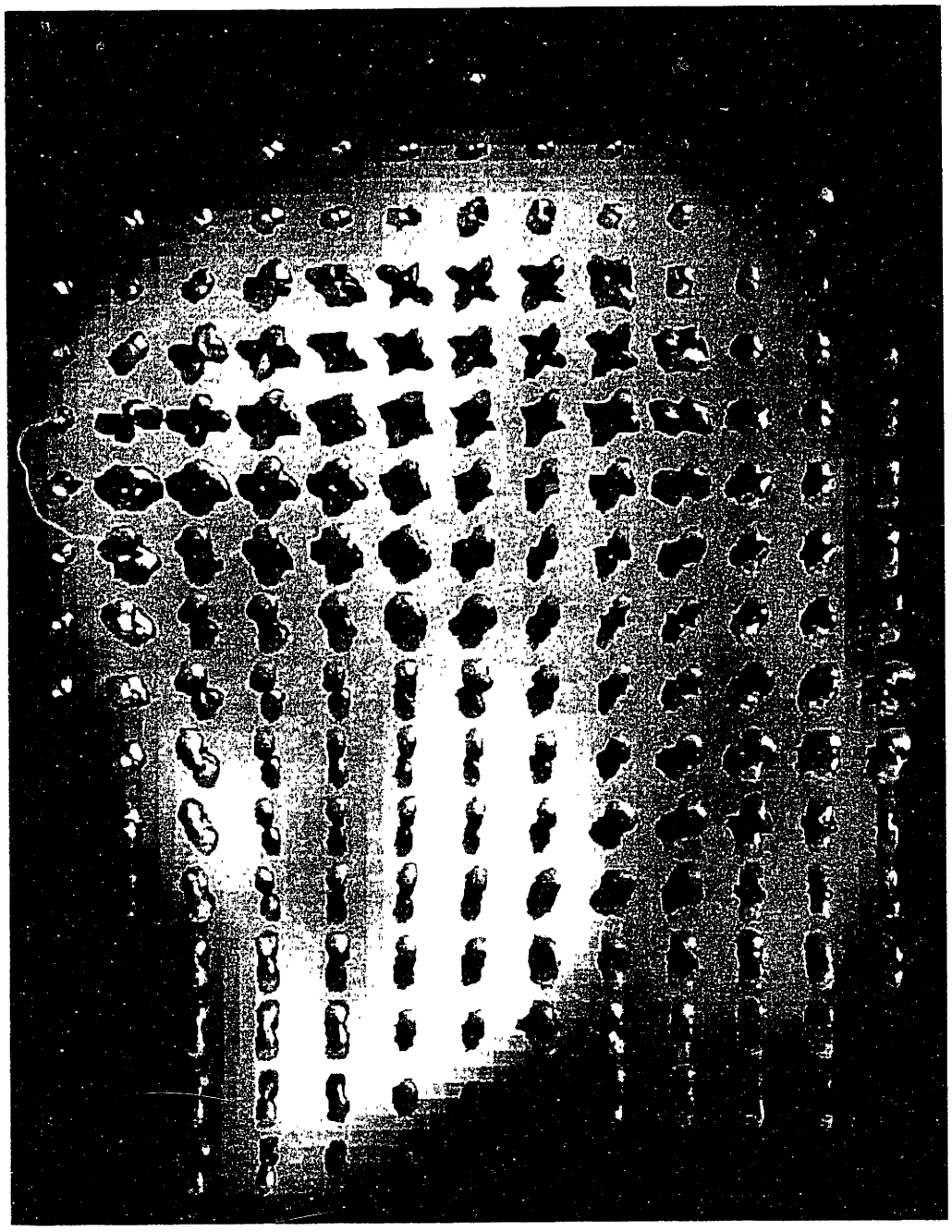

Figure 5-2 Diffusion Spectrum Imaging of an *ex vivo* bovine tongue (axial slice). The 3D displacement profile was visualized by iso-contour icons with orientation specific color-coding. This image shows distinct fiber population neterogeneity. The longitudinal sheath was present on the periphery as a single through-plane fiber population (red). The tongue core exhibited both transversus (blue) and verticalis (green) myofiber populations. Inferior voxels again showed the existence of only a single fiber population - most likely the extrinsic genioglossus muscle (green) fanning superiorly into the tongue body. *Image courtesy of Van Wedeen.*

An interesting application of the Diffusion Spectrum Imaging technique would be the investigation of normal or pathological myoarchitecture by varying parameters in the DSI pulse sequence that were held constant in the preliminary experiments. For instance, the wavenumber ($\gamma t_e \mathbf{g}$) appearing in the equation for signal intensity, S(**g**) (equation **(5.1)**), was incremented by varying gradient strength, **g**, while encoding time, t_e, was held constant. This experiment could also be repeated at varying diffusion times, t_e, to see how the displacement probability varies. This may be interesting since restricted diffusion ("impermeable" boundaries) manifests itself by the independence of S(**g**) on t_e, at a t_e large enough such that the diffusion distance equals the mean free path of cell diameter. Myopathies such as DMD and other atrophic changes would alter fiber diameter and hence the mean free path. Thus, DSI could be used to track the progression of myopathic disease.

5.4 Future Directions: Investigating Physiology and Pathophysiology

In our previous work, we have demonstrated not only the feasibility but also the utility of tagging MRI to evaluate the strain field of a complex deforming tissue. Another extension of this thesis would be to compile a 3D strain field rendering of the entire tongue during deglutition. Our results from the mid-sagittal slice were very promising, but it is my suspicion that the para-sagittal slices also contain interesting information and may be crucial in the diagnosis of incompetent bolus containment in certain oropharyngeal dysphagias. Parasagittal slices could be referenced to other parasagittal slices, as well as the midsagittal slice, by matching deglutitive phase observed by tongue contour. Then, the entire dataset could be compiled into a volumetric strain map movie, displaying the changing 3D strain field throughout oral phase deglutition.

Another obvious extension of the tagging methodology would be for the evaluation of pathological deglutition. Similar clinical models can be evaluated as in the myoarchitecture study – namely hemiplegic CVA, muscular dystrophy, etc. Atrophy of skeletal muscle tissue (whether primary in MD or secondary in CVA), will surely limit the deformation of the tongue, eventually producing significant morbidity via dysphagia. Strain mapping lingual pathology (most likely with the already proven mid-sagittal tagging sequence) could be correlated with existing metrics of deglutition such as bolus transport time and manometry data in order to derive the relevance of tongue dysfunction to various oropharyngeal dysphagias.

5.5 *Future Directions: Associating Local Strain with Local Fiber Orientation*

The association of regional strain with local fiber organization, i.e. fiber direction or diffusion anisotropy, would provide direct demonstration of structure-function relationship. Since it is presently not feasible to impart DTI or DSI during ungated physiological motion, the pulse sequences must be improved upon or, the motion studied must be gated. If either of these options proved feasible, it would then be possible to superimpose the strain tensor field (acquired during physiological motion) onto architectural data from *in vivo* diffusion tensor or diffusion spectrum imaging in the same subject. Specifically, the strain tensor must be rotated into the eigensystem of the diffusion tensor, such that the strains measured are in the principal directions of the described fibers. However, this methodology would apply to homogeneous tissue regions only. The strain tensor would have to be rotated into multiple fiber orientations, as derived by DSI, if the tissue region proved significantly heterogeneous (common throughout the tongue). This would provide a quantification of "fiber strains," that is the degree of axial strain experienced by the constituent myofibers. Furthermore, the calculation of the axial strain experienced along the secondary eigenvector of the DTI diffusion tensor (i.e. in-plane to the sampled fiber bundle but orthogonal to its constituent myofibers) would allow for the quantification of "bundle strains." The transformation of the strain tensor could be calculated as follows:

$$\mathbf{E}' = \mathbf{Q}\mathbf{E}\mathbf{Q}^{T} \tag{5.4}$$

Where $\mathbf{E}$ is the strain tensor in the laboratory x-y-z coordinate system, $\mathbf{E}'$ is the strain tensor in the eigen-system of the location specific diffusion tensor and $\mathbf{Q}$ is a transformation matrix of the column-wise eigenvectors of the diffusion tensor (^{T} being the transpose operation). Hence, if $\{Q_{11}, Q_{21}, Q_{31}\}$ is the primary eigenvector $\mathbf{e}_1$ of the diffusion tensor, corresponding to the homogeneous myofiber direction, then $\mathbf{E}'_{11}$ is the relevant axial strain experienced by the fiber population in the voxel in question. Similarly $\mathbf{E}'_{22}$ is the relevant "bundle strain."

5.6 *Future Directions: The Effect of Variable Bolus Parameters onStrain*

An important consideration in our past studies was that deglutitive strain was measured for dry swallows, i.e. negligible bolus volume. The lingual response to the bolus in the oral cavity constitutes a crucial self-regulator of the tongue's mechanical function. Since the selection of food in humans is based on factors such as taste, smell, and social reinforcement, rather than pre-selected mechanical attributes, the tongue is required to adapt instantaneously to variations of bolus volume and viscosity. Previous work has emphasized that in response to variation of bolus volume or viscosity, the tongue is capable of rapidly reconfiguring its shape, as well as modifying the timing of physiological events, such as bolus manipulation and laryngeal closure (Dantas, Kern et al., 1990). Hence, strain mapping with Tagging MRI could be used to ascertain the underlying mechanical basis for changes in lingual configuration. Moreover, swallowing is produced for the express purpose of ingesting a *bolus* of food or drink, while dysphagia is rarely problematic when no bolus is present. Hence, the results expressed in this thesis should somehow be extended to incorporate variable bolus conditions.

Both increased volume and viscosity could induce changes in intrinsic core contraction and extrinsic contraction of either the inferior directed (resulting in deepened accommodation) or medial-laterally and postero-superiorly directed (resulting in enhanced propulsion) muscles. For example, these changes in bolus properties could produce a graded increase of contractile strain encircling the bolus – corresponding to activation of the genioglossus and hyoglossus muscles. The net effect of these actions would be to enlarge the accommodating concavity to effectively contain the bolus on the surface of the tongue prior to propulsion.

A major technical problem would be to quantify strain relative to a rest configuration. Since our methodology imposes a square rectilinear tagging grid almost immediately before imaging, the grid would have to be placed with the subject holding the bolus in their mouth. Thus, the tongue is not tagged in a rest state! A correction would have to be made to transform the measured strain map into a strain field relative to a true rest state, so that fiber contraction patterns could be inferred.

While difficult, this correction could be completed by deriving the strain state at the intermediate conformation (most likely early accommodation, as the bolus is held in place). If a linear element in the rest conformation (dx) is transformed by the deformation gradient $\underline{\mathbf{F}}$ in early accommodation to dy,

$$dy = \underline{F}\, dx \tag{5.5}$$

and is then transformed by a different deformation gradient $\underline{\mathbf{G}}$ into dz,

$$dz = \underline{G}\, dy \tag{5.6}$$

then the line element which can be quantified from the gated tagged image (dz) is in fact related to the rest condition by the multiplicative quantity $\underline{GF}$,

$$dz = \underline{GF}\, dx \tag{5.7}$$

Hence, $\underline{F}$ corresponds to a deformation into the intermediate conformation of early accommodation, and could be quantified by a tagging experiment wherein a bolus is quickly injected into the oral cavity and imaged in early accommodation. In fact, this was done by our group with the use of a 10ml syringe (unpublished data). Then, $\underline{G}$ could be derived in a separate experiment starting from early accommodation, with bolus in place, by producing a tagged image at the chosen time step. However, several difficulties would still remain. For example, it would be difficult for the subject to assume the same early accommodative deformation with each bolus swallow. Also, co-registration of the different strain fields could prove to be problematic. This said, there would be a significant payoff in successfully performing these experiments. Specifically, the results would produce a complete 3-dimensional strain map for the entire tongue, for any phase of oral deglutition.

Publications Derived from Thesis

1. Napadow V.J., Q. Chen, V.J. Wedeen, R.J. Gilbert. Intramural mechanics of the human tongue in association with physiological deformations. (1999) **Journal of Biomechanics,** 32 (1): pp. 1-12.

2. Napadow V.J., Q. Chen, V.J. Wedeen, R.J. Gilbert, Biomechanical basis for lingual muscular deformation during swallowing. (1999) **American Journal of Physiology,** 40 (3): pp. G695-G701.

3. Wedeen V.J., T.G. Reese, V.J. Napadow, R.J. Gilbert. Demonstration of primary and secondary muscle fiber architecture of the Bovine tongue by diffusion tensor MRI. (2001) **Biophysical Journal,** 80(2): pp.1024-1028.

4. Napadow V.J., Q. Chen, V. Mai, PTC So, R.J. Gilbert. Quantitative analysis of 3D-resolved fiber architecture in heterogeneous skeletal muscle tissue using NMR and optical imaging methods. (2001) **Biophysical Journal,** 80: pp. 2968-2975.

5. Chen Q., V. Mai, A.A. Bankier, V.J. Napadow, R.J. Gilbert, R.R. Edelman. An ultra-fast MR grid tagging sequence for assessment of local mechanical properties of the lungs. (2001) **Magnetic Resonance in Medicine,** 45(1): pp.24-8.

6. Napadow V.J., V. Mai, A.A. Bankier, R.J. Gilbert, R. Edelman, Q. Chen. Determination of regional pulmonary parenchymal strain during normal respiration using spin inversion tagged magnetization MRI. (2001) **Journal of Magnetic Resonance Imaging,** 13(3): pp.467-74.

7. Napadow, V., R Kamm, R. Gilbert. A biomechanical model of sagittal tongue bending. **Journal of Biomechanical Engineering,** in review.

Appendix A:

Introduction to Magnetic Resonance Imaging

Nuclear Magnetic Resonance (NMR) or Magnetic Resonance Imaging (MRI - the nomenclature employed in the clinical medicine world to avoid the connotations of "nuclear" in NMR), was an integral imaging modality employed in this study. This brief introduction into MRI is not intended to be an all-encompassing discourse of the technology's classical or quantum mechanics phenomena; however, some background is in order and will be provided.

MRI employs energy in the radio frequency (RF) band of the electromagnetic spectrum; coupled with static magnetic fields with strengths on the order of a Tesla (the magnet used was a 1.5T Siemens Vision or GE Signa System). 1 Tesla equals 10^4 Gauss, and, for reference, the Earth's natural magnetic field is approximately 0.5 Gauss in strength. The magnetic resonance phenomenon exists only for nuclei with non-zero spin quantum numbers, I, which denotes an odd number of protons or neutrons. Hydrogen, ^1H, satisfies this condition, having a spin quantum number equal to ½. Furthermore, this element is ubiquitous in the human body, which is composed mainly (70%) of water, H_2O, thus providing ample resource to study this phenomenon. Due to its non-zero spin quantum number, hydrogen has an induced nuclear magnetic moment,

$$\mu = \gamma_H \hbar I \tag{A.1}$$

where $\gamma_H = 42.6$MHz/T is the proton (^1H) gyromagnetic ratio and $\hbar$ is Plank's constant. The proton acts as a magnetic dipole, alternating between its positive and negative spin states. In the presence of an external magnetic field, B_0, ^1H experiences an interaction energy given by

$$E = \vec{\mu} \bullet \vec{B}_0 \tag{A.2}$$

For I = ½ nuclei, there exist two allowable states for the magnetic moment to align with the external magnetic field, parallel and anti-parallel. The interaction energy increases with the strength of the external field, as does the energy difference, ΔE, between the parallel and anti-parallel aligned dipoles (**Figure A-1**).

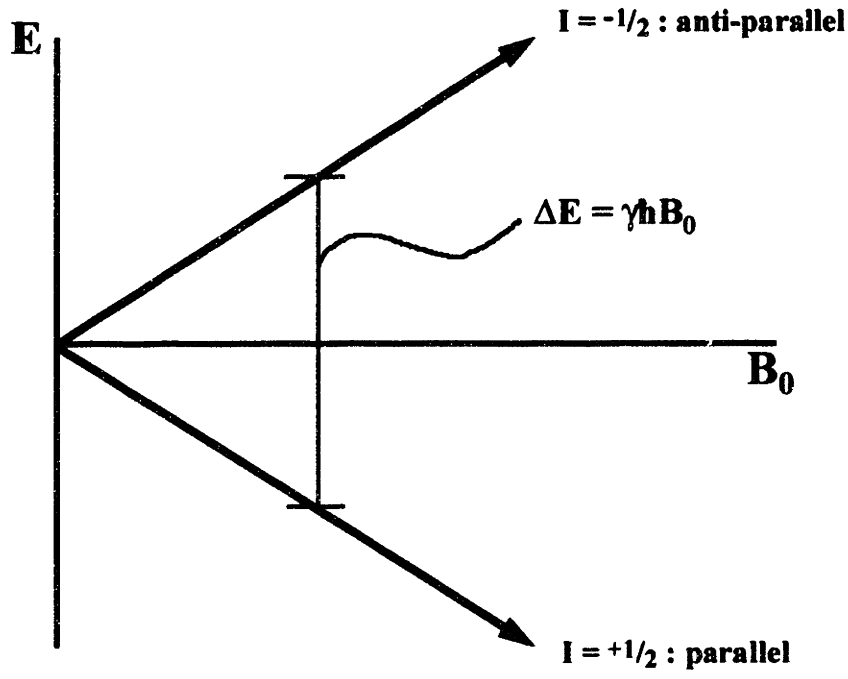

Figure A-1 Energy associated with the interaction of the proton magnetic dipole and an external magnetic field. There are two allowable states for the dipole, parallel and anti-parallel with B_0.

Spins prefer the lower energy state, and so will tend to align parallel with the external field. Statistically speaking, the ratio of spins aligning anti-parallel to those aligning parallel follows the Boltzmann distribution, given by

$$\frac{N_-}{N_+} = \exp\left(-\frac{\Delta E}{kT}\right) \tag{A.3}$$

where k is the Boltzmann constant and T is temperature. This spin population difference is what leads to the NMR signal.

For an observable signal to exist, there must be 10^{18} more spins aligned parallel than anti-parallel to B_0. At room temperature and at a field strength of 1.5T, the number of excess spins (parallel spins not paired with a neighboring anti-parallel spin) is only 1 in 10^5. However, in only 1ml of H_20, there are $6.7x10^{22}$ spins. Even the miniscule ratio of $1:10^5$ leads to $6.7x10^{17}$ excess parallel spins in only 1 ml of H_20. This plethora of spins provides ample signal for an NMR experiment on human tissue, which is by nature aqueous.

All of the magnetic dipoles can be represented by a single bulk sum magnetization vector,

$$\vec{M} = \sum \vec{\mu} \tag{A.4}$$

which traverses the space represented by a cone standing on end. The cone's long axis represents the external magnetic field, B_0, and the magnetization vector precesses about this axis (thus producing the cone). The Precession rate is given by the Larmor frequency,

$$\omega_0 = \gamma_H B_0 \tag{A.5}$$

In order to perform NMR experiments, energy must be input at or near the proton's Larmor frequency, ω_0. This restriction means that at 1.5T, RF energy must be input. This is because the Larmor frequency of hydrogen at this field strength is 63.9MHz, close to the FM RF band, which stretches on typical radio dials from 88 to 108 MHz.

In a reference frame rotating with the Larmor frequency about the B_0 axis (z-axis), the bulk magnetization vector, M_0, is stationary, and aligned with the z-axis. Spin dynamics are then governed by the famous Bloch equations (Bloch, 1946), which in vector form are

$$\frac{\mathrm{d}}{\mathrm{dt}}\vec{M}(t) = \gamma_H \vec{M}(t) \times \vec{B} - \frac{1}{T_1}(M_z - M_0)\hat{z} - \frac{1}{T_2}\left(M_x\hat{x} - M_y\hat{y}\right) \tag{A.6}$$

where M_z is amount of magnetization along the z-axis, and is termed longitudinal magnetization. M_x and M_y represent the amount of magnetization along the x and y axes respectively, and in vector sum are referred to as the transverse magnetization. Transverse magnetization is measured by the current it induces in an RF receive coil and corresponds directly to pixel intensity.

In a typical MRI experiment, short RF pulses (t=1ms) create a magnetic field, B_1, oscillating at the resonance (Larmor) frequency (that is, stationary in the rotating reference frame). This magnetic field tips the magnetization vector off of its equilibrium along the z-axis. Once this RF pulse has been turned off, the transverse magnetization relaxes back to nil exponentially at a rate given by a decay time constant T_2, which is an inherent property of the tissue. Simultaneously, the longitudinal magnetization relaxes back to its original value, M_0, with time constant T_1. Different tissues have different relaxation time constants, a property which provides for the contrast in a typical MR image.

Appendix B:

Introduction to 2-Photon Microscopy

Two-photon excitation microscopy was used to image lingual muscle fiber autofluorescence *in situ*. This imaging modality may constitute an optimal method for visualizing *in situ* fiber architecture due to its ability to scan a three-dimensional portion of the tissue space; thereby visualizing the relative orientations of heterogeneously aligned fiber populations. All two-photon scanning was done in the laboratory of Peter So, on the campus of the Massachusetts Institute of Technology.

Two-photon microscopy was developed as an extension of classical fluorescence based confocal microscopy. With classical fluorescence confocal microscopy (single photon), several limitations confound experimental design. Firstly, increased scattering of excitation and emission photons leads to image degradation. Secondly, photobleaching of fluorophores in planes outside those being observed can degrade subsequent imaging planes as the 3D sample is scanned. Thus, the smaller the excitation volume, the lower the chances of photobleaching occurring. Finally, confocal microscopy requires a blocking pinhole to generate an optical section.

To produce the two-photon effect, laser excitation was configured to excite *two* photons at discrete locations in the tissue (Denk, Strickler et al., 1990; Masters, So et al., 1997; Centonze and White, 1998). Energy is directly proportional to frequency, $E = h\nu$. Thus, at higher wavelength, energy is lower and it takes multiple simultaneous absorptions of the incident beam to excite a certain fluorophore, which would have fluoresced by absorbing a single lower-wavelength photon (**Figure B-2**). For example, autofluorescence of pyridine nucleotides, NAD(H) and NADP(H), occurs with excitation energy of $\lambda \sim 380$nm. Hence, to produce the two-photon effect, we would use energy of $\lambda \sim$ 790nm. But what advantages are there for scanning with higher wavelength energy? Firstly, scattering is highly wavelength dependent, being proportional to $\sim 1/\lambda^4$ (i.e. less for longer λ). Hence, scanning at higher wavelengths (as is achieved with two-photon microscopy for the same fluorophore species) will mitigate photon scattering. Another reason to scan with higher wavelength energy is that most biological tissue has an optical window within the infrared wavelength range, where scattering and absorption are limited (**Figure B-1**).

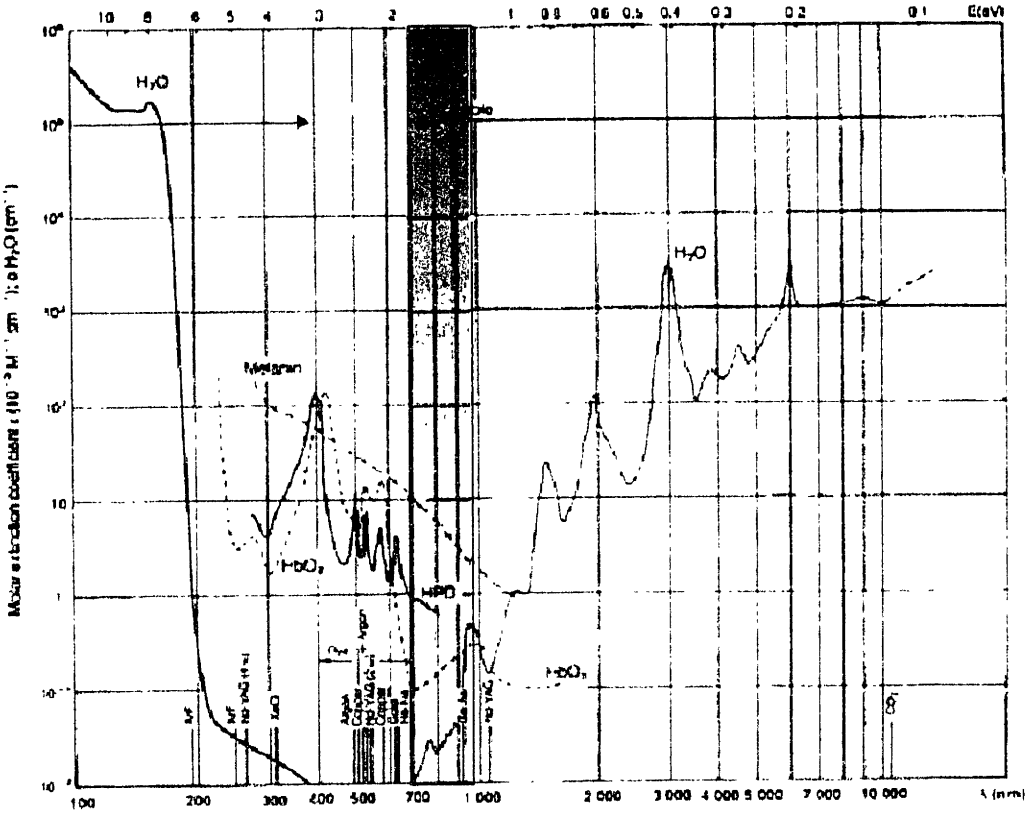

Figure B-1 An optical window occurs in the infrared range for many biological tissues. In this window, absorption and scattering are limited, thereby reducing background noise. Two-photon microscopy capitalizes on the existence of this window by utilizing energy within the infrared range to achieve fluorescence imaging.

However, multiphoton events are rare (2-photon excitation will drop off as inverse fourth power from plane of focus), thus a high energy beam is needed to provide adequate photon flux (15 mW at specimen). In order to avoid excessive average power consumption and energy deposition at the sample, the beam is pulsed (76 MHz, 150 fs (10^{-15}) pulsewidth). One advantage of this steep excitation falloff comes in depth discrimination. In two-photon microscopy, excitation is confined to a small enough volume (the football-shaped excitation volume psf: radial ~ 300 nm; axial ~ 1 μm) to effectively remove background signal and beam scatter, obviating the need for a blocking pinhole (**Figure B-2**). This higher SNR and efficiency translates into a depth of imaging penetration *twice* that of confocal (Centonze and White, 1998).

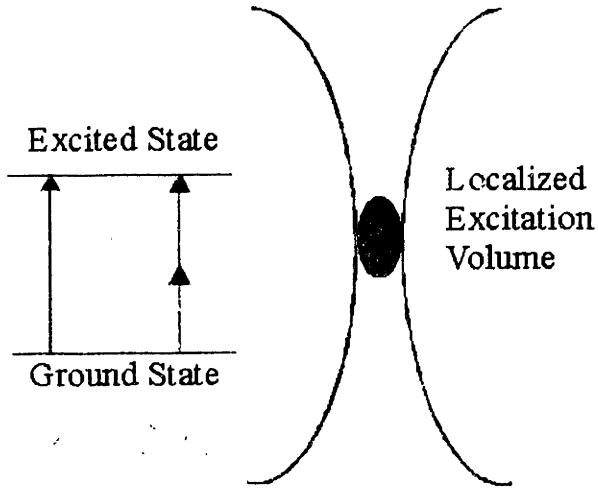

Figure B-2 The two-photon effect occurs when two lower energy (higher wavelength) photon excite a fluorophore that would have been naturally excited by a single higher energy (lower wavelength) photon. Two photon events are rare, thus excitation falls off rapidly from the laser focal point, which has the highest degree of photon flux.

An overview of the basic design of the multi-photon microscope is also warranted (Masters, So et al., 1997; So, Kim et al., 1998). Tissue specimens were imaged with a mode-locked Ti-Sapphire laser, with a 76MHz repetition rate and a 150fsec pulse width (Coherent, Inc, Palo Alto, CA). The power of the laser light source was regulated to approximately 130mW with a Glan-Thompson polarizer, which, given a transmission efficiency of 10-20%, resulted in approximately 15mW to be delivered at tissue level. The expanded laser light beam was directed into the microscope via a galvanometer-driven x-y scanner (Cambridge Technology, Watertown, MA), and images were generated by raster scanning the x-y mirrors. Thus, the excitation light entered the microscope via a modified epifluorescence light pathway, while the scan lens was positioned such that the x-y scanner was at its eye-point while the field aperture was at its focal point. The axial position of the objective was driven by a piezoelectric driver, with a resolution of 0.05μm over 100μm. The typical frame rate (per single image slice) was approximately 3 seconds.

In order to maximize the number of available photons for detection (while minimizing potential photo-damage), we used a single photon counting system in which the fluorescence signal at each pixel was detected by an R5600-P photo-multiplier tube (Hamamatsu, Bridewater, NJ). This apparatus constituted a photon counting module with high quantum efficiency (12% at 500nm and 25% at 400nm). A 100MHz single photon counting discriminator (F100T, Advanced Research Instruments, Boulder, CO) converted single photon bursts into TTL pulses, which were subsequently counted and

saved on a PC computer (Gateway), as photon intensity modulated images. The 3D deep-tissue volume scans produced 256x256 images with resolution 1.85x1.85μm and a slice thickness of 5μm. Achievable scan depth into the tissue was approximately 200μm.

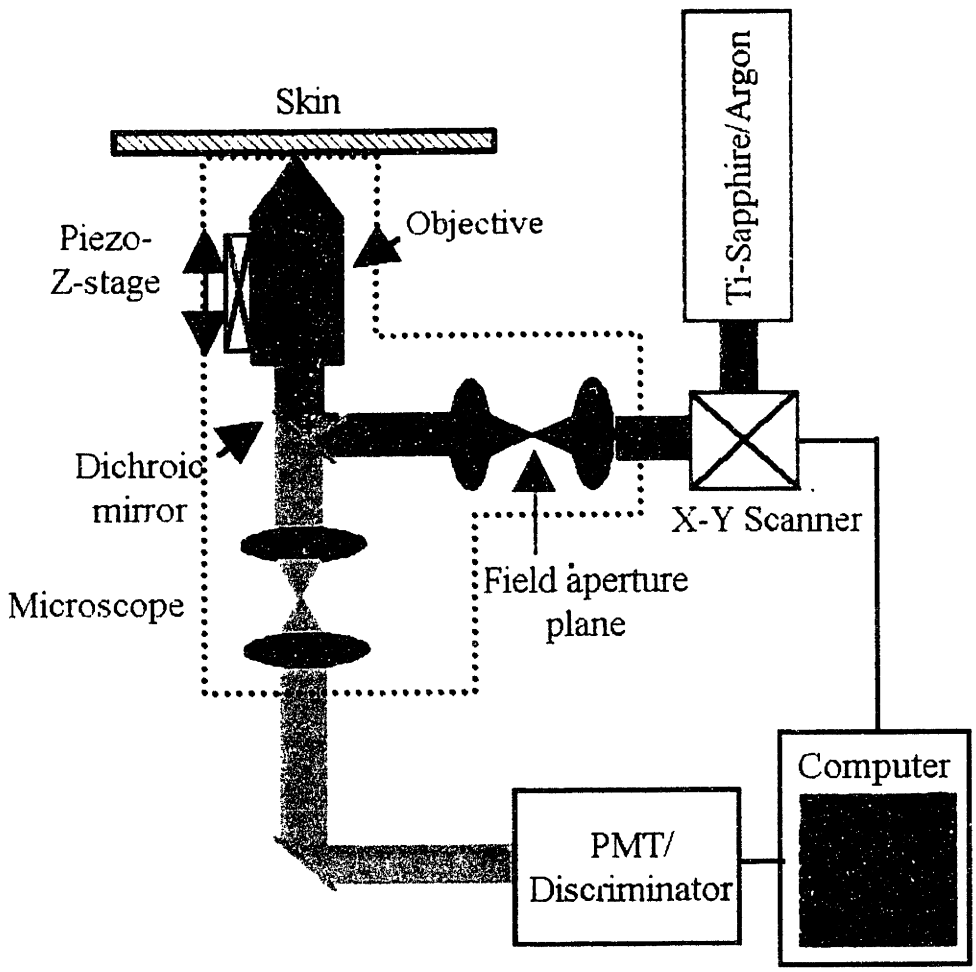

Figure B-3 A schematic of the two-photon apparatus displays how fluorophores in the sample are excited, and how that fluorescence is collected and visualized with integrated computer control.

Appendix C:

Exploring Variability in DTI Data

Diffusion Tensor Imaging (DTI) is a technique that allows for the analysis of myoarchitecture in intact specimens. Chapter 2 presented data from *ex vivo* bovine tongue samples, with one representative dataset displayed. This dataset proved to be qualitatively similar to datasets derived from other bovine tongues (**Figure C-1**). A series of three axial slices from the anterior portion of three separate bovine tongues demonstrated that DTI accurately and repeatedly deciphered the general myoarchitecture of the mammalian tongue. In this figure, processed images were displayed next to their raw data counterparts (a standard T1 weighted image). Processed data were displayed by color-coded pixels whose color represented the orientation of the greatest eigenvector of the calculated diffusion tensor.

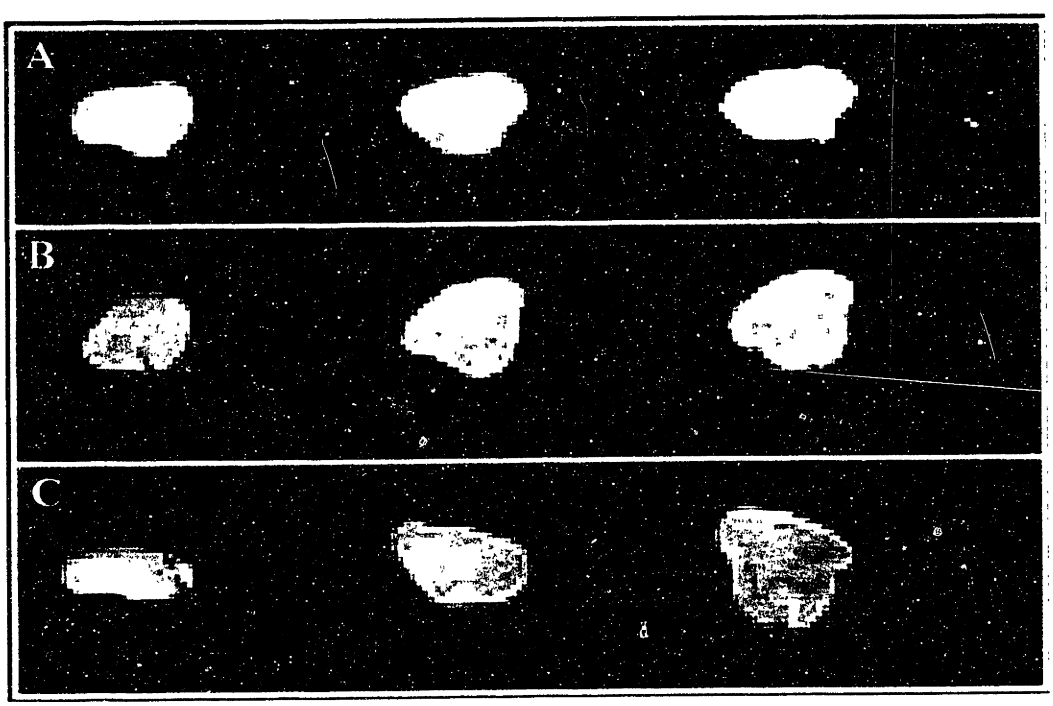

Figure C-1 DTI data from the anterior portion of three separate tongues (A, B, and C) presented a qualitatively similar and reproducible result. Processed data were shown next to their raw counterparts. Pixels in the processed data were color-coded based on the orientation of the principal eigenvector of the computed diffusion tensor. The anterior tongue myoarchitecture was composed of a peripheral sheath of longitudinal fibers (color-coded blue) surrounding an internal core of transversus (red) and verticalis (green) muscle populations.

Appendix D:

Deriving Green's Strain Tensor Components

The following is a derivation of the equations for the non-linear Green's strain tensor components. Consider the general deforming body defined by two line elements, perpendicular in the undeformed state (**Figure D-1**):

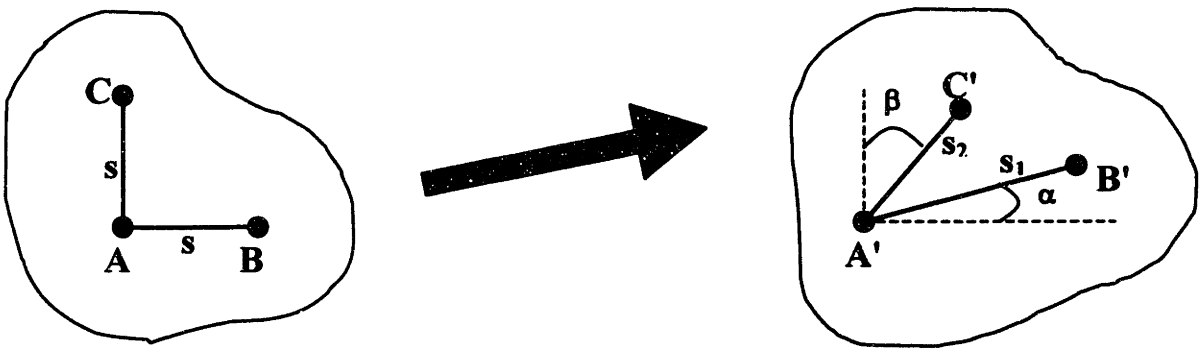

Figure D-1 Two perpendicular line elements describing a general deforming body. As the body deforms, the line elements assume a new length and angular orientation.

The deformation gradient, **F**, transforms any line element dX to dx.

$$dx = \mathbf{F}dX \tag{D.1}$$

By the polar decomposition theorem, the deformation gradient can be decomposed into an orthogonal rotation tensor, **R**, and a symmetric, positive-definite right stretch tensor **U**.

$$\mathbf{F} = \mathbf{RU} \tag{D.2}$$

Thus, assume a resting 3D orthogonal Cartesian coordinate system defined by the unit vectors e_x, e_y, e_z with

$$\overrightarrow{AB} = s\,e_x$$
$$\overrightarrow{AC} = s\,e_y \tag{D.3}$$

and deformed line elements defined by

$$\overrightarrow{A'B'} = \mathbf{F}\overrightarrow{AB} = s\mathbf{F}e_x$$
$$\overrightarrow{A'C'} = \mathbf{F}\overrightarrow{AC} = s\mathbf{F}e_y \tag{D.4}$$

Hence, since the rotation tensor does not cause any stretch, the deformed line element lengths are given by the following formulae:

$$s_1 = |\mathrm{A'B'}| = s|\mathbf{F}e_x| = s|\mathbf{U}e_x|$$
$$s_2 = |\mathrm{A'C'}| = s|\mathbf{F}e_y| = s|\mathbf{U}e_y| \tag{D.5}$$

Also, the relative angle between the two deformed line elements can be given by

$$\overrightarrow{\mathrm{A'B'}} \bullet \overrightarrow{\mathrm{A'C'}} = \mathrm{s}^2\,\mathbf{F}e_x \bullet \mathbf{F}e_y = \mathrm{s}_1\mathrm{s}_2\cos(\pi/2-\phi)$$

or

$$\mathrm{s}^2\,\mathbf{U}e_x \bullet \mathbf{U}e_y = \mathrm{s}_1\mathrm{s}_2\sin\phi$$

hence

$$\mathbf{U}e_x \bullet \mathbf{U}e_y = \frac{\mathrm{s}_1\mathrm{s}_2}{\mathrm{s}^2}\sin\phi \tag{D.6}$$

The general definition of a Lagrangian strain tensor is

$$\mathbf{E}_{\text{Lagrangian}} = \frac{1}{m}\left(\mathbf{U}^m - \mathbf{I}\right) \tag{D.7}$$

where $m \neq 0$ is a scalar. By definition (Lai, Rubin et al., 1993; Chandrasekharaiah and Debnath, 1994), Green's non-linear strain tensor is given by the special case, m=2.

$$\mathbf{E}_{\text{Green}} = \frac{1}{2}\left(\mathbf{U}^2 - \mathbf{I}\right) \tag{D.8}$$

Finally, the elements of this strain tensor can be derived by incorporating equations **(D.5)** and **(D.6)** with the definition given in **(D.8)**.

$$
\begin{aligned}
E_{xx} &= \mathbf{E}e_x \bullet e_x = \frac{1}{2}\left(\mathbf{U}^2 - \mathbf{I}\right)e_x \bullet e_x \\
&= \frac{1}{2}\left(\mathbf{U}^2 e_x \bullet e_x - 1\right) = \frac{1}{2}\left(\mathbf{U}e_x \bullet \mathbf{U}e_x - 1\right) \\
&= \frac{1}{2}\left(\left|\mathbf{U}e_x\right|^2 - 1\right) \\
&= \frac{1}{2}\left(\frac{s_1^2}{s^2} - 1\right)
\end{aligned}
\tag{D.9}
$$

$$
\begin{aligned}
E_{yy} &= \mathbf{E}e_y \bullet e_y = \frac{1}{2}\left(\mathbf{U}^2 - \mathbf{I}\right)e_y \bullet e_y \\
&= \frac{1}{2}\left(\mathbf{U}^2 e_y \bullet e_y - 1\right) = \frac{1}{2}\left(\mathbf{U}e_y \bullet \mathbf{U}e_y - 1\right) \\
&= \frac{1}{2}\left(\left|\mathbf{U}e_y\right|^2 - 1\right) \\
&= \frac{1}{2}\left(\frac{s_2^2}{s^2} - 1\right)
\end{aligned}
\tag{D.10}
$$

$$
\begin{aligned}
E_{xy} &= \mathbf{E}e_y \bullet e_x = \frac{1}{2}\left(\mathbf{U}^2 - \mathbf{I}\right)e_y \bullet e_x \\
&= \frac{1}{2}\mathbf{U}^2 e_y \bullet e_x = \frac{1}{2}\mathbf{U}e_x \bullet \mathbf{U}e_y \\
&= \frac{s_1 s_2}{2s^2}\sin\phi
\end{aligned}
\tag{D.11}
$$

These definitions provide a complete 2-Dimensional description of the strain state. However, a 3-dimensional extension of the data can also be provided if the tissue is assumed to be incompressible. With this assumption, element volume is isochoric, and the third principal strain can be found from the determinant of the deformation gradient and definition **(D.6)**. Here E_{11} and E_{22} are the principal strains in the x-y plane.

Incompressibility requires that det**F**=1. Because of **(D.2)** and the orthogonality of the rotation tensor **R**, this implies that det$\mathbf{U}^2$=1. Consequently by **(D.6)**,

$$\Rightarrow \det(2\mathbf{E}+\mathbf{I})=1$$

$$\det\begin{pmatrix} 2E_{11}+1 & 0 & 0 \\ 0 & 2E_{22}+1 & 0 \\ 0 & 0 & 2E_{33}+1 \end{pmatrix}=1$$

$$\Rightarrow (1+2E_{11})(1+2E_{22})(1+2E_{33})=1$$

$$E_{33}=\frac{1}{2}\left[\frac{1}{(1+2E_{11})(1+2E_{22})}-1\right] \qquad \textbf{(D.12)}$$

If the out-of-tagging-plane shear strains (E_{xz} and E_{yz}) are negligible, E_{zz} = E_{33}, and the orientation of the third eigenvector is coincident with the z-axis. Hence, the strain state can be completely defined in the x-y-z Cartesian coordinate system.

Appendix E:

Error and Sensitivity Analysis for Tagging MRI

Certain assumptions were made in the development of the previously described tagging MRI strain model. This section is an attempt to quantify the errors incurred by hypothetically erroneous assumptions, as well as to test the sensitivity of the model to these errors. There is also an attempt to quantify the errors introduced during data reduction, through manual image digitization.

E.1 Digitization Error

Manual digitization in tagging MRI post-processing analysis was subject to human error, as the operator, whether trained or not, must manually click on the perceived tag line intersection points. Digitization was done on a Dell 17" monitor with a resolution of 1280 x 1024 (width x height) in screen pixels. At maximum window size, the image (256x256) filled approximately 70% of screen height, thus the screen was composed of 366 image pixels, or 1 screen pixel = 0.357 image pixels.

In this analysis it will be assumed that the human digitization error was ±2 screen pixels and that the initial (undeformed) tag spacing was 5.1 image pixels. Because the strain calculation was non-linear, the error in axial strain will depend on the deformed tag spacing, s_1. Thus, the theoretical axial strain error can be expressed as the following difference:

$$\text{axial strain error} = 0.5*((s_1 \pm \epsilon)^2 / 5.1^2 - 1) - 0.5*(s_1^2 / 5.1^2 - 1) \quad \textbf{(E.1)}$$

where ϵ = 0.714 image pixels and s_1 = 3 to 10 image pixels (physiological range). The axial strain error has been plotted below, and shows a maximal error of 28.63% at a real strain of 142.2%. However, these errors would be most pernicious at small measured strains where they would comprise a higher percentage of the reported value.

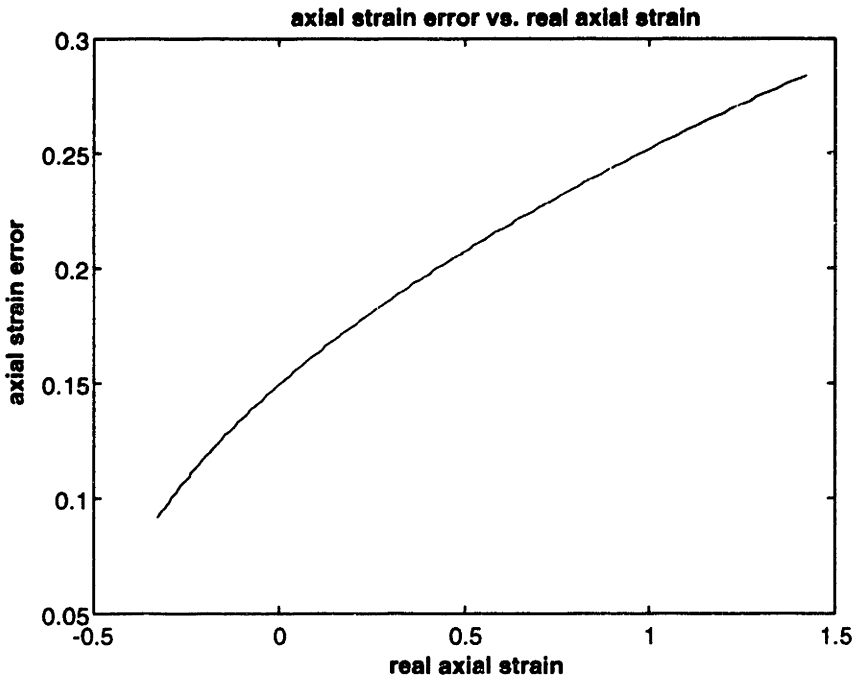

Figure E-1 Digitization strain error increases non-linearly as a function the real axial strain. However, the digitization error may be most pernicious at lower real strain values, when it comprises a greater percentage of the reported value.

E.2 Incompressibility

In order to deduce the through-plane axial strain, E_{zz}, from data measured solely in the x-y plane, the model assumes incompressibility of the deforming muscle tissue. This constraint leads to the condition of isochoric or volume preserving deformation. Mathematically, isochoric deformation can be represented by setting the determinant of the deformation gradient, F, equal to unity. This leads to an expression for the unknown through-plane axial strain E_{zz}, which is equivalent to E_{33} :

$$E_{33} = \frac{i}{2}\left(\frac{1+\epsilon}{(1+2E_{11})(1+2E_{22})} - 1\right) \tag{E.2}$$

where ϵ can range from -0.1 to 0.1 for reasonable physiological limits of tissue compressibility. Muscle tissue has been shown to be isochoric (maintaining its volume under deformation) or incompressible by x-ray diffraction methods (Elliott, Lowy et al., 1963), thus a compressibility of 10% can be deemed conservative. The x-y plane principal strains, E_{11} and E_{22}, have been taken from an element in tongue protrusion which presented extreme values of strain: $E_{11} = 2.123$ and $E_{22} = 0.232$. The resulting percent error compared to an E_{zz} calculated by assuming perfect incompressibility ($E_{zz} = -0.435$) has been plotted below (**Figure E-2**). The maximum percent error was found to be only 1.5% at a value of 10% compressibility (deviation of 0.1 from a unity determinant).

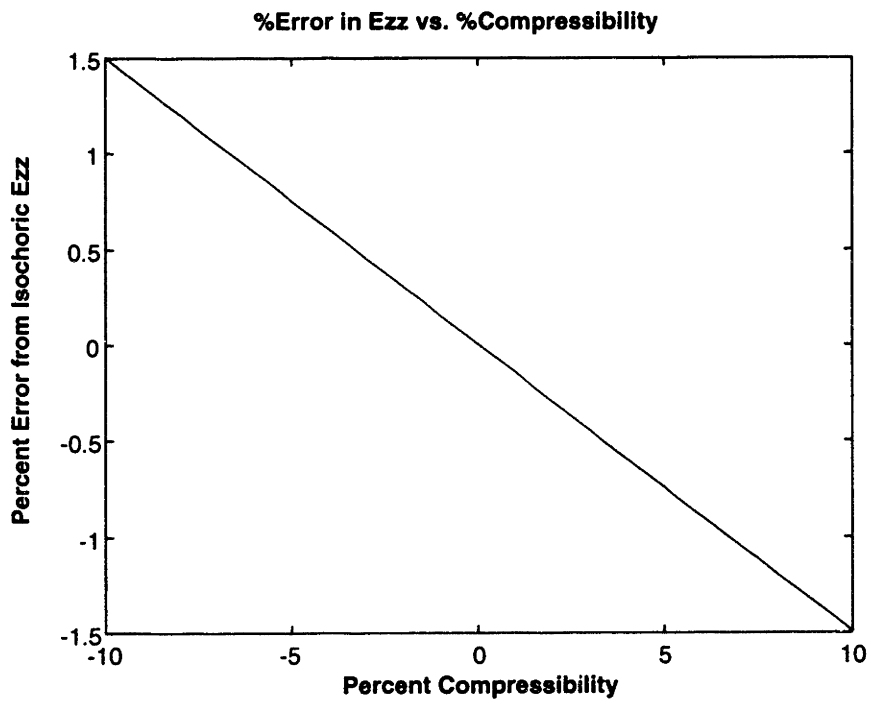

Figure E-2 Percent error in calculating E_{zz} as a function of compressibility shows that the error in assuming tissue incompressibility is relatively low within a physiological range of compressibility.

E.3 Through Plane Shear Strains

An important assumption made in determining the through plane axial strain, E_{zz}, from the incompressibility condition was that through-plane shear strains, E_{xz} and E_{yz}, were negligible. This assumption was deemed reasonable by the fact that the motions studied were symmetric about the mid-sagittal plane. In order to test the sensitivity of the model to through-plane shears, representative

elements were chosen from a tongue protrusion dataset. This tongue motion was chosen since it involved extreme strain values; hence, element 39 was chosen for its extreme axial strain value, while element 30 was chosen for its extreme shear strain value. These elements were augmented as 39' and 30' to investigate the effect of variable in-plane axial and shear strain (**Table E-2**). Elements 39 and 39' have similar E_{yy} and E_{xy} values, but element 39' was under half the axial strain, E_{xx}, as element 39. Elements 30 and 30' had similar axial strain values, but element 30' was under half the shear strain, E_{xy}, as element 30.

Element	E_{xx}	E_{yy}	E_{xy}
39	2.115	0.240	-0.125
39'	1.057	0.240	-0.125
30	0.737	0.604	-0.630
30'	0.737	0.604	-0.315

Table E-2 Elements used in sensitivity study (39: extreme axial strain; 30: extreme shear strain; 39', 30': augmented elements)

In order to derive the through plane axial strain, E_{zz}, the isochoric condition must be solved in terms of the known in-plane axial and shear strains, and through-plane shear strains.

$$E_{zz} = \frac{1}{2}\left(\frac{1-2E_{yz}\left(4E_{xy}E_{xz}-2(2E_{xx}+1)E_{yz}\right)-2E_{xz}\left(4E_{xy}E_{yz}-2(2E_{yy}+1)E_{xz}\right)}{(1+2E_{xx})(1+2E_{yy})-2E_{xy}^2}-1\right) \qquad \text{(E.3)}$$

The in-plane strains were taken from representative extreme strain elements, while through-plane shear strains, E_{xz} and E_{yz}, were identically incremented from a value of 0.0 to 0.7. The percent error in the new E_{zz} was computed relative to the E_{zz} value under zero through-plane shear strains.

The results of this study show several important findings (**Figure E-3**). Firstly, through-plane shears always lead to a smaller calculated E_{zz}, i.e. negative percent error. Furthermore, through-plane shear strain greater than 20 or 30% can lead to significant errors in calculating E_{zz}, reaffirming the necessity that the motions studied be relatively symmetric about the x-y plane, minimizing through plane shear. Finally, the error was more sensitive to extreme E_{xy} values (element 30) compared to E_{xx} values (elements 39, 39'). This effect was also seen when comparing element 30 to 30'.

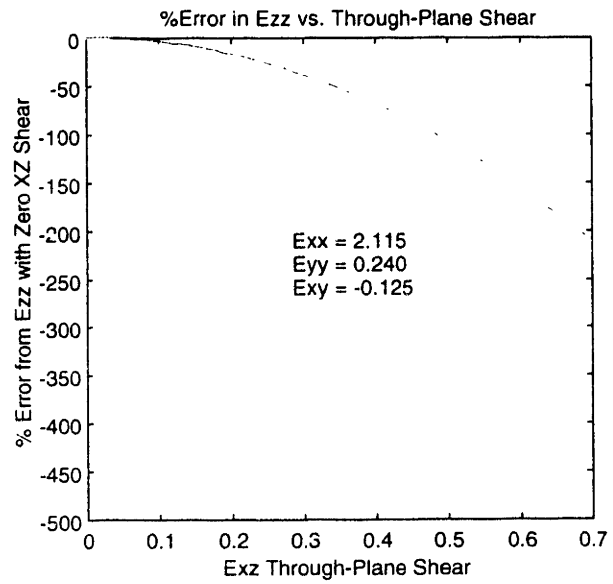

Element 39

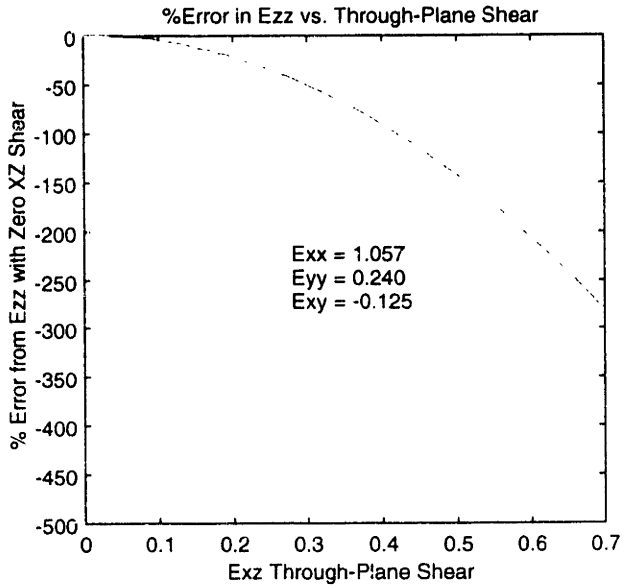

Element 39'

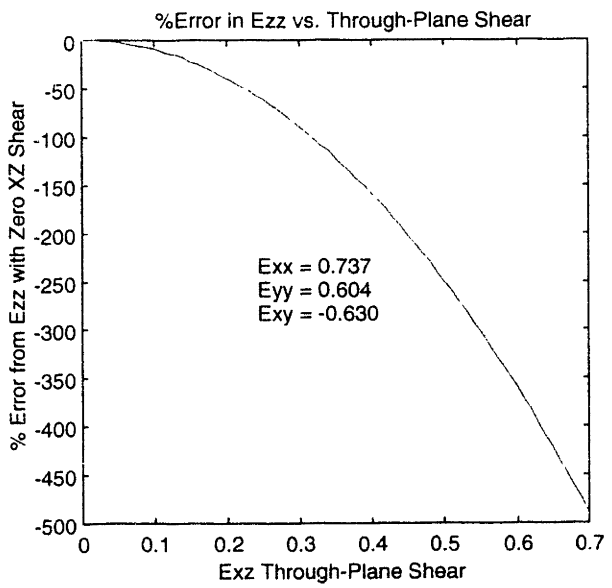

Element 30

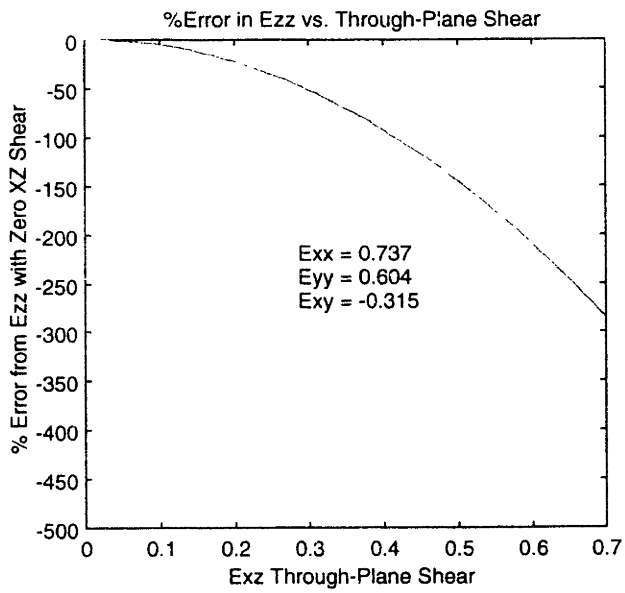

Element 30'

Figure E-3 Results of the through-plane shear sensitivity study demonstrate that through-plane shears always lead to a smaller calculated E_{zz}, i.e. negative percent error. Furthermore, through-plane shear strain greater than 20 or 30% can lead to significant errors in calculating E_{zz}, reaffirming the necessity that the motions studied be relatively symmetric about the x-y plane, thus minimizing through plane shear. The error was more sensitive to extreme E_{xy} values (element 30) compared to E_{xx} values (elements 39, 39').

Appendix F:

Non-linear Strain Definition for Curved Beam

The derivation of Green's strain definition for bending strain in a curved beam undergoing bending was based on several geometric manipulations (**Figure F-1**).

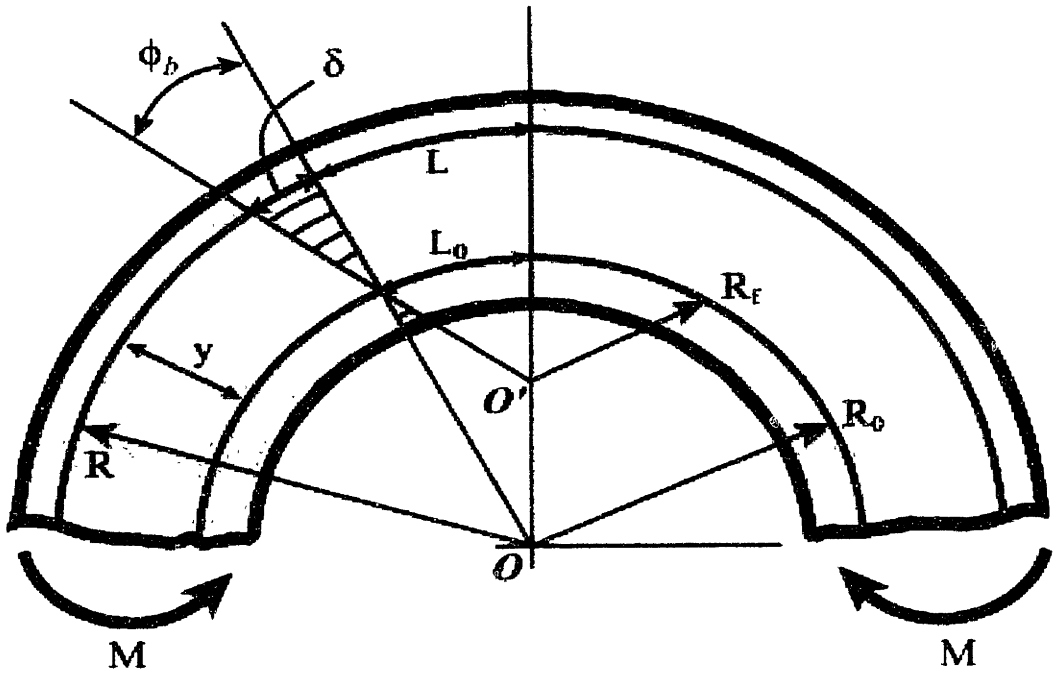

Figure F-1 Schematic of initially bent beam subjected to bending moment, M, which causes the center of curvature to shift from *O* to *O'* (actual beam deformation not shown for clarity sake). L_0 lies along the neutral axis.

Non-linear bending strain for a curved beam was defined on the basis of the fact that the angle, ϕ_b, which relates the rotation of a cross-sectional plane through the beam, can be expressed by

$$\phi_b = L_o\left(\frac{1}{R_f} - \frac{1}{R_o}\right) \tag{F.1}$$

where L_o is the arc length at the neutral axis, R_o is the initial radius of the bent beam, and R_f is the final radius of curvature of the beam. Euler, in 1744, was the first to show that an initially bent beam subjected to a bending moment will behave by the following equation:

$$\frac{1}{R_b} = \frac{1}{R_f} - \frac{1}{R_o} \tag{F.2}$$

where R_b is the radius of curvature caused by the bending moment, M. Hence the angle, ϕ_b can be expressed more simply as:

$$\phi_b = L_o\left(\frac{1}{R_b}\right) \tag{F.3}$$

The axial deflection , δ, of the arc length L at a distance y from the neutral axis can then be expressed as

$$\delta = y\phi_b = yL_o\left(\frac{1}{R_b}\right) \tag{F.4}$$

Thus, the stretch at a distance, y, from the neutral axis can be expressed:

$$U = \frac{L+\delta}{L} = 1 + y\frac{L_o}{L}\left(\frac{1}{R_b}\right) \tag{F.5}$$

Finally, noting through geometric similarity that

$$\frac{L_o}{L} = \frac{R_o}{R} = \frac{R_o}{R_o + y} \tag{F.6}$$

Green's strain definition, $\varepsilon = {}^1/_2(U^2-1)$, can be applied to define non-linear bending strain in a curved beam using the following definition:

$$\varepsilon = \frac{1}{2}\left[\left(1 + \frac{yR_o}{y+R_o}\left(\frac{1}{R_b}\right)\right)^2 - 1\right] \tag{F.7}$$

This strain definition was used in applying the compatibility condition to solve the bimetal strip problem in chapter 4.

Appendix G:

Finding the Neutral-Axis in a Curved Beam

It is important to note that for an initially curved beam undergoing elastic bending, the neutral axis does not pass through the centroid of cross-sectional area, but is displaced toward the center of initial curvature (Shanley, 1957). Mathematically, the neutral axis is found by setting the total (integrated) axial force over the cross-section equal to zero:

$$P = \int \sigma \, dA = 0 \tag{G.1}$$

Assuming a linearly elastic material, and the absence of a large deviation from the neutral axis for large deformations, equation **(G.1)** can be expanded as:

$$\int E\,(R\text{-}R_o)\frac{R_o}{R}\left(\frac{1}{R_b}\right)dA = 0 \tag{G.2}$$

where R is the radius of curvature to any material point on the cross section, R_o is the radius of curvature at the neutral axis, R_b is the radius of curvature produced by the moment. This equation can then be simplified, assuming that R_b and R_o do not vary over the cross-section:

$$\int \frac{R\text{-}R_o}{R} dA = 0 \tag{G.3}$$

or

$$\int dA - R_o \int \frac{dA}{R} = 0 \tag{G.4}$$

which can be rearranged to yield an expression for the radius of curvature of the neutral axis:

$$R_o = \frac{A}{\int \frac{dA}{R}} \tag{G.5}$$

Hence, for the cross-sectional geometry assumed by the tongue model, the neutral-axis can be solved for explicitly:

$$R_o = \frac{h}{\ln\left(\frac{R_2}{R_1}\right)} \tag{G.6}$$

where R_2 is the convex side radius, and R_1 is the concave side radius (**Figure G-1**). In the bimetal strip model in Chapter 4, this definition was used to calculate the strain distribution across both curved beam cross-sections.

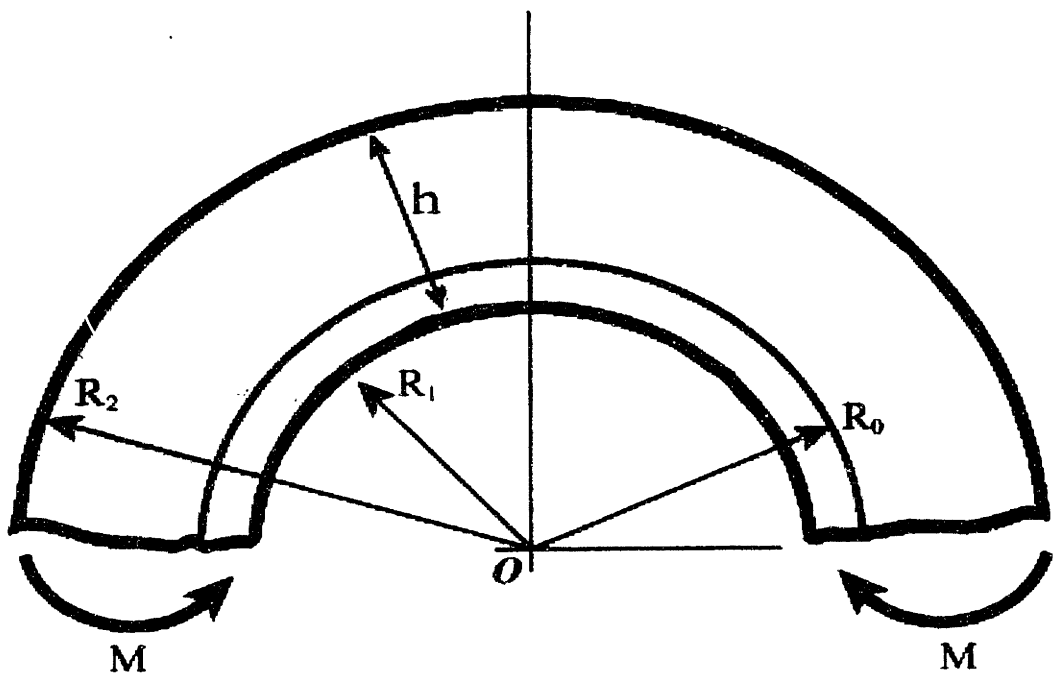

Figure G-1 Initially bent beam undergoing bending by moment, M. R_o defines the location of the neutral axis. Notice that it is closer to the concave edge, R_1, than the centroidal axis (not shown).

Bibliography

1. Abbott, B. and R. Baskin (1962). "Volume changes in frog muscle during contraction." Journal of Physiology, London **161**: 379-391.

2. Abd-El-Malek, S. (1938). "Observations on the morphology of the human tongue." Journal of Anatomy **73**: 201-210.

3. Abd-El-Malek, S. (1955). "The part played by the tongue in mastication and deglutition." Journal of Anatomy **89**: 250-254.

4. Agur, A. and M. Lee (1999). Grant's Atlas of Anatomy. Baltimore, Lippincott Williams and Wilkins.

5. Axel, L. and L. Dougherty (1989). "MR imaging of motion with spatial modulation of magnetization." Radiology **171**: 841-845.

6. Azhari, H., J. L. Weiss, et al. (1993). "Noninvasive quantification of principal strains in normal canine hearts using tagged MRI images in 3-D." American Journal of Physiology **264**: H205-H216.

7. Barclay, A. (1929). "The normal mechanisms of swallowing." Mayo Clinic Proceedings **4**: 251-257.

8. Basser, P., J. Mattiello, et al. (1993). MR imaging of fiber tract direction and diffusion in anisotropic tissues. 12 annual meeting of the Society of Magnetic Resonance in Medicine.

9. Basser, P. J. (1995). "Inferring microstructural features and the physiological state of tissues from diffusion-weighted images." NMR in Biomedicine **8**: 333-344.

10. Basser, P. J., J. Mattiello, et al. (1994). "MR diffusion tensor spectroscopy and imaging." Biophysical Journal **66**: 259-267.

11. Baum, B. and L. Bodner (1983). "Aging and oral motor function: evidence for altered performance among older persons." Journal of Dental Research **62**(1): 2-6.

12. Bennett, G. and R. Hutchinson (1946). "Experimental studies on the movements of the mammalian tongue. II. The protrusion mechanism of the tongue (dog)." Anatomical Record **94**: 59-72.

13. Bihan, D. L. (1995). "Molecular diffusion, tissue microdynamics and microstructure." NMR in Biomedicine **8**: 375-386.

14. Bloch, F. (1946). "Nuclear induction." Physical Reviews **70**: 460-474.

15. Bosma, J. (1963). "Maturation of function of the oral and pharyngeal region." American Journal of Orthodontics **49**: 94-104.

16. Brodie, A. (1952). "Consideration of musculature in diagnosis, treatment and retention." American Journal of Orthodontics **38**: 823-835.

17. Burke, R., Ed. (1981). Motor unit recruitment: What are the ciritical factors? Prog Clin Neurophysiol. Basel, Karger.

18. Centonze, V. and J. White (1998). "Multiphoton Excitation provides optical sections from deeper within scattering specimens than confocal imaging." Biophysical Journal **75**(4): 2015-2024.

19. Chandrasekharaiah, D. and L. Debnath (1994). Continuum Mechanics, Academic Press.

20. Chapman, G. (1950). "Of the movement of worms." Journal of Experimental Biology **27**: 29-39.

21. Chiel, H. J., P. Crago, et al. (1992). "Biomechanics of a muscular hydrostat: a model of lapping by a reptilian tongue." Biological Cybernetics **67**: 403-415.

22. Cook, I., W. Dodds, et al. (1989). "Timing of videofluoroscopic, manometric events, and bolus transit during the oral and pharyngeal phases of swallowing." Dysphagia **4**: 8-15.

23. Cory, D. G. and A. N. Garroway (1990). "Measurement of translational displacement probabilities by NMR: an indicator of compartmentation." Magnetic Resonance in Medicine **14**: 435-444.

24. Cotran, R., V. Kumar, et al. (1994). Robbins: Pathologic Basis of Disease. Philadelphia, W.B. Saunders Co.

25. Crandall, S. (1959). An introduction to the mechanics of solids. New York, McGraw-Hill Publications.

26. Croghan, J., E. Burke, et al. (1994). "Pilot study of 12 month outcomes of nursing home patients with aspiration on videofluoroscopy." Dysphagia **9**: 141-146.

27. Dantas, R., M. Kern, et al. (1990). "Effect of swallowed bolus variables on oral and pharyngeal phases of swallowing." American Journal of Physiology **258**: G675-G681.

28. Davalos, A., W. Ricart, et al. (1996). "Effect of malnutrition after acute stroke on clinical outcome." Stroke **27**: 1028-1032.

29. Denk, W., J. Strickler, et al. (1990). "Two-photon laser scanning fluorescence microscopy." Science **248**(4951): 73-76.

30. Depaul, R. and J. H. Abbs (1996). "Quantitative morphology and histochemistry of instrinsic lingual muscle fibers in Macaca fascicularis." Acta Anatomica **155**: 29-40.

31. Devgan, B. K., C. W. Gross, et al. (1978). "Anatomic and physiologic aspects of sword swallowing." Ear, Nose, and Throat Journal **57**: 58-66.

32. Doble, E. A., J. C. Leiter, et al. (1985). "A noninvasive intraoral electromyographic electrode for genioglossus muscle." Journal of Applied Physiology **58**(4): 1378-1382.

33. Dodds, W., E. Stewart, et al. (1990). "Physiology and radiology of the normal oral and pharyngeal phases of swallowing." American Journal of Radiology **154**: 953-963.

34. Doorn, A. V., P. H. M. Bovendeerd, et al. (1996). "Determination of muscle fibre orientation using diffusion-weighted MRI." European Journal of Morphology **34**(1): 5-10.

35. Doran, D. and H. Baggett (1972). "The genioglossus muscle: a reassessment of its anatomy in some mammals, including man." Acta Anatomica **83**: 403-410.

36. Doran, G. (1975). "Review of the evolution and phylogeny of the mammalian tongue." Acta Anatomica **91**: 118-129.

37. Doran, G. and D. Allbrook (1973). "The tongue and associated structures in two species of African pangolins, Manis gigantia and Manis tricuspis." Journal of Mammalogy **54**: 887-899.

38. Doran, G. and H. Baggett (1971). "A structural and functional classification of mammalian tongues." Journal of Mammalogy **52**(2): 427-429.

39. Drace, J. E. and N. J. Pelc (1994). "Skeletal muscle contraction: analysis with use of velocity distributions from phase-contrast MR Imaging." Radiology **193**: 423-429.

40. Duck, F. A. (1990). Physical Properties of Tissue: A Comprehensive Reference Book. London, Academic Press.

41. Elliott, G. F., J. Lowy, et al. (1963). "An X-Ray and light-diffraction study of the filament lattice of striated muscle in the living state and in rigor." Journal of Molecular Biology **6**: 295-305.

42. English, A. and W. Letbetter (1982). "A histochemical analysis of identified compartments of cat lateral gastrocnemius muscle." Anatomical Record **204**: 123-130.

43. Gans, C. and W. Bock (1965). "The functional significance of muscle architecture: a theoretical analysis." Ergebnisse dur Anatomie und Entwicklungsgeschichte **35**: 115-142.

44. Gilbert, R., S. Daftary, et al. (1998). "Patterns of lingual deformation associated with bolus containment and propulsion during deglutition as determined by echoplanar magnetic resonance imaging." Journal of Magnetic Resonance Imaging **8**(3): 554-560.

45. Gilbert, R., T. Reese, et al. (1998). "Determination of Lingual Myoarchitecture in Whole Tissue by NMR Imaging of Anisotropic Water Diffusion." American Journal of Physiology **275**(2 (Part 1)): G363-G369.

46. Groher, M. (1997). Dysphagia: Diagnosis and Management, Butterworth-Heinemann Press.

47. Hajnal, J., M. Doran, et al. (1991). " MR imaging of anisotropically restricted diffusion of water in the nervous system: technical, anatomic, and pathologic considerations." Journal of Computer Assisted Tomography **15**: 1-18.

48. Hamlet, S., M. Stone, et al. (1988). "Posterior tongue grooving in deglutition and speech: Preliminary observations." Dysphagia **3**: 65-68.

49. Hashimoto, K. and S. Suga (1986). "Estimation of the muscular tensions of the human tongue by using a three-dimensional model of the tongue." Journal of the Acoustical Society of Japan **7**(1): 39-46.

50. Hiiemae, K. and A. Crompton (1985). Mastication, food transport, and swallowing. Functional Vertebrate Morphology. M. Hildebrand, D. M. Bramble, K. F. Liem and D. B. Wake. Cambridge, MA, Belknap Press: 262-290.

51. Hsu, E. W., A. L. Muzikant, et al. (1998). "Magnetic resonance myocardial fiber-orientation mapping with direct histological correlation." American Journal of Physiology **274**: H1627-H1634.

52. Kahrilas, P., J. Logemann, et al. (1992). "Pharyngeal clearance during swallowing: a combined manometric and videofluoroscopic study." Gastroenterology **103**: 128-136.

53. Kahrilas, P. J., S. Lin, et al. (1993). "Deglutitive tongue action: volume accommodation and bolus propulsion." Gastroenterology **104**: 152-162.

54. Kakita, Y. and O. Fujimura (1977). "Computational model of the tongue: a revised version." Journal of the Acoustic Society of America **62**: S15(A).

55. Kier, W. and K. Smith (1985). "Tongues, tentacles, and trunks: The biomechanics of movement in muscular-hydrostats." Zoological Journal of the Linnaean Society **83**: 307-324.

56. Kiritani, S., K. Miyawaki, et al. (1976). "A computational model of the tongue." Annual Bulletin, Research Institute of Logopedics and Phoniatrics, University of Tokyo **10**: 243-251.

57. Krol, R., S. Knuth, et al. (1984). "Selective reduction of genioglossus muscle activity by alcohol in normal human subjects." American Review of Resperitory Disease **129**: 247-250.

58. Kumada, M., M. Niitsu, et al. (1992). "A study of the inner structure of the tongue in the production of the 5 Japanese vowels by tagging snapshot MRI." Annual Belletin of the Research Institute of Logopedics and Phoniatrics of the University of Tokyo **26**: 1-11.

59. Lai, W., D. Rubin, et al. (1993). Introduction to Continuum Mechanics, Pergamon Press.

60. Livingston, R. (1956). "Some observations on the natural history of the tongue." Annals of the Royal College of Surgeons, England **19**: 185-200.

61. Lowe, A. (1981). "The neural regulation of tongue movements." Progress in Neurobiology **15**: 295-344.

62. Masters, B., P. So, et al. (1997). "Multiphoton excitation fluorescence microscopy and spectroscopy of in vivo human skin." Biophysical Journal **72**: 2405-2412.

63. Matsumoto, Y. (1967). "Validity of the force-velocity relation for the muscle contraction in the length region, l<lo." The Journal of General Physiology **50**: 1125-1137.

64. Matthys, L. and G. DeMey (1996). "An analysis of an engineering model for the thermal mismatch stresses at the interface of a uniformly heated two layer structure." The International Journal of Microcircuits and Electronic Packaging **19**(3): 323-329.

65. McLean, M. and J. Prothero (1992). "Determination of relative fiber orientation in heart muscle: methodological problems." The Anatomical Record **232**: 459-465.

66. McMurrich, J. (1930). Leonardo da Vinci the Anatomist. Baltimore, Carnegie Institute.

67. Merboldt, K., W. Hanicke, et al. (1991). "Diffusion imaging using stimulated echoes." Magnetic Resonance in Medicine **19**: 233-235.

68. Miller, A. J. (1982). "Deglutition." Physiological Reviews **62**(1): 129-184.

69. Miyawaki, K. (1974). "A study of the musculature of the human tongue." Annual Bulletin of the Research Institute of Logopedics and Phoniatrics - University of Tokyo **8**: 23-50.

70. Miyawaki, K., H. Hirose, et al. (1975). "A preliminary report on the electromyographic study of the activity of lingual muscles." Annual Bulletin of the Research Institute of Logopedics and Phoniatrics - University of Tokyo **9**: 91-106.

71. Moore, K. (1992). Clinically Oriented Anatomy. Baltimore, Williams and Wilkins.

72. Moseley, M., J. Kucharczyk, et al. (1991). "Anisotropy in diffusion-weighted MRI." Magnetic Resonance in Medicine **19**: 321-326.

73. Mu, L. and I. Sanders (1999). "Neuromuscular Organization of the Canine Tongue." The Anatomical Record **256**: 412-424.

74. Napadow, V., Q. Chen, et al. (2001). "Quantitative analysis of 3d-resolved fiber architecture in heterogeneous skeletal muscle tissue using NMR and optical imaging methods." Biophysical Journal **80**: 2968-2975.

75. Napadow, V., Q. Chen, et al. (1999). "Biomechanical Basis for Lingual Muscular Deformation During Swallowing." American Journal of Physiology **40**(3): G695-G701.

76. Napadow, V., Q. Chen, et al. (1999). "Intramural Mechanics of the Human Tongue in Association with Physiological Deformations." Journal of Biomechanics **32**: 1-12.

77. Niitsu, M., M. Kumada, et al. (1994). "Tongue displacement: visualization with rapid tagged magnetization-prepared MR imaging." Radiology **191**: 578-580.

78. Norris, D. G. and T. Niendorf (1995). "Interpretation of DW-NMR data: dependence on experimental conditions." NMR in Biomedicine **8**: 280-288.

79. Perkell, J., M. Cohen, et al. (1992). "Electromagnetic midsagittal articulation system for transducing speech articulatory movements." Journal of the Acoustic Society of America **92**: 3078-3096.

80. Pierpaoli, C. and P. J. Basser (1996). "Toward a quantitative assessment of diffusion anisotropy." Magnetic Resonance in Medicine **36**: 893-906.

81. Pouderoux, P. and P. J. Kahrilas (1995). "Deglutitive tongue force modulation by volition, volume, and viscosity in humans." Gastroenterology **108**: 1418-1426.

82. Proffit, W. (1973). "Muscle pressures and tooth position: a review of current research." Australian Orthodontics Journal **3**: 104-108.

83. Reese, T., R. Weisskoff, et al. (1998). "Diffusion NMR facilitated by a refocused edy-current EPI pulse sequence." Proceeding of the International Society for Magnetic Resonance in Medicine, Sixth Annual Meeting **1**: 663.

84. Reese, T. G., R. M. Weisskoff, et al. (1995). "Imaging myocardial fiber architecture in vivo with magnetic resonance." Magnetic Resonance in Medicine **34**: 786-791.

85. Ringel, R. and S. Ewanowski (1965). "Oral perception. 1. Two point discrimination." Journal of Speech and Hearing Research **8**: 389-398.

86. Russ, J. (1999). The Image Processing Handbook, CRC Press.

87. Sanguineti, V., R. Laboissiere, et al. (1997). "A control model of human tongue movements in speech." Biological Cybernetics **77**(1): 11-22.

88. Sauerland, E. and R. Harper (1976). "The human otngue during sleep: electromyographic activity of the genioglossus muscle." Experimental Neurology **51**: 160-170.

89. Scardella, A. T., N. Krawciw, et al. (1993). "Strength and endurance characteristics of the normal human genioglossus." American Review of Resperitory Disease **148**: 179-184.

90. Shanley, F. (1957). Strength of Materials. New York, McGraw-Hill Book Company, Inc.

91. Shawker, T., B. Sonies, et al. (1984). Sonography of speech and swallowing. Ultrasound Annual. R. Sanders and M. Hill. New York, Raven: 237-260.

92. Site, V. H. P. W. "Visible Human Project Web Site - http://www.nlm.nih.gov/research/visible.".

93. Smith, K. (1986). "Morphology and function of the tongue and hyoid apparatus in Varanus (Varanidae, Lacertilia)." Journal of Morphology **187**: 261-287.

94. Smith, K. K. (1984). "The use of the tongue and hyoid apparatus during feeding in lizards (Ctenosaura similis and Tupinambis nigropunctatus)." Journal of Zoology, London **202**: 115-143.

95. Smith, K. K. and W. M. Kier (1989). "Trunks, tongues, and tentacles: moving with skeletons of muscle." American Scientist **77**: 29-35.

96. Smithard, D., P. O'Neil, et al. (1997). "The natural history of dysphagia following a stroke." Dysphagia **12**: 188-193.

97. So, P., C. Kim, et al. (1998). "Two-photon deep tissue ex vivo imaging of mouse dermal and subcutaneous structures." Optics Express **3**: 339-350.

98. Sontag, C. (1925). "The comparative anatomy of the tongues of mammalia. XII. Summary, classification, and physiology." Proceedings of the Zoological Society, London **21**: 701-762.

99. Stejskal, E. (1965). "Use of spin echoes in a pulsed magnetic field gradient to study anisotropic, restricted diffusion and flow." Journal of Chemical Physics **43**: 3597-3603.

100. Stone, M. (1990). "A three-dimensional model of tongue movement based on ultrasound and x-ray microbeam data." Journal of the Acoustical Society of America **87**: 2207-2217.

101. Suhir, E. (1989). "Interfacial stresses in bimetal thermostats." Journal of Applied Mechanics **56**: 595-600.

102. Takemoto, H. (2001). "Morphological analyses of the human tongue musculature for three-dimensional modeling." Journal of Speech, Language, and Hearing Research **44**: 95-107.

103. Timoshenko, S. (1925). "Analysis of bimetal thermostats." Journal of the Optical Society of America **11**: 233-255.

104. Wedeen, V., T. Reese, et al. (2001). "Demonstration of Primary and Secondary Muscle Fiber Architecture of the Bovine Tongue by Diffusion Tensor Magnetic Resonance Imaging." Biophysical Journal **80**(2): 1024-1028.

105. Wedeen, V., T. Reese, et al. (1995). Mapping myocardial architecture with diffusion anisotropy MRI. 3rd Annual Meeting of the ISMRM, Cannes, France.

106. Wedeen, V., T. Reese, et al. (2000). Mapping fiber orientation spectra in cerebral white matter with fourier-transform diffusion MRI. Proceedings of the 8th Annual Meeting of ISMRM, Denver, CO.

107. Wedeen, V. J. (1992). "Magnetic resonance imaging of myocardial kinematics: technique to detect, localize, and quantify the strain rates of the active human myocardium." Magnetic Resonance in Medicine **27**: 52-67.

108. Wein, B., R. Bockler, et al. (1991). "Temporal reconstruction of sonographic imaging of disturbed tongue movements." Dysphagia **6**: 135-139.

109. Wilhelms-Tricarico, R. (1995). "Physiological modeling of speech production: methods for modeling soft tissue articulators." Journal of the Acoustical Society of America **97**(5): 3085-3098.

110. Wu, J., E. Wong, et al. (1993). "In vivo determination of the anisotropic diffusion of water and the T1 and T2 times in the rabbit lens by high-resolution magnetic resonance imaging." Investigative Ophthalmology and Visual Science **34**: 2151-2158.

111. Young, A. A. and L. Axel (1992). "Three-dimensional motion and deformation of the heart wall: estimation and spatial modulation of magnetization - a model-based approach." Radiology **185**: 241-247.

112. Young, A. A., L. Axel, et al. (1993). "Validation of tagging with MR imaging to estimate material deformation." Radiology **188**: 101-108.

113. Zerhouni, E. A., D. M. Parish, et al. (1988). "Human heart: tagging with MR imaging - a method for noninvasive assessment of myocardial motion." Radiology **169**: 59-63.

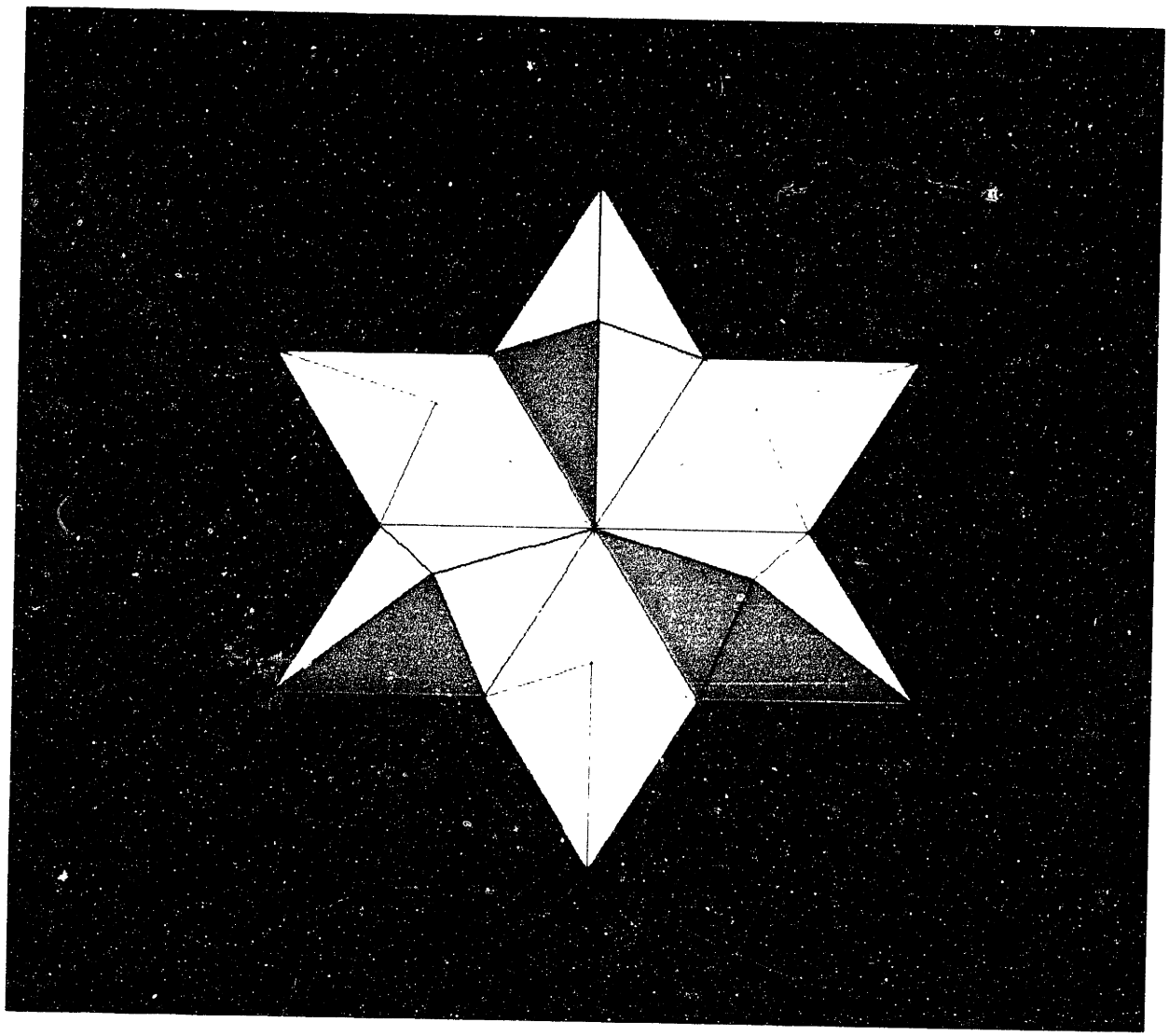

"Star of David"
Six octahedra with eigenvalues $\{0.866, 0.5, 0.5\}$
In memory of my grandfather, David Napadow, who died
on June 29th 2001, the day this thesis was officially signed

THESIS PROCESSING SLIP

FIXED FIELD: ill. _____ name _____

index _____ biblio _____

▶ COPIES: (Archives) Aero Dewey Barker Hum

Lindgren Music Rotch Science Sche-Plough

TITLE VARIES: ▶ ☐ _____

_____

_____

NAME VARIES: ▶ ☐ _____

_____

IMPRINT: (COPYRIGHT) _____

_____

▶ COLLATION: _____

_____

▶ ADD: DEGREE: _____ ▶ DEPT.: _____

▶ ADD: DEGREE: _____ ▶ DEPT.: _____

SUPERVISORS: _____

_____

NOTES:

cat'r: date:

page ▶

▶ DEPT: _____

▶ YEAR: _____ ▶ DEGREE: _____

▶ NAME: _____

_____